ALICE TRD Performance studied with cosmic rays

Martin Freudenberger

Master-Thesis

supervised by

Prof. Dr. Peter Braun-Munzinger

Gesellschaft für Schwerionenforschung

Technische Universität Darmstadt

18.December 2009

ALICE TRD Performance studied with cosmic rays
Das Verhalten des ALICE TRDs untersucht mit kosmischer Strahlung

Master-Thesis by Martin Freudenberger

1.Gutachten: Prof. Dr. Peter Braun-Munzinger
2.Gutachten: Dr. Anton Andronic

Tag der Einreichung: 18. Dezember 2009

Abstract

The performance of the Transition Radiation Detector (TRD) of the ALICE heavy ion experiment at CERN is studied with cosmic radiation. Since cosmic radiation has a large variety in energy and is available in great number, it can be used as a simulation of proton-proton or heavy ion collisions. The detector performance than should be similar to the one expected for collision runs taking into account the differences which originate from the angular distribution of the cosmic radiation when striking the detector volume. For the moment, as the TRD is not completed yet, the performance of the installed supermodules up to the present is investigated. Especially the performance of the single sectors in comparison to the whole TRD and the behavior of the single detectors of each supermodule is studied in this thesis. The results from selected runs taking place in two cosmic run periods during fall 2008 and fall 2009 are presented and finally compared to first results from proton-proton collisions generated in December 2009.

Zusammenfassung

In dieser Arbeit wird das Verhalten des Übergangsstrahlungsdetektors (engl. TRD) des Schwerionen Experiments ALICE, welches derzeit am europäischen Kernforschungslabor CERN und dessen kürzlich in Betrieb genommenen Beschleunigers LHC durchgeführt wird, mit hilfe von kosmischer Strahlung untersucht. Da sich die kosmische Strahlung über einen sehr weiten Energiebereich erstreckt und in großer Anzahl verfügbar ist, kann sie verwendet werden um als Simulation von Proton-Proton oder Schwerionen Kollisionen zu dienen. Das aus der Untersuchung mit kosmischen Strahlen resultierende Verhalten des Detektors sollte ähnlich demjenigen sein, welches für Kollisionen erwartet wird, sofern man den Unterschied beachtet, der durch das Auftreffen der kosmischen Strahlung von außerhalb des Detektors entsteht. Da der TRD noch nicht vollständig ist, wird zunächst das Verhalten der bis zu diesem Zeitpunkt installierten Supermodule erforscht. Von besonderem Interesse ist hierbei das Verhalten der einzelnen beteiligten Abschnitte im Vergleich untereinander und im Zusammenspiel als Ganzes, so wie das Verhalten der einzelnen Detektoren jedes einzelnen Supermoduls. Es werden Resultate ausgewählter Testläufe präsentiert die während zweier Testlauf Phasen im Herbst 2008 und im Herbst 2009 stattfanden. Diese werden schlussendlich mit aktuellen Ergebnissen aus den ersten Proton-Proton Kollisionen vom Dezember 2009 verglichen.

Abstract

Contents

List of Figures

List of Tables

Chapter 1

Introduction

The next step towards a deeper understanding in the field of particle and heavy ion physics, will be taken with the help of the Large Hadron Collider (LHC), which is currently under commissioning at the European Organization for Nuclear Research (CERN) near Geneva. The LHC is a circular particle collider with a circumference of 27 km and lays up to 100 meters underneath the surface crossing the Swiss and French border. The particles injected inside the LHC are either protons, for proton-proton collisions, or lead, for heavy ion collisions. As it is a collider, there are two beams circulating in the ring in opposite directions and collisions take place inside the different experimental setups. Along its way the particle beam passes the following four big experiments in clockwise order:

- ATLAS, located at point 1 at CERN´s main site
- ALICE, located at point 2 near St. Genis-Pouilly
- CMS, located at point 5 near Cessy
- LHCb, located at point 8 near Ferney-Voltaire

In addition there are two smaller experiments LHCf located near ATLAS and TOTEM located at the CMS setup. All experiments are shortly summarized in the following subsections.
In figure 1.1 one can see the placement of the four big experiments and their location as well.

1.1 The LHC

The project planning for the LHC already begun in the mid 1990s, when the LHC project was approved by CERN council in December 1994 [1]. With its help physicists all over the world hope to reveal many secrets in a new territory of particle physics. The energy provided should be able to create particles and states of matter which could answer the most important questions in modern physics. The main focus in the different experiments is set to answer the question of the

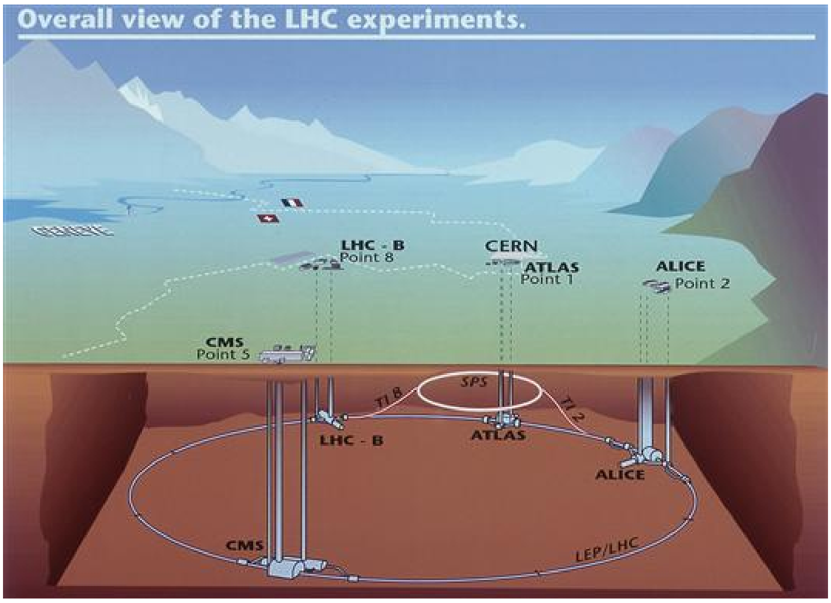

Figure 1.1: The four big LHC experiments and their location can be seen in clockwise order starting at the CERN building in the middle, where ATLAS is located. Next follows ALICE at point 2, CMS at point 5 and finally LHCb at point 8. The transfer insertion lines TI 2 and TI 8, connecting the pre-accelerator SPS to the LHC, can be seen as well. In the background one can see the lake Geneva and the Swiss French border. Picture taken from [2].

origin of mass (ATLAS and CMS), the existence of light super symmetric particles (ATLAS and CMS), the search for dark matter (ATLAS and CMS), the question why matter dominates against antimatter in our universe (LHCb) and the state of matter just after the Big Bang, in which quarks and gluons moved freely in the so called Quark-Gluon-Plasma (ALICE).
To achieve these goals the biggest particle accelerator so far was built as a ring of superconducting magnets with a total length of 26659 meters. Although the LHC is called a circular accelerator it has indeed an octal shape. Therefore it is divided into eight sectors, that were installed separately. One sector is defined as the distance between two injection points, which are numbered from one to eight. At special injection points the experiments are located as can be seen in Figure 1.0.1. Each sectors contains 154 dipole magnets, which are used for bending the beam, so in total there are 1232 dipole magnets used each with a length of 15 meters. For focusing the beam there are in total 392 quadrupole magnets, each 5-7 meters long, along the ring especially at the injection points. It is absolutely necessary that these magnets are in a superconducting state. To achieve this the magnets are cooled down with liquid helium to 1.9 Kelvin, which is colder than the known universe. On the other side the LHC is a very hot place, because the temperature during the collisions is approximately 100000 times the temperature of the interior of the sun. But as the collision energy in the beam pipe is concentrated in protons or lead ions the surrounding material is not effected. Protons that travel

through the LHC are accelerated to 99.99% the speed of light, which means that they circulate the ring with a frequency of 11245 circulations per second.
The LHC uses the older CERN devices as pre-accelerators. The complete accelerator chain is shown in figure 1.2. From a hydrogen source the protons are gained by stripping their electrons. The total amount of hydrogen used is very small in the order of ng. From the source the protons are accelerated in a typical linear accelerator (LINAC 2) and injected in the Proton Synchrotron Booster (PS Booster),which has a circumference of 157 meters. From there the protons are transfered to the PS, which has an circumference of 628 meters and accelerates them up to 25 GeV. The PS is the oldest accelerator at CERN and had its 50th anniversary on November 24th. Particles from the PS can be used for other experiments as well, for example one can use protons to produce proton-antiproton pairs in collisions with fixed targets and store the antiprotons by decelerate them (AD). The next station for the protons on their way to the LHC is the Super Proton Synchrotron (SPS) with a circumference of approximately seven kilometers. Once in the SPS the protons are either transfered to the LHC via transfer tunnels TT 40 or TT 60, each of them 2.5 kilometers long, or used for neutrino production in the CERN Neutrino to Gran Sasso (CNGS) experiment, which sends a beam of muon neutrinos to the Gran Sasso laboratory over a distance of 732 km. After the transfer tunnels TT 40 and TT 60 the protons travel through the transfer insertion (TI) and enter the LHC at insertion point 2 (near the ALICE experiment) via TT 60 and TI 2 or at insertion point 8 (near LHCb) via TT 40 and TI 8.
In case of lead ions instead of protons used for the collisions, the lead ions are gained from a source of vaporised lead and then injected in the LINAC 3. From there they travel to the Low Energy Ion Ring (LEIR) with a circumference of 78 meters and from there to the already mentioned accelerator chain PS, SPS and finally LHC.

1.2 The experiments at the LHC

Along the circular beam line of the LHC, there are four major experiments and two smaller ones. The location of the different experiments can be seen in figure 1.1 together with the layout of the LHC. As the LHC crosses the border between France and Switzerland, three out of four experiments are located on French territory. Only ATLAS the biggest one is hosted at CERN´s main site near the Swiss town of Meyrin, a suburb of Geneva.

1.2.1 ATLAS

The name ATLAS stands for A Torrodial LHC ApparatuS. It is the biggest LHC experiment and is located at Point 1 of the LHC ring. ATLAS is considered as a general purpose experiment, but its main focus is in detecting the Higgs boson as a manifestation of spontaneous symmetry breaking in the electroweak sector of the standard model. Furthermore it should look for extra dimensions and particles belonging to the so called dark matter. Finally the Top Quark is a matter of interest. A general overview can be seen in figure 1.3. ATLAS consists of an

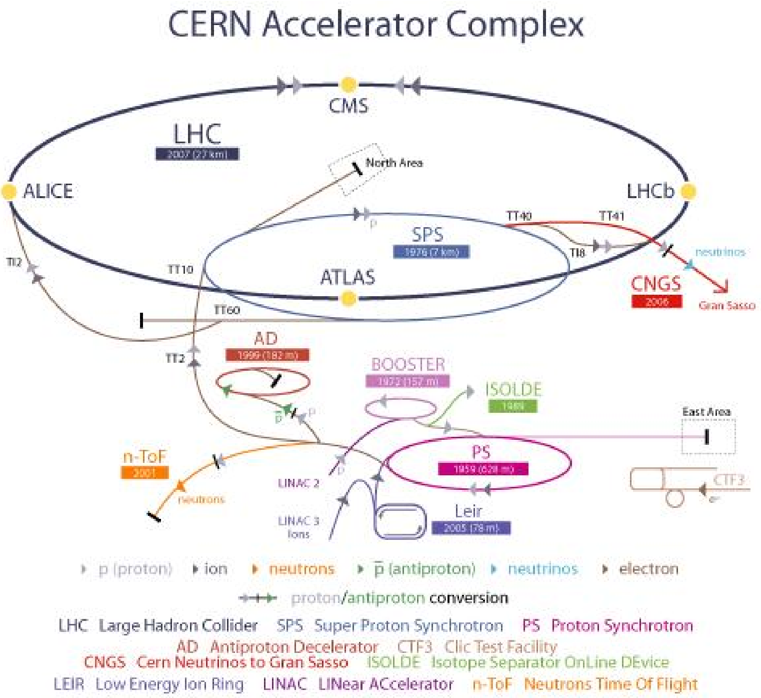

Figure 1.2: In this picture one can see the LHC and its pre-accelerators. The concept is explained in the text. Nucleons travel from their source through PS and SPS and are then inserted in the LHC ring via transfer lines. Picture taken from [3].

inner detector for electron identification, special designed calorimeters and a muon spectrometer [4].

1.2.2 ALICE

The name ALICE means A Large Ion Collision Experiment. The Experiment is located at Point 2 near the French town of St. Genis-Pouilly. As the ALICE Experiment and especially its transition radiation detector (TRD) are a main part of this thesis, both will be looked at in detail in the following chapters. A general overview of ALICE is found in Chapter 2 with a basic discussion of its detectors. The TRD is looked at in Chapter 3.

1.2.3 CMS

CMS is located at point 5 and stands for Compact Muon Solenoid. Like ATLAS CMS´s main focus is on finding the Higgs boson. Other issues CMS wants to study are the search for supersymmetric particles such as squaks and gluinos, the search for new massive vector bosons like $Z^{'}$, detecting extra dimensions beyond the electroweak scale with a possible creation of mini black holes and the investigation

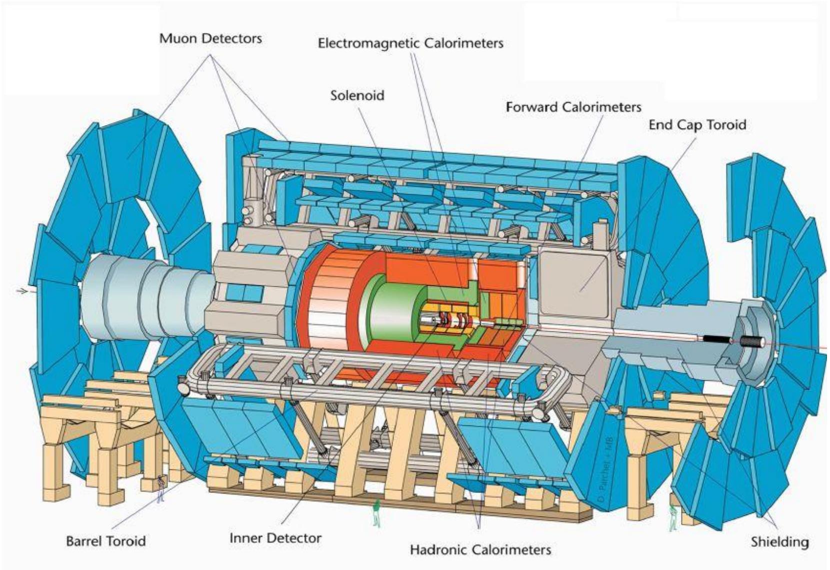

Figure 1.3: Overview of the ATLAS experiment. One can see the single detectors housed in the solenoid magnets. Picture taken from [9]

of heavy-ion collisions with a main focus on jet quenching. Therefore CMS uses electromagnetic and hadron calorimeters and a muon detector similar to ATLAS. The whole detector is housed in a superconducting solenoid magnet [5]. A general overview of CMS is found in figure 1.4.

1.2.4 LHCb

The LHC Beauty Experiment is located at Point 8 in Ferney-Voltaire, France. Its main goal is to investigate the beauty quark and from this derive new knowledge about the abundance of matter and antimatter in the universe. This will be done by studying CP violation through high precision measurements of CP asymmetries and of rare decays in B-meson systems [11] . LHCb is designed as a singlearm spectrometer with a variety of subdetectors which can be seen in the general overview in figure 1.5.

1.2.5 LHCf and TOTEM

The very small LHCf experiment, which is located near the ATLAS experiment at CERN´s main site, is used to detect forward particles created in the LHC collisions. As these forward particles cause cascades of secondary particles like the cascades caused by cosmic rays in collisions in earth´s atmosphere, LHCf is intended to help scientists to interpret and calibrate instruments for large scale cosmic ray experiments [7].
TOTEM is located near the CMS experiment and wants to measure the total cross section with an absolute error of 1 mb, elastic scattering in the largest interval of momentum transfer and the process of diffraction dissociation [8].

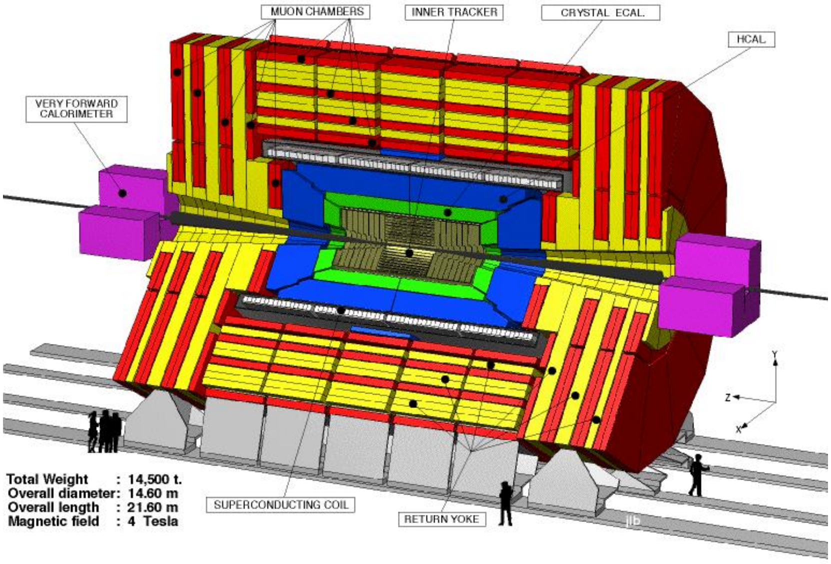

Figure 1.4: The CMS detector. Picture taken from [10].

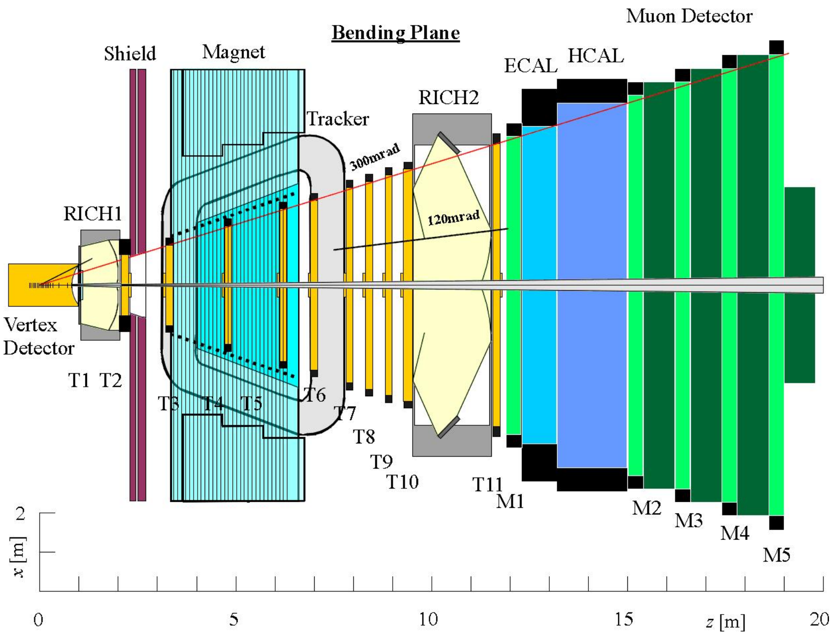

Figure 1.5: The LHCb detector. Picture taken from [11].

Chapter 2

ALICE and the Quark-Gluon-Plasma

2.1 Idea of ALICE

The ALICE experiment is a general-purpose experiment for studying ultra-relativistic heavy-ion collisions at the LHC. ALICE´s main aim is to look for matter at extreme conditions (e.g. extreme energy densities). These conditions are a matter of interest, because similar conditions existed in the very early universe just a few microseconds after the Big Bang and are believed to exist in the core of collapsing neutron stars [12].

2.2 Theoretical background

For understanding the phenomena which occur at very high temperatures or densities in macroscopic objects one has to understand the processes on the microscopic level. There are four fundamental forces in nature which effect ourselves and our surrounding matter. Gravitation and electromagnetism are the most obvious forces on large scales, on the scale of elementary particles one has to take the weak and strong interaction into account but can neglect the gravitational force. As it was shown by Weinberg, Salam and Glashow the weak interaction and electromagnetism are two different occurrences of one unified interaction.

2.2.1 Standard model of particle physics

In the standard model of particle physics the electromagnetic force and the weak interaction are unified to the electroweak interaction. The smallest constituents in this model are quarks and leptons which are divided into three families seen in figure 2.1. The particles responsible for the interaction between these constituents are called force carriers. In case of the electromagnetic interaction the force carrier is the massless photon (γ) and in case of the weak interaction the force carriers are heavy bosons (Z^0, W^+ and W^-). To unify electromagnetism and the weak interaction it was necessary to postulate two neutral vector-bosons (W^0 and B^0),

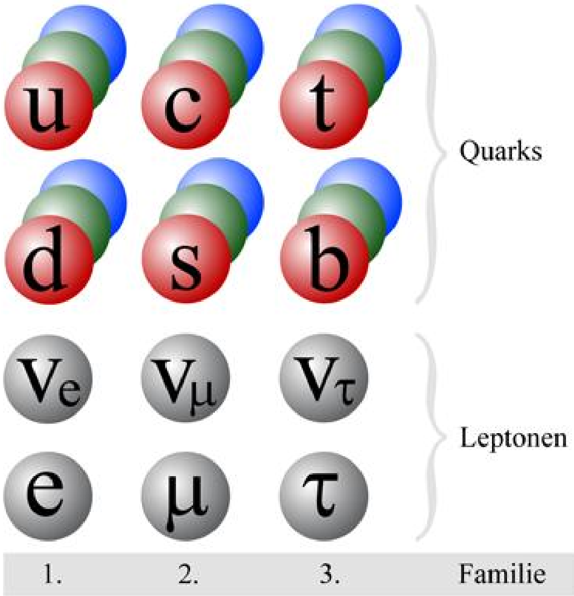

Figure 2.1: The standard model of particle physics. Leptons and quarks can be divided into three families. Picture taken from [16]

which can form two orthogonal linear combinations, the Z^0 boson and the photon. This can be described using the Weinberg angle θ_W and reads:

$$|\gamma\rangle = \cos\theta_W \left|B^0\right\rangle + \sin\theta_W \left|W^0\right\rangle$$

$$\left|Z^0\right\rangle = -\sin\theta_W \left|B^0\right\rangle + \cos\theta_W \left|W^0\right\rangle$$

The above formalism only works if γ and Z^0 have similar masses. Since this is not the case but the masses of W- and Z-boson are rather large ($m_W = (80,41 \pm 0,10)\text{GeV/c}^2$ and $m_Z = (91,187 \pm 0,007)\text{GeV/c}^2$[13]) one has to get rid off the mass of the bosons. This was done in a theoretical model predicted in 1964 independently by Englert and Brout[14] and by Higgs[15]. In this model the bosons are all massless at high energies and interact with the so called Higgs-field as they cool-down and cross the phase boundary. There are four Higgs-bosons (the quantum particles of the Higgs-field) according to each of the vector bosons and by interacting with them the Z^0 and the $W^\pm$ gain their mass. As the photon is a massless particle, it is predicted that there has to be one free Higgs-boson. Detecting this free Higgs-boson was one of the major reasons for building the LHC.

2.2.2 QCD

The theoretical description of the strong interaction is done using the quantum chromodynamics. The new quantum number 'color', which gives the name for the theory, is introduced in this description. Since there are baryons which can contain three quarks of the same flavor[1] and the same spin direction, the color charge, which is defined as an intrinsic feature of the quarks, was predicted to save the Pauli exclusion principle in these baryons. There are three colors known today (red, green and blue) which can occur in eight different combinations. This is a consequence of the mathematical description using a SU(3) symmetry group. Thereby the hadron´s wave function gains a color dependent term which is described by

$$|\Psi_{color}\rangle = \frac{1}{\sqrt{3}}\left(|r\bar{r}\rangle + \left|(b\bar{b})\right\rangle + |(g\bar{g})\rangle\right) \tag{2.1}$$

for mesons and

$$|\Psi_{color}\rangle = \frac{1}{\sqrt{6}}\left(|rgb\rangle + |gbr\rangle + |brg\rangle - |bgr\rangle - |rbg\rangle - |grb\rangle\right) \tag{2.2}$$

for baryons. As SU(3) denotes to the group of unitary matrices of order 3 with determinant det = +1, every 3×3 matrix of the group can be represented through generators λ_a (a = 1, ... , 8) [17]. These generators are reflected by the eight terms in the baryon color wave function and can be described by hermitian and traceless matrices, so called Gell-Mann matrices.

The quark-antiquark potential is qualitatively described by a linear combination of two interaction terms. The first term is a coulomb-like potential for small relative distances and reads:

$$V(r) = -\frac{4}{3}\frac{\alpha_S(Q)}{r} \tag{2.3}$$

Here $\alpha_S(Q)$ is the coupling constant of the strong interaction and r the relative distance between the quarks. In addition, since free single quarks have never been detected, the term for large relative distances grows linear with the distance r analog to the linear function of the spring tension. The combined expression for the quark-antiquark potential then reads:

$$V_{q\bar{q}}(r) = -\frac{4}{3}\frac{\alpha_S(Q)}{r} + k\cdot r \tag{2.4}$$

The interaction is of infinite range since the force carriers, the gluons, are massless spin-1 bosons. But since hadrons are composed objects which are colorless, the resulting force between hadrons is only a residuum of their quark components and therefore cancels when the distance between the hadrons gets larger. Because of the SU(3) symmetry gluons can exist in eight different color states so that each gluon carries a color charge and as a consequence gluons can interact with other gluons. The crucial difference between QCD and QED, where the exchange particles are the photons which are massless spin-1 bosons as well, is the fact that

[1] Flavor is the character of quarks. There are six known flavors: up (u), down (d), strange (s), charm (c), bottom (b) and top (t), which can be distinguished by their mass and charge.

photons are neutral and do not couple themselves to the electric charge and do not interact with each other. The gluon self-coupling leads to interesting consequence, color confinement and asymptotic freedom. As all observed particles have zero color charge, objects like gluons and quarks can not exist as single free particles. Asymptotic freedom occurs when the interaction distance is very small. Then the interaction can be described by one gluon exchange as a process of first order but with a contribution from the self-interacting gluon what leads to the effect that the interaction gets weaker at small distances. On the contrary at larger distances processes of higher order contribute what makes precise theoretical predictions of QDC very complicated. The strength of the coupling constant $\alpha_S(Q)$ can either be described using the distance between the particles or by the momentum transfer Q and is often called running coupling constant that can be derived using

$$\alpha_S(Q) = \frac{12\pi}{(33 - 2N_f)\ln(\frac{Q^2}{\Lambda_{QCD}})} \tag{2.5}$$

where N_f is the number of quark flavors and $\Lambda_{QCD} \approx 200$ MeV[19] is a scale parameter which one has to determine experimentally.

2.2.3 Quark-Gluon-Plasma

From mentioned reasons theoretical forecasts in QCD have to be done using simulations. Most popular and must successful simulations are so called lattice calculations on which space and time are handled as discrete points on a finite lattice. One of the predictions of lattice calculations is a thermodynamical phase transition at a critical temperature of approximately 170 MeV. Above this critical temperature a state called quark-gluon-plasma should be formed, in which quarks and gluons are de-confined and act as quasi-free particles. This state can be reached on two ways. The first possibility is to increase the temperature at zero baryo-chemical potential μ_B. This would follow the inverse way of the early universe, which cooled down at vanishing μ_B crossing the phase border between the QGP and hadronic matter. Thereby a chemical freeze out occurred which ceased the inelastic collisions between particles. The second possibility of creating a QGP is to condense nuclear matter such that the overlap of the hadronic particles leads to a state of quasi free quarks and gluons, the QGP. The latter process is believed to be executed in the interior of neutron stars forming a cold, but very dense QGP there. The phase diagram of nuclear matter can be seen in figure 2.2 where the temperature is plotted versus the baryo-chemical potential. One can see the hadronic phase and the phase of the QGP separated by the phase boundary at approximately 175 MeV at zero baryo-chemical potential. Results from lattice QCD predicting a phase transition of first order (solid line) or a crossover (dashed line) are included as well as the critical point (triangle).
A good phenomenological description is made using the MIT Bag model [19]. In this model hadrons are formed as spherical cavities (the bag) with radius $R \propto \Lambda_{QCD}^{-1}$. Inside the bag the interaction of the quarks and gluons is weak

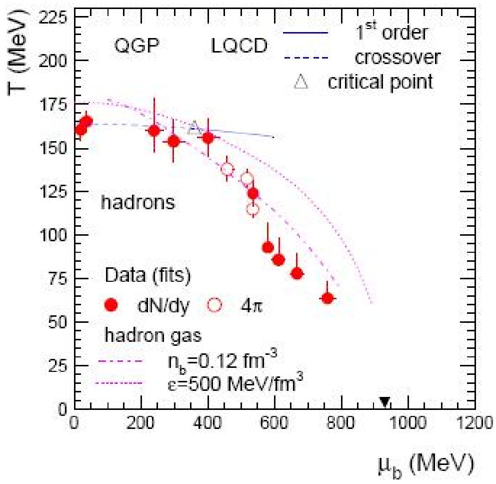

Figure 2.2: Phase diagram of nuclear matter. The temperature is plotted versus the baryo-chemical potential. The data are from a chemical freeze-out analysis in nucleus-nucleus collisions at various beam energies. Picture taken from [18]

according to asymptotic freedom and the boundary of the bag (confinement) prevents quarks and gluons from existing outside the bag. The idealized picture describes a cavity (the hadron) surrounded by QCD vacuum, which is a perfect paramagnetic medium with respect to the color charge. This is an analogous situation to an electric field confined in a cavity in a conductor. The confined field here is the colorfield. A parameter called bag constant B is introduced taking into account the energy density necessary for building the bag. A simple interpretation of the bag constant is to identify it with the pressure on the surface of the bag caused by the vacuum. In the most general case the total energy depending on the bag sphere radius can be written as

$$E(R) = \frac{2.04N}{R} + B\frac{4\pi R^3}{3} \tag{2.6}$$

where N is the number of quarks. By minimizing the energy one can obtain the hadron radius R to

$$R = \sqrt[4]{\frac{2.04N}{4\pi B}} \tag{2.7}$$

and by insertion the hadron mass M becomes:

$$M = \frac{4}{3}\,(2.04N)^{3/4}\,(4\pi B)^{1/4} \tag{2.8}$$

The parameter B can be fitted using experimentally determined hadron masses [20].

2.2.4 Hints for QGP

To confirm the existence of a QGP created in a heavy ion collisions, unambiguous hints for a QGP are needed. There are some specific probes which can be studied within the ALICE experiment [21]. The detection of direct photons is an important tool to diagnose the temperature and initial hard processes in the QGP environment. Direct photons are in contrast to decay photons originating from the initial collision and can be divided into thermal photons, which carry information about the temperature and prompt photons which contain information about the hard processes.

The production of low mass lepton pairs from the decay of open charm and open beauty can be used to gain information about the mechanism of hadron production and propagation in the hot and dense medium. The cross sections of these mesons are needed as reference to the effect of traveling through a de-confined region. Lighter vector mesons ($\rho\omega\phi$) are expected to change their properties in dense matter. Their leptonic decay products are therefore of special interest as well.

An enhancement of strange particle production is expected to take place in a QGP since the process of gluon fusion to strange quarks is favored. Especially the ϕ meson and its decay channel to strange mesons (K^+ and K^-) is of special interest. The ratios between mesons with strange quark content to mesons without strange quark content for pp- and heavy ion collision can be used as experimental tools, e.g. the ratio of K/Π [22].

Another prominent hint for a QGP is the so called jet-quenching. Partons with a high transverse momentum undergo multiple interactions in the medium before the production of jets. Through the energy loss caused by theses interactions the jets are quenched. Therefore the fraction of partons with high transverse momentum is lower in heavy ion collisions compared to pp-collisions.

A quantity for the centrality of the collision is the collective flow of the particles. The collective flow can either be an isotropic distribution, so called radial flow, when the initial collision is a central collision. On the other side when the initial collision is very peripheral then the flow is of an anisotropic form called anisotropic flow. These collective phenomenon can be described using pressure gradients analogous to hydrodynamics. For the anisotropic flow at low energies the particles are produced in the reaction plane and are referred to as directed flow. In contrary for ultra-relativistic energies the momentum can be visualized as an ellipse in the transverse plane and is called elliptic flow.

Finally the suppression or enhancement of charmonia is a signal for a QGP. The suppression of mesons consisting of charm-anticharm quarks especially the ground state J/Ψ in hot dense matter due to Debye screening was introduced by Matsui and Satz in 1986 [23]. Because of recent lattice QCD results, the 'screening' temperature T_D is significantly larger than the critical temperature T_C and exceeds it by a factor of 2 for the J/Ψ [24]. Another approach using the statistical hadronization model [25] predicts an enhancement of J/Ψ production compared to pp collisions due to hadronization of uncorrelated charm quarks at chemical freeze-out.

2.3 ALICE's Detectors

ALICE consists of several detectors which are sensitive on different topics. Only the interaction of all detectors in the experiment will provide reliable results for particle tracking and particle identification as well as momentum measurement. ALICE is housed in a big magnet, that was formerly used in the L3 experiment at the predecessor of the LHC, the LEP. This magnet is called L3 magnet and will be operated at a nominal field strength of +0,2 T. With the help of the magnetic field charged particles will be forced on curved tracks which will help to calculate the particle's mass. In the interior of the magnet the central detectors of ALICE are installed. To hold them in place there is a frame, called main frame. The central detectors are installed around the main frame which has a cylindrical shape to cover the whole azimuth related to the beam axis. Additionally outside the L3 magnet there is a forward detector installed called the myon arm. A scheme of ALICE can be seen in figure 2.3, where the main detectors are labeled.

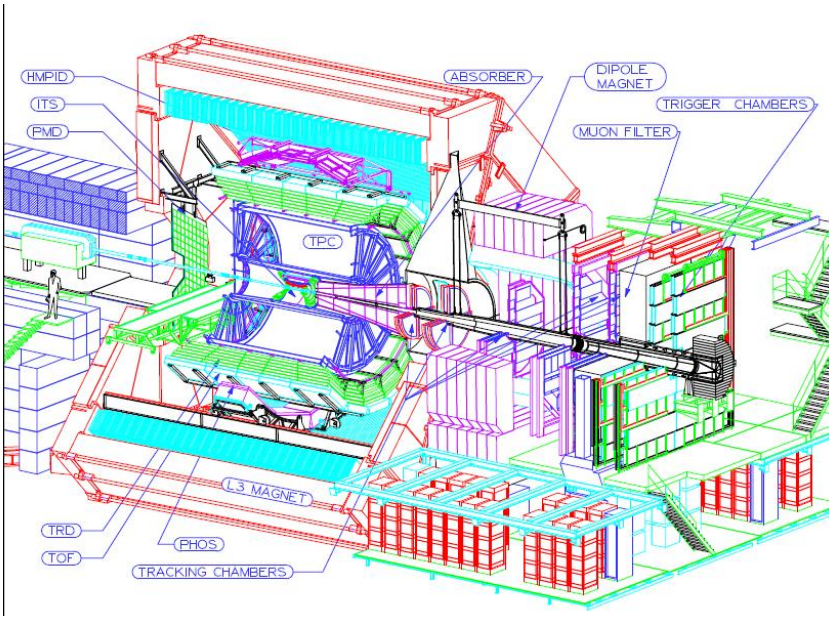

Figure 2.3: Overview of the ALICE Experiment and its Subdetectors. From the beam axis in the middle the detectors covering the full azimuth are ITS, TPC, TRD and TOF. The small detectors FMD, T0 and V0 are located next to ITS. HMPID, PMD and PHOS special positions explained in the text. Next to the central barrel one can see the myon arm. Not visible in the picture are EMCAL and ZDC. Picture taken from the TRD website at GSI[26].

2.3.1 Inner Tracking System (ITS)

The ITS is the innermost detector of ALICE´s central part. It consists of six layers of silicon detectors, that are arranged cylindrically. As the ITS is located next to the beam pipe at a radius of three centimeter, it has to fulfill several tasks. At very small distances the the track density, caused by the primary-vertex particles, is very high. In this region the ITS is responsible for finding tracks and identify particles especially particles with low momenta. It is also responsible for the determination of the primary vertex and of secondary vertices for the reconstruction of charm and hyperon decays. The six ITS layers are divided in three types of silicon detectors each covering two layers. These are the Silicon Pixel Detector (SPD) at radii four and seven centimeters, the Silicon Drift Detector (SDD) at 14,9 cm and 23,8 cm and the Silicon Strip Detector (SSD) at 39,1 cm and 43,6 cm. Further information about the ITS can be found in the ITS Technical Design Report[27].

2.3.2 Time Projection Chamber (TPC)

The main detector of the central barrel is the Time Projection Chamber. It has an inner radius of 80 cm and an outer radius of approximately 250 cm. The TPC is a single barrel filled with a composition of Ar, $C0_2$ and N_2. As it is the main tracking detector for the whole experiment the TPC has to fulfill several tasks. First of all it has to be sure, that the TPC is able to distinguish between different particle tracks, so the two-track resolution has to be optimized. Secondly it is necessary to know the differential energy loss (dE/dx) very precisely two identify particles crossing the TPC. And finally the TPC has to perform an efficient tracking capability to match with tracks seen in ITS and TOF. All these requirements are crucial when dealing with hadronic observables or observables coming from hadronic decays. For the leptonic observables which are detected together with ITS and TRD the TPC has to provide a very good tracking efficiency, good momentum resolution and a good dE/dx resolution for electrons.

2.3.3 Transition Radiation Detector (TRD)

For distinguishing between electrons and charged pions with high momenta, produced in decays of heavy hadrons, one needs a special trick. As the energy loss of electrons and charged pions in this momentum region has the same shape one has to add an additional energy loss for electrons. This energy loss arises when electrons cross the border between two different dielectrica. Then so called transition radiation is produced which can be detected in the TRD. The ALICE TRD is not only able to distinguish electrons and charged pions but is also used as a very fast trigger for the whole experiment. The QGP hints which will be studied with the TRD are mainly the di-electron decay channel of the J/Ψ to investigate its enhancement, the single-electron channel of the semi-leptonic decays of open charm and open beauty and the trigger capability of the TRD for studying jets with high transverse momenta. As the TRD is the main subject of this thesis it will be explained in more details in the following chapter.

2.3.4 Time-Of-Flight detector (TOF)

TOF is the fourth detector of ALICE covering the whole azimuth at a radius of about 3,5 meters. Its main purpose is to separate pions, kaons and protons in the intermediate momentum range (0,2 GeV/c - 2,5 GeV/c)[29]. To meet this condition TOF needs a very good intrinsic time resolution. As the TRD the TOF detector is built of 18 supermodules each consisting of 5 modules. There are three different type of modules which differ in length but all modules are built as multi gap resistive plate chambers with front-end electronics.

2.3.5 HMPID

At momenta above 1 GeV/c the expected yield for most particles is very small. To gain information about particle production via hard processes in this momentum range the High Momentum Particle Identification detector (HMPID) is used. To get data representing these hard processes is of special interest because the initial hard processes can be calculated using perturbative QCD calculations and therefore can verify them[30]. The technique used in this detector is particle identification via Cherenkov radiation, which is produced when a charged particle crosses a di-electric medium and its velocity exceeds the phase velocity of light in this medium. Cherenkov radiation is then emitted under an angle θ relative to the initial track of the particle depending on the refractive index of the medium. Only liquids fulfill the requirements for an adequate refractive index, so the solution for HMPID is to use C_6F_{14}. The produced Cherenkov photons are in the ultra violet range and are finally detected using a multiwire proportional chamber.

2.3.6 PHOS

The PHOton Spectrometer (PHOS) is an electromagnetic calorimeter and is used to measure uncharged particles, especially direct photons from the initial collision or photons from hadronic decays. Direct photons from the initial collision carry information about thermal and dynamical parameters in the initial collision zone. Another issue is the measurement of neutral pion transverse momentum (p_t) spectra to gain information about jet quenching. In the high momentum range the resolution of PHOS is superior to the momentum resolution of the tracking detectors. PHOS consists of 17280 channels of lead-tungstate crystals, $PbWO_4$ (PWO), coupled to PIN-diodes with low noise preamplifiers[31].

2.3.7 MYON Spectrometer

The most prominent signal for a QGP is the suppression of heavy quarkonia resonances (J/Ψ, Ψ', Υ, Υ', Υ''), which can be detected by looking at their leptonic decay mode into dimuons. As muon identification in the LHC environment is only feasible for muon momenta above 4 GeV, a muon spectrometer in forward direction is used[32]. To avoid measuring charged hadrons an absorber is placed between the central part of ALICE and the muon arm. Behind the absorber plate there is a low angle absorber for absorbing charged particles originating from the beam pipe.
There are several tracking chambers behind the low angle absorber to identify the tracks of the muons crossing the detector and a dipole magnet to separate positive and negative muons. In order not to detect low p_t muons or muons from the background a muon filter is used. Finally there is another tracking chamber at the outermost position, which acts as a fast trigger for high energy muons.

2.3.8 Photon Multiplicity Detector (PMD)

The Photon Multiplicity Detector (PMD) is a pre-shower detector that measures the multiplicity and spatial distribution of photons on an event-by-event basis in the forward region of ALICE[33]. The used design is a gaseous proportional counter with a honeycomb structure. This leads to an almost perfect circular equipotential within the cells. To avoid δ-rays in the PMD the honeycomb walls are thin metallic plates. Another crucial design consideration is to prevent interaction of neutrons with the detector gas. So the choice is a mixture of Ar and CO_2. The location of PMD is on the opposite side of the myon arm approximately 360 cm away from the interaction point.

2.3.9 ZDC

To gain information about the centrality of the initial collision one can use a simple relationship between the participating nucleons and the non-interacting, so called 'spectator' nucleons. It is obvious that the number of participating nucleons N_P can be derived when the number of spectators N_S and the nucleon number A of the colliding nuclei is known. The quantity used to determine N_P is the energy E_S carried away by the spectators. The simple expression then says $N_P = A - E_S/E_A$ where E_A is the beam energy per nucleon[34]. To measure E_S one uses calorimeters which are located in the beam pipe approximately 115 meters away from the collision point. The ALICE ZDC has to be very resistant against radiation, therefore a device made out of quartz fibres is used, as they provide very good radiation shielding.

2.3.10 EMCal

As the EMCal is still in a developing mode it is not installed in the ALICE barrel so far. Its final location will be inside the magnet 110 cm deep in the radial direction sandwiched between the space-frame and the magnet coils[35]. When EMCal is integrated its main task will be to provide a fast trigger on high energy jets and enhance ALICE´s capability for jet quenching measurements. The jet energy resolution will be improved with EMCal as well. The used technology is a layered Pb-scintillator sampling calorimeter.

2.3.11 FMD, T0, V0

The three detectors FMD, T0 and V0 form the Forward Detector system (FWD) which acts as the initial trigger for the other ALICE detectors. The FWD is installed at small radial distances from the beam pipe at both sides of the interaction point. Because of limited space in the vicinity of the interaction point and because of high costs the FWD acts as a compromise instead of one single detector.
The T0 detector is split into two arms on both sides of the interaction point. It consists of two arrays of Photo Multiplier Tubes (PMT) equipped with Cherenkov radiators. The main task of T0 is to provide fast timing signals used for the L0 trigger-chain, to produce a wake-up call for the TRD and to deliver a collision time reference for TOF as well[36]. With the main trigger signal the location of the interaction point can be confirmed up to an accuracy of 1,5 cm. Therefore a very good time resolution in the order of 50 ps and a dead time smaller than the bunch crossing time (25 ns) are the main requirements.
The V0 detector is located on both sides of the interaction point approximately 340 cm (A-side) or 90 cm (C-side) away from the interaction point. V0 is designed as cylindrical disks housed in a box surrounding the beam pipe. The used technique is to produce scintillation light which is converted by wavelength shifting fibres and then read out via photomultipliers. Its main task is to provide the on-line L0 centrality trigger for the central detectors of ALICE and in addition to provide a background rejection for the muon arm detector[37].
Providing information about the charged particle multiplicity is the main task of the Forward Multiplicity Detector (FMD). Because of its relatively slow read out time of approximately 13 μs, FMD is only used in the L2 trigger chain or higher. Together with ITS the charged multiplicity distributions for all beam types can be derived. The FMD´s layout is a silicon strip detector with 51200 channels distributed over five ring counters[38].

Chapter 3

The TRD Design

3.1 Transition Radiation

The TRD is based on the physical phenomena of transition radiation (TR), which is emitted as electromagnetic radiation when a relativistic charged particle crosses the border of two different dielectrica. The charged particle in the first medium and its image charge, which is built up in the second medium, form a time variable dipole, which then emits the TR [39]. The intensity of the photons which are created by a particle of charge ze can then be described using the following formula:

$$I = \alpha z^2 \gamma \hbar \omega_P / 3 \tag{3.1}$$

In this formula α is the coupling constant of the electromagnetic interaction ($\alpha = 1/137$), γ is the relativistic Lorentz coefficient ($\gamma = \frac{1}{\sqrt{1-(\frac{v}{c})^2}}$) and ω_P is a material property, the so called plasma frequency:

$$\omega_P = \sqrt{\frac{4\pi\alpha n_e}{m_e}} = 28.8\sqrt{\rho\frac{Z}{A}} \text{ eV} \tag{3.2}$$

In the first equation n_e is the electron density of the material and m_e the electron mass ($m_e = 511$ keV). The values in the second equation are the material density ρ, the atomic number Z and the number of nucleons A.
The energy density spectrum radiated at polar angle Θ by a charged particle with Lorentz factor γ has the following expression [40]:

$$\frac{d^2W}{d\omega d\Omega} = \frac{\alpha}{\pi^2}\left(\frac{\Theta}{\gamma^{-2}+\Theta^2+\xi_1^2} - \frac{\Theta}{\gamma^{-2}+\Theta^2+\xi_2^2}\right)^2 \tag{3.3}$$

The abbreviation $\xi_i^2 = \frac{\omega_{P,i}^2}{\omega^2} = 1 - \varepsilon_i(\omega)$ is used here, where $\varepsilon(\omega)$ is the dielectric constant.

As the emission angle Θ is small, it can be written in a first approximation as $\Theta \approx \frac{1}{\gamma}$. The energy density spectrum is then integrated over the full solid angle and one gets the differential energy spectrum:

$$\left(\frac{dW}{d\omega}\right) = \frac{\alpha}{\pi}\left[\frac{\xi_1^2 + \xi_2^2 + 2\gamma^{-2}}{\xi_1^2 - \xi_2^2}\ln\left(\frac{\gamma^{-2} + \xi_1^2}{\gamma^{-2} + \xi_2^2}\right) - 2\right] \tag{3.4}$$

Because of the linearity of the Lorentz factor ($\gamma = \frac{E}{mc^2}$) it is obvious that lighter particles can reach great values for γ much easier than heavy particles. For example to reach a γ value of 1000 for electrons one only needs about 1000 times the mass of an electron (511 keV $\cdot$ 1000 $=$ 0,511 GeV) as initial momentum. Therefore a distinction between the additional radiation coming from electrons and charged pions ($m_{pion} = (139,5702 \pm 0,0004)$ MeV[43]) can be made easily and one can expect an additional signal for electrons when looking at the energy loss of charged particles at momenta about 1 GeV/c. For getting a good yield for the produced X-rays due to TR it is necessary to have stacks instead of one single foil, as the yield scales with α. The stack method is implemented in the ALICE TRD.

3.2 TRD Layout

The ALICE TRD is a combination of single TRDs put together in so called supermodules. One supermodule consists of six detector layers and five detector stacks giving a total of 30 single detectors, so called readout chambers (ROC), in one supermodule. Each supermodule covers an angle of 20°, that gives 18 supermodules in total. The single sectors in the ALICE spaceframe and the installed supermodules can be seen in figure 3.1. The ROCs are in principle gaseous proportional counters with a radiator part for producing the TR photons and a front-end electronic part for the data readout of the chambers. Like other proportional counters the ROC have a drift region and an amplification region near the anode wire plane. Both regions are separated by the cathode wire plane, which is more than 99 % transparent for electrons but at the same time prevents 72 % of the produced positive ions to drift back into the drift ragion. A charged particle crossing a TRD chamber loses parts of its energy via ionization with the fill gas in the drift region. The primary produced electrons then drift towards the amplification region with a drift velocity of 1,5 μs/cm, which leads to a total drift time of 2 μs in the 3 cm long drift region. The drift region is split into 30 timebins each 66 ns long. If the charged particle is an electron it is able to produce TR photons in the radiator part of the readout chamber. These photons reach the gas volume as well with energies in the order of typically 10 keV. A high photo absorption probability is provided by high mass noble gases such as Ar and Xe. A gas mixture of Xe and CO_2 as quench gas is the best choice for the ALICE TRD. The principle movement of charged particles (electrons and pions in this case) can be seen in figure 3.2.

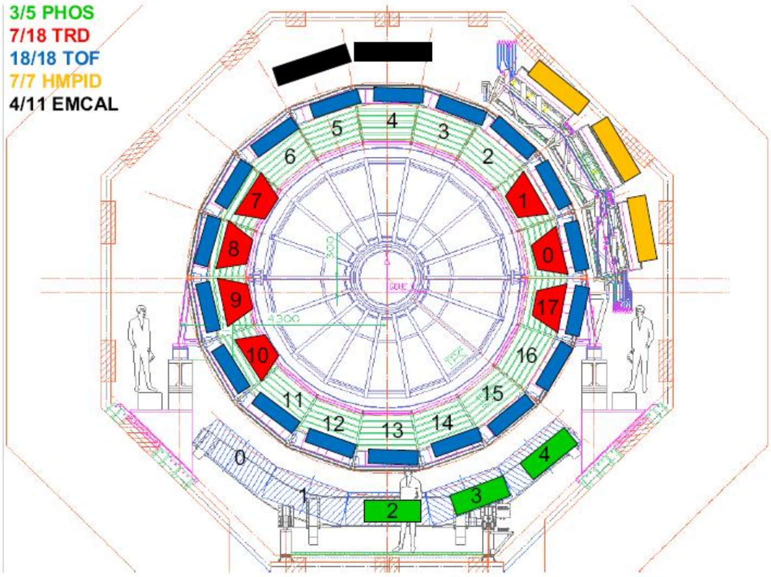

Figure 3.1: In this picture one can see the TRD Supermodules, which are installed at the moment. All seven sectors contributed to the cosmic run period LHC09c and will now take data during the first proton-proton collisions in ALICE. For the cosmic run period LHC08d only sectors 0, 8, 9 and 17 were installed. Picture taken from ?

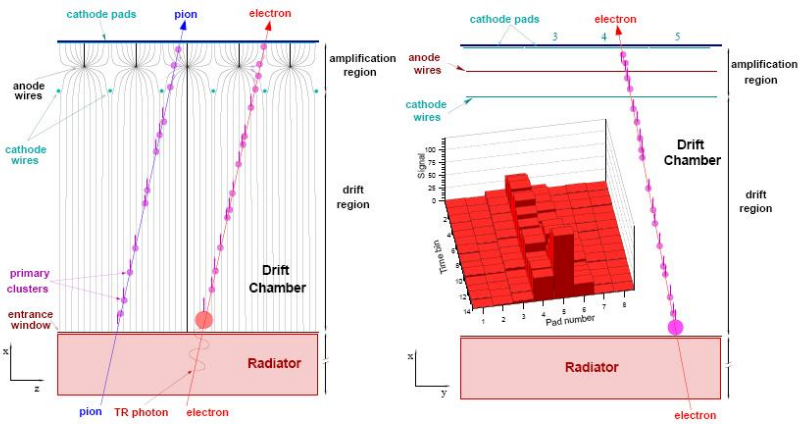

Figure 3.2: In the left panel the plane perpendicular to the wire plane is shown. The anode wires as well as the cathode wires are in the azimuthal direction. One can see the electric field lines starting at the anodes. A charged particle can drift on these lines towards the amplification region, which lies between the cathode wires and the cathode pads. For primary electron clusters TR photons causes additional electrons in the drift region. In the right panel a plane parallel to the wire planes is shown. The lego plot shows a typical track depending on the timebin and the pad number. Picture taken from [44].

Once in the amplification region, which has a total length of 0,7 cm, the electrons are multiplied by avalanche formation[1]. The positive charged Xe ions then drift towards the cathode pads and induce an electric signal there. This signal is then further processed in the data readout chain.

3.3 Data processing

A signal which is detected in the pad plane is shipped to the front-end electronic of every chamber. The signals have to be shaped and digitized before they are read out. This is done in a special designed chip doing the signal pre-amplification and shaping (PASA) and the digitization (ADC). The digitized signals are then analyzed by the tracklet processor (TRAP), which has the main task to look for tracklets of the charged particle track. The different analog and digital parts are grouped together for eighteen channels on one, so called, multi chip module (MCM). There are seventeen or eighteen MCMs forming a read-out board (ROB) and six to eight ROBs are installed on every chamber. Further details on the functionality of the electronics and the readout of the data tree can be found in the technical design report[40].

3.4 Computing

The general computing model for ALICE is described in the computing technical design report [41]. Referring to this report the front-end electronics send their data, which are event fragments via the ALICE Detector Data Links (DDL) to the Data Acquisition Readout Receiver Cards (D-RORCs).The fragments are merged to sub-events in the Local Data Concentrators (LDCs). From there the sub-events, which belong to the same physical interaction, are shipped to the Global Data Concentrator (GDC) where the whole event is built.

3.4.1 The AliRoot framework

The ALICE computing framework is based on the existing ROOT framework [42], which is nowadays the standard investigation tool for high energy physics. AliRoot can provide simulations as well as data analysis. In the simulation part data are generated via a Monte Carlo event generator and are then transported through the detector using detector simulation packages. A detailed energy deposition in a detector, called a hit, is created and transformed to a detector response and finally transformed into raw data format. For the data analysis the raw data of

[1]When the electrons drift towards the anode they gain kinetic energy through acceleration in the electric field caused by the anode and cathode wires. In the vicinity of the anode the electrons are then able to ionize the fill gas as well. This process can take place several times depending on the fraction of kinetic energy of the drifting electrons and the binding energy of the atomic electrons. Usually a multiplication factor of 10^4 is reached with avalanche formation.

real events are processed and reconstructed. Reconstruction is done using the space points generated by a charged particle crossing the detector volume. The cluster finding method to reconstruct the space points in the TRD is described in the technical design report [40]. The output of a reconstruction pass is stored as Event Summary Data (ESD) file. The ESDs contain all necessary information about the particle tracks, particle identification and decay channels. A high statistic run contains around 400 ESD files which then have to be analyzed using again AliRoot. The result is a Root tree file containing several histograms with information about the cluster, the tracklets, the tracks and the charge distribution. Depending on the used AliRoot version some details in the assembly of the histograms alter. For the cosmic run period LHC08d AliRoot version 4-16-Rev-01 was used. Whereas for the run period LHC09c version v4-17-Rev-05 was used for the runs 81043 to 89097 and v4-17-Rev-16 was used for the runs 95741 to 99031.

Chapter 4

Cosmic data taking with the TRD

4.1 Cosmic Radiation

Cosmic Radiation is the summary of extraterrestrial particles coming from the Sun, the Milky Way or even from other galaxies. It consists mainly of positive charged particles (protons, α-particles or heavy ions) in a big variety of energy. Particles from the Sun originate from flares with energies of some GeV and can be accelerated up to 10^{10} eV in the plasma of the Sun´s corona [45]. Non-solar particles occur with energies reaching from 10^{8} eV up to the enormous energy of 10^{20} eV (approximately 10^{7} times the LHC endpoint energy for protons). The energy spectrum can be seen in figure 4.1. Because Earth´s magnetic field has no influence on high energetic particles (E > 10^{10} eV) only energies above 10^{11} eV are shown in the figure. In this region the integrated energy spectrum scales with a power law function:

$$J(> E) = J_0 \cdot \left(\frac{E}{E_0}\right)^{-\gamma} \tag{4.1}$$

The exponent in the power law equals 1.7 up to an energy of 10^{15} eV and gets 2.1 for higher energies forming the so called knee in the energy spectrum. For energies around 10^{20} eV the particle flux becomes very low and only about one nucleon per square kilometer per year can be detected on earth. There are as well electrons in the primary cosmic radiation, but their fraction only is about 1 % of the total cosmic radiation.

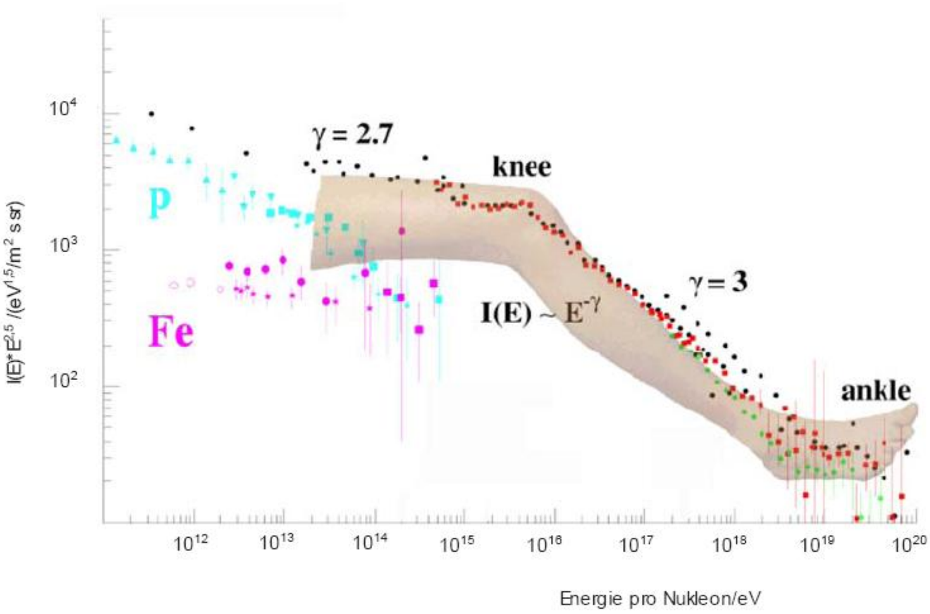

Figure 4.1: Energy spectrum of cosmic radiation in the energy range from 10^{11} eV to 10^{20} eV. On the ordinate the intensity is plotted scaled with a factor of 2,5 to reveal the structure of the curve. Taken from [46]

When colliding with Earth´s atmosphere the high energetic cosmic radiation produces cascades of secondary particles which can decay on their way to the ground as well. In a first step charged and uncharged pions, protons and neutrons are produced. The uncharged pions decay to γ-radiation, the charged pions decay to muons. As the kinetic energy of muons is of relativistic order they can reach the sea level due to time dilatation, although they decay themselves to electrons or positrons. A cosmic shower event therefore has three components, a soft electromagnetic component (γ-rays from π^0 decays), a nucleonic component (protons and neutrons) and a hard mesonic component (decay of muons). Mainly electrons, muons and neutrinos reach the sea level after secondary decay processes, but as neutrinos interact very seldom with surrounding material only electrons and muons can be detected with a good yield. Their contribution to every days radiative exposure at sea level is approximately 0,3 mSv per year, which is roughly 10 % of the natural exposure in Germany. A principle view of a shower event can be seen in figure 4.2.

4.2 TRD and cosmics

As the cosmic radiation consists of high energetic particles, it is a good probe to test the detector performance of the TRD. In principle the cosmic radiation creates an environment similar to a collision in the LHC with lots of secondary charged particles decaying themselves in leptonic components. What ends up in

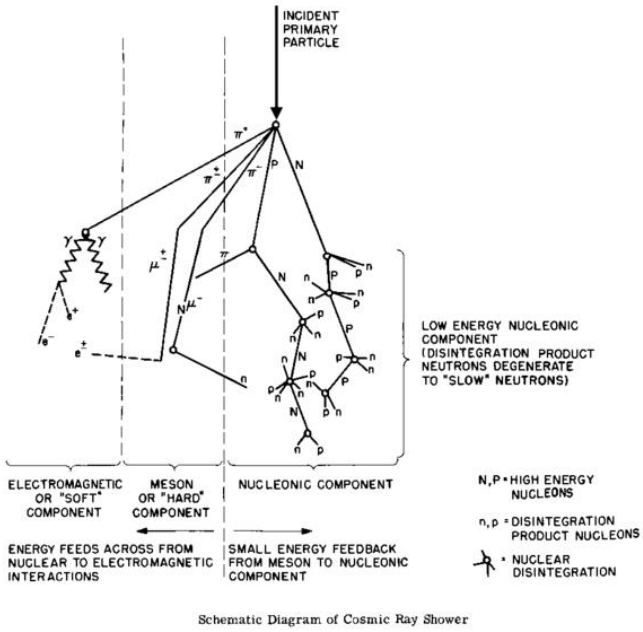

Figure 4.2: A schematic diagram describing a cosmic shower. The primary particle triggers a cascade of secondary particles. The cascade can be classified in different components of particles, mentioned in the text. Picture taken from [47].

the TRD are muons which made their way through the atmosphere and the rock between the surface and the pit where ALICE is located. The yield of TR photons can be estimated taking into account that muons are roughly 200 times heavier than electrons. The basic detector checks which can be applied are the performance of the average pulse height spectrum from the signal depending on the timebins. Another issue which can be studied is the behavior of single detectors in the interaction with the whole system and of course a check of the analysis software tools which are used. Moreover one can expect effects of the geometry of the participating supermodules. As one can see in figure 3.1, the sectors 0, 8, 9 and 17 are located on a position with a zenith angle between $\pm 70°$ and $\pm 90°$ (sectors 0 and 8) and accordingly between $\pm 90°$ and $\pm 110°$ (sectors 9 and 17) relative to the vertical. Therefore it is expected that more cosmics will hit the outermost sectors 1, 7 and 10, which have a zenith angle between $\pm 50°$ and $\pm 70°$ (sectors 1 and 7) and accordingly between 110° and 130° (sector 10). The muons suffer from energy loss of the surface material and only muons exceeding the threshold energy of 15 GeV can be detected. This is only true for muons entering directly vertical into the detector. For increasing zenith angles relative to the vertical the threshold energy rises due to the bigger amount of geological material which has to be passed by the muons. There is a significant drop in the threshold energy down to only about 5 GeV at zenith angles of $\pm 20°$ to $\pm 40°$ due to the supply shafts PX24 and PM25 crossing the rock.

Because of the very flat above area, the well known rock material with a thickness of 30 meters between the surface and the detector and the very high energy in the collisions, the ALICE experiment is aible to determine the muon absorption with high precission and to study cosmic radiation in a yet undiscovered energy range. With respect to empty bunch crossing times a total of 30 days per year can be used to collect cosmic data. Therefore ALICE could answer questions concerning the unexplored knee of the cosmic radiation energy distribution. Further information about cosmic radiation analysis can be found in the physics performance report [21].

4.2.1 Chambers in use

As mentioned above there are seven sectors installed in the TRD so far. For a detailed look on the single detector behavior it is necessary to know about the specific behavior of these single chambers. To connect the results obtained from detector electronic tests done in Frankfurt and at GSI with the cosmic data, the following tables will give an overview of the location of every single chamber inside the complete TRD. Although the supermodules located in sector 0 and sector 8 were removed for maintance reasons between the run periods LHC08d and LHC09c, they were later re-installed in the same sectors.

Sector 0			Sector 1		
#	Position	Chamber #	#	Position	Chamber #
0	S0L0	L0C1_006	30	S0L0	L0C1_028
1	S0L1	L1C1_014	31	S0L1	L1C1_037
2	S0L2	L2C1_007	32	S0L2	L2C1_035
3	S0L3	L3C1_030	33	S0L3	L3C1_025
4	S0L4	L4C1_005	34	S0L4	L4C1_051
5	S0L5	L5C1_025	35	S0L5	L5C1_022
6	S1L0	L0C1_005	36	S1L0	L0C1_020
7	S1L1	L1C1_003	37	S1L1	L1C1_024
8	S1L2	L2C1_026	38	S1L2	L2C1_032
9	S1L3	L3C1_034	39	S1L3	L3C1_029
10	S1L4	L4C1_012	40	S1L4	L4C1_059
11	S1L5	L5C1_008	41	S1L5	L5C1_069
12	S2L0	L0C0_003	42	S2L0	L0C0_004
13	S2L1	L1C0_006	43	S2L1	L1C0_013
14	S2L2	L2C0_012	44	S2L2	L2C0_014
15	S2L3	L3C0_001	45	S2L3	L3C0_012
16	S2L4	L4C0_015	46	S2L4	L4C0_005
17	S2L5	L5C0_012	47	S2L5	L5C0_009
18	S3L0	L0C1_032	48	S3L0	L0C1_024
19	S3L1	L1C1_018	49	S3L1	L1C1_045
20	S3L2	L2C1_022	50	S3L2	L2C1_024
21	S3L3	L3C1_014	51	S3L3	L3C1_001
22	S3L4	L4C1_023	52	S3L4	L4C1_007
23	S3L5	L5C1_018	53	S3L5	L5C1_045
24	S4L0	L0C1_008	54	S4L0	L0C1_023
25	S4L1	L1C1_029	55	S4L1	L1C1_051
26	S4L2	L2C1_015	56	S4L2	L2C1_029
27	S4L3	L3C1_005	57	S4L3	L3C1_060
28	S4L4	L4C1_018	58	S4L4	L4C1_014
29	S4L5	L5C1_026	59	S4L5	L5C1_044

Table 4.1: Readout Chambers of sector 0 and 1. Supermodule 2 was installed in sector 0 in November 2007 and was removed one year later due to leakage problems and was reinstalled after repair at GSI in April 2009. Supermodule 6 was installed in sector 1 in January 2009. This supermodule contains chambers which were equipped with electronics and tested at GSI in the framework of the proposal to this thesis [48].

Sector 7		
#	Position	Chamber #
210	S0L0	L0C1_022
211	S0L1	L1C1_008
212	S0L2	L2C1_023
213	S0L3	L3C1_012
214	S0L4	L4C1_035
215	S0L5	L5C1_062
216	S1L0	L0C1_021
217	S1L1	L1C1_027
218	S1L2	L2C1_033
219	S1L3	L3C1_020
220	S1L4	L4C1_036
221	S1L5	L5C1_050
222	S2L0	L0C0_001
223	S2L1	L1C0_012
224	S2L2	L2C0_015
225	S2L3	L3C0_014
226	S2L4	L4C0_001
227	S2L5	L5C0_010
228	S3L0	L0C1_029
229	S3L1	L1C1_036
230	S3L2	L2C1_025
231	S3L3	L3C1_036
232	S3L4	L4C1_028
233	S3L5	L5C1_049
234	S4L0	L0C1_030
235	S4L1	L1C1_021
236	S4L2	L2C1_031
237	S4L3	L3C1_028
238	S4L4	L4C1_025
239	S4L5	L5C1_051

Sector 8		
#	Position	Chamber #
240	S0L0	L0C1_004
241	S0L1	L1C1_011
242	S0L2	L2C1_018
243	S0L3	L3C1_031
244	S0L4	L4C1_011
245	S0L5	L5C1_003
246	S1L0	L0C1_002
247	S1L1	L1C1_019
248	S1L2	L2C1_001
249	S1L3	L3C1_044
250	S1L4	L4C1_008
251	S1L5	L5C1_034
252	S2L0	L0C0_015
253	S2L1	L1C0_008
254	S2L2	L2C0_019
255	S2L3	L3C0_008
256	S2L4	L4C0_018
257	S2L5	L5C0_001
258	S3L0	L0C1_001
259	S3L1	L1C1_020
260	S3L2	L2C1_003
261	S3L3	L3C1_076
262	S3L4	L4C1_004
263	S3L5	L5C1_035
264	S4L0	L0C1_003
265	S4L1	L1C1_002
266	S4L2	L2C1_005
267	S4L3	L3C1_038
268	S4L4	L4C1_073
269	S4L5	L5C1_004

Table 4.2: Readout chambers of sector 7 and 8. Supermodule 3 was installed in sector 7 in November 2008 after it was shipped back to Münster due to leakage problems. Supermodule 1 was installed in sector 8 for the first time in January 2007, but was removed in November 2008 due to leakage problems as well and was re-installed in sector 8 in July 2009.

Sector 9		
#	Position	Chamber #
270	S0L0	L0C1_026
271	S0L1	L1C1_035
272	S0L2	L2C1_030
273	S0L3	L3C1_015
274	S0L4	L4C1_010
275	S0L5	L5C1_021
276	S1L0	L0C1_010
277	S1L1	L1C1_004
278	S1L2	L2C1_002
279	S1L3	L3C1_002
280	S1L4	L4C1_024
281	S1L5	L5C1_036
282	S2L0	L0C0_016
283	S2L1	L1C0_014
284	S2L2	L2C0_017
285	S2L3	L3C0_002
286	S2L4	L4C0_009
287	S2L5	L5C0_008
288	S3L0	L0C1_035
289	S3L1	L1C1_006
290	S3L2	L2C1_017
291	S3L3	L3C1_010
292	S3L4	L4C1_015
293	S3L5	L5C1_032
294	S4L0	L0C1_015
295	S4L1	L1C1_028
296	S4L2	L2C1_021
297	S4L3	L3C1_011
298	S4L4	L4C1_013
299	S4L5	L5C1_013

Sector 10		
#	Position	Chamber #
300	S0L0	L0C1_057
301	S0L1	L1C1_039
302	S0L2	L2C1_049
303	S0L3	L3C1_045
304	S0L4	L4C1_017
305	S0L5	L5C1_061
306	S1L0	L0C1_018
307	S1L1	L1C1_042
308	S1L2	L2C1_047
309	S1L3	L3C1_019
310	S1L4	L4C1_029
311	S1L5	L5C1_074
312	S2L0	L0C0_005
313	S2L1	L1C0_021
314	S2L2	L2C0_013
315	S2L3	L3C0_011
316	S2L4	L4C0_010
317	S2L5	L5C0_018
318	S3L0	L0C1_058
319	S3L1	L1C1_033
320	S3L2	L2C1_039
321	S3L3	L3C1_069
322	S3L4	L4C1_047
323	S3L5	L5C1_005
324	S4L0	L0C1_016
325	S4L1	L1C1_040
326	S4L2	L2C1_066
327	S4L3	L3C1_035
328	S4L4	L4C1_053
329	S4L5	L5C1_020

Table 4.3: Readout chambers of sector 9 and 10. Supermodule 4 was installed in sector 9 in May 2008. Supermodule 7 was installed in sector 10 in August 2009. There were no leakage problems with these chambers as they were repaired before their transport to CERN.

Sector 17		
#	Position	Chamber #
510	S0L0	L0C1_007
511	S0L1	L1C1_001
512	S0L2	L2C1_028
513	S0L3	L3C1_009
514	S0L4	L4C1_032
515	S0L5	L5C1_001
516	S1L0	L0C1_014
517	S1L1	L1C1_023
518	S1L2	L2C1_034
519	S1L3	L3C1_008
520	S1L4	L4C1_021
521	S1L5	L5C1_028
522	S2L0	L0C0_010
523	S2L1	L1C0_007
524	S2L2	L2C0_018
525	S2L3	L3C0_016
526	S2L4	L4C0_012
527	S2L5	L5C0_016
528	S3L0	L0C1_025
529	S3L1	L1C1_038
530	S3L2	L2C1_020
531	S3L3	L3C1_032
532	S3L4	L4C1_020
533	S3L5	L5C1_010
534	S4L0	L0C1_012
535	S4L1	L1C1_022
536	S4L2	L2C1_012
537	S4L3	L3C1_018
538	S4L4	L4C1_022
539	S4L5	L5C1_033

Table 4.4: Readout chambers of Sector 17. Supermodule 5 was succesfully installed in sector 17 in May 2008. It was leak-fixed before installation.

4.3 Cosmic runs at the LHC

In this thesis the performance of the TRD during two different cosmic run periods is studied. The first run period (LHC08d) took place from September 2008 until October 2008. The second run period (LHC09c) started in August 2009 and ended just some days before the restart of the LHC in November 2009.

4.3.1 Run period LHC08d

For run period LHC08d only sectors 0, 8, 9 and 17 contributed. Because these sectors have a small angular placement relative to the horizontal plane one can expect a lower rate of recorded events. The mean duration of the runs was 2,4 hours, with one very long run of more then 10 hours and seven runs with a duration of less then 1 hour of which one run has a duration of only 15 s. The magnetic field of the L3 magnet was only applied for runs 62006 and 62029, which took place on October 7th, with a nominal strength of +0,5 T and for the runs 62084 and 62102, which took place on October 8th, with a strength of -0,5 T.

4.3.2 Run period LHC09c

The cosmic run period LHC09c started in August 2009 after the installation of sectors 1, 7 and 10 and the re-installation of sectors 0 and 8, which had to be leak-fixed at GSI. The new installed sectors are placed under an angle of $\pm 40°$ relative to the horizontal plane. Therefore one can expect a larger number of entries in these sectors for cosmic runs. The mean duration of the runs was 2,6 hours, with two runs lasting for more then seven hours and one run with a duration of only three minutes. The magnetic field of the L3 magnet was applied for the runs 95741 to 99031 with a nominal strength of +0,2 T. In these run for the first time Xe was used as fill gas.

Chapter 5

Results from Aliroot analysis

5.1 Analysis plots created with ROOT

The plots which are shown in this chapter were produced using the ROOT version 5-24-00. The root files from the AliRoot analysis contain histograms for the objects of interest. The histograms from run period LHC09c and some of the runs from run period LHC08d (60283, 60419, 60517, 60545 and 60668) are then put together using the macro PlotPHSectors.C based on a C++ code. Only runs which have passed the ALIROOT analysis and contain the debug file are used. The histogram objects which are derived are a main monitor plot for basic detector checks, a single sector overview for the deposited charge per timebin and its profile projection and a detailed single detector overview for the deposited charge per timebin. The bi-dimensional plots are color coded showing the entries in the corresponding bin. The macro can be found in the appendix.

5.1.1 Monitoring plots

The monitoring plots made for every run contain some basic information about the performance of the detector. An example for a very high statistic run (run 96287) can be seen in figure 5.1. In the upper left panel the distribution of tracklets per track is plotted. The mean value for the number of tracklets is 5,217 which fits quite good with the expected value. The entries in this plot are the total numbers of found tracklets in this run. On the upper right one can see the distribution of clusters per tracklet which has a peak at the mean value of 21,27 clusters which fits good with the expected value as well. The entries in this case are the total number of tracks found in this run. If the number of tracks is multiplied with the mean value of the tracklets per track one gets approximately the number of tracklets found in the upper left plot. The lower left plot shows the average pulse height distribution of the signal. It is a profile plot of a bi-dimensional histogram where the deposited charge versus the timebin is plotted. This signal should of course reproduce the expected plot for charged particles in the TRD shown in Chapter 3. The peak of the plot at low timebins is caused by the contribution of avalanche electrons created in the vicinity of the anode wires in the amplification

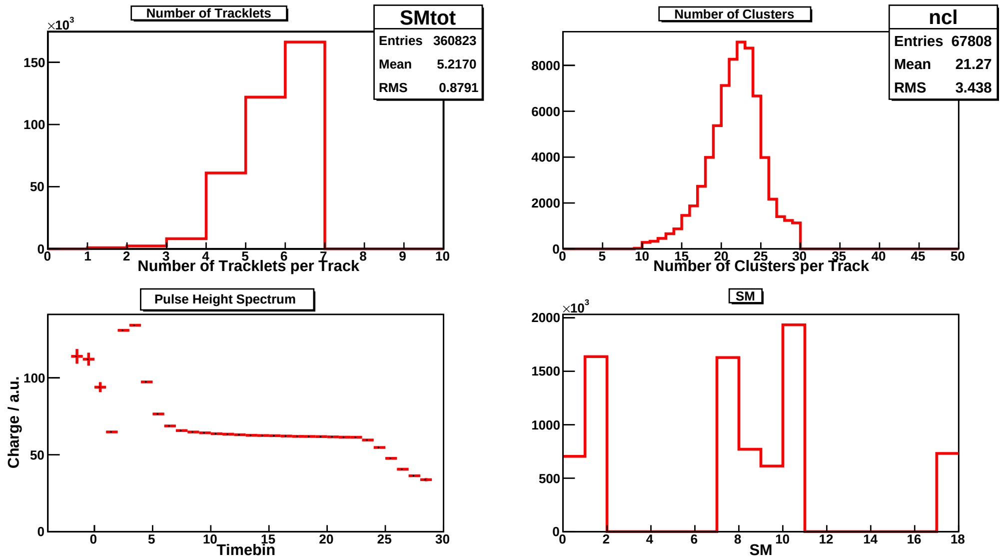

Figure 5.1: The Monitor Plot for Run 96287 as an example. The upper left plot shows the number of tracklets per track. In the upper right plot one can see the distribution of clusters per tracklet. The lower part shows the profile plot of the average pulse height plotted versus the timebin on the left and the total number of entries in the single sectors on the right.

region. The plateau refers to the drift region and has a drop at the border of the gas volume and the radiator part. A good overview can be seen in figure 5.2. With the good statistic available for this run the expectation is fulfilled. The lower right plot finally shows the distribution over the single sectors of the TRD. One can see that for sectors 1, 7 and 10 the number of entries is much higher than for the other sectors. If one keeps in mind the layout of the detectors in the spaceframe (see figure 3.1) it is obvious that those three sectors must have more entries because they are installed under a certain angle and do not lie in the horizontal plane, where the threshold energy for muons is bigger.

5.1.2 Single Sector Plots

For a detailed look into the performance of the TRD it is necessary to look at the performance of the single sectors and even the performance of the single detectors. In the single sector plots the main focus is set on the average pulse height spectrum of the signal for every sector. Therefore a bi-dimensional plot is made which can be seen in the middle panel of figure 5.2. The upper panel shows the corresponding profile plots which are constructed the same way like the single one for the whole detector in the monitor plot. The lower panel shows the total number of entries distributed over the single detectors of this sector. One would expect a more or less uniform distribution like it is shown for sector 0, which is the picture on the left side. But as one can see for the other sectors, there are groups of detectors which have a higher contribution than others. These groups can be identified, using the tables of chapter 4, as single layers of the supermodule.

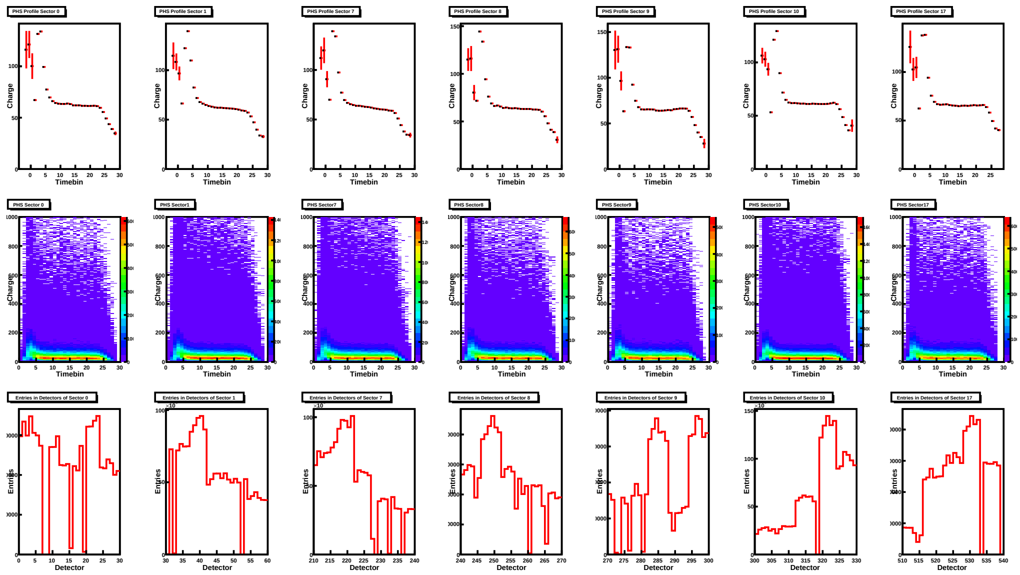

Figure 5.2: This plot shows in the upper panels the average pulse height distribution as a profile plot. One can see the maximum at low timebins which is caused by the higher charge deposited in the vicinity of the anode and corresponds to the amplification region. In the middle panels the bi-dimensional distribution of the average pulse height is shown for the single sectors. The lower panel shows the entries of clusters in the single sectors, from which one can conclude on the contribution of the single detectors.

There are two more single sector plots showing the distribution of tracklets per track and clusters per tracklet for every single supermodule. They can be found in the appendix for every run. For the chosen run 96287 the number of tracklets per track show a peak at 5 tracklets (sector 0 and sector 17) or at 6 tracklets (sector 1, 7, 8, 9 and 10), which can be seen in figure 5.4. For the number of clusters per tracklet one can see a Gaussian distribution with a mean around 22 clusters for all sectors, which one can see in figure 5.3.

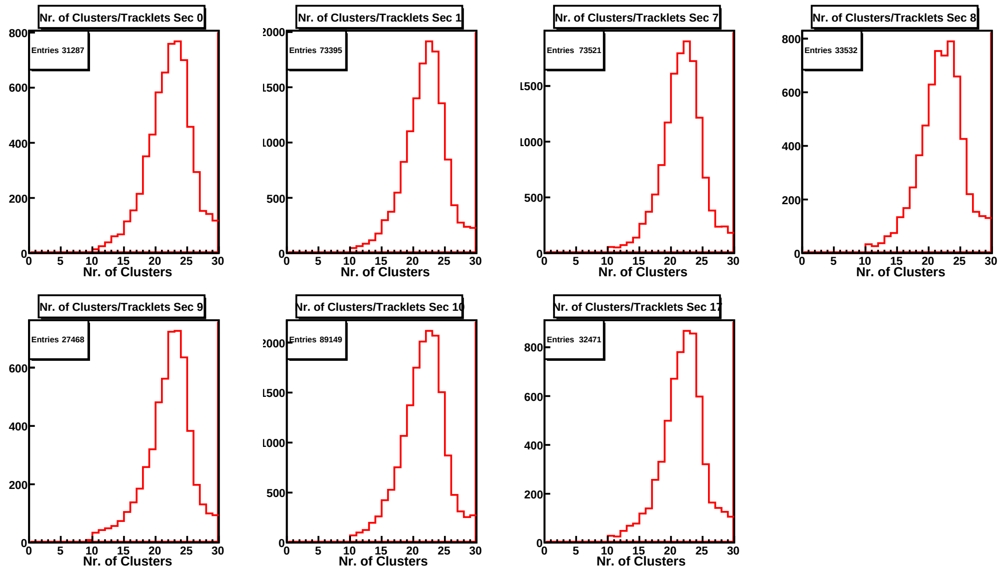

Figure 5.3: The distribution of clusters per tracklet is shown for the seven participating sectors. One can see a very uniform Gaussian distribution in every sector. The number of entries in every sector can be found in the embedded box.

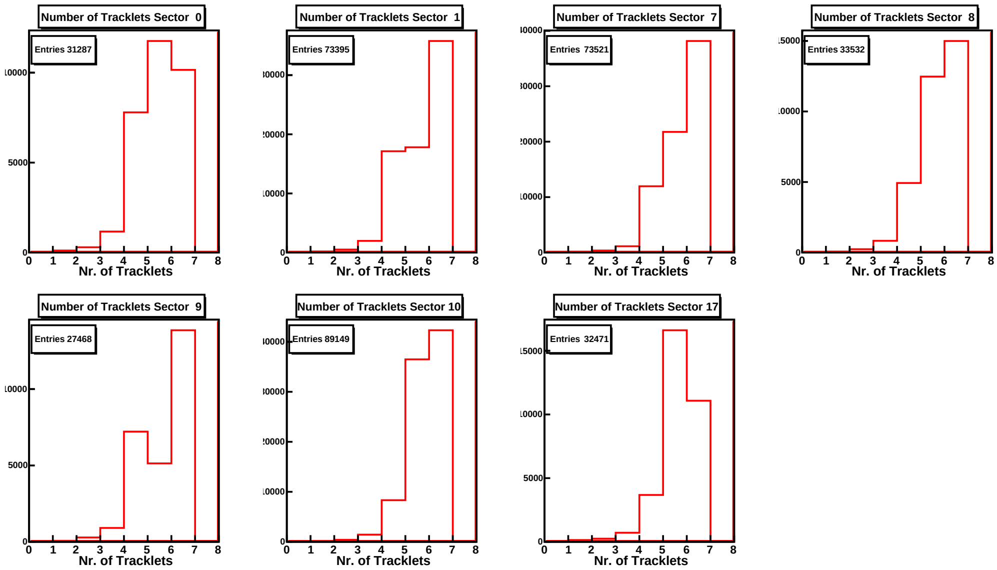

Figure 5.4: The distribution of tracklets per track is shown for the single sectors in this plot. One can see a maximum around 5 and 6 tracklets. The number of entries in the boxes are the same as for the clusters.

5.1.3 Single Detector Plots

For the performance of single readout chambers one can have a look on the bi-dimensional pulse height distribution for every single detector. The advantage is, that one can see immediately which detector did not take part in the run or did not produce any data. When looking at the high statistic runs 95741 to 99031, one can find some interesting behavior of the single detectors. The detector number N can be derived from the single plots by using the following expression:

$$N = x_i + n_S \cdot 30$$

where x_i $(i = 0, ..., 29)$ is the detector number derived from the plot when counting from left to right and n_S is the number of the sector (0, 1, 7, 8, 9, 10 or 17).
In sector 0 there are two detectors (15 and 19) which produce very low entries compared to the other detectors, which can be seen in figure 5.5. They have only about 3 % (detector 19) or 7 % (detector 15) of the entries compared to the other detectors. A similar behavior can be seen if one looks in the results for the lower statistic runs. These detectors can be identified as chamber L3C0_001 (detector 15) and chamber L1C1_018 (detector 19). There are no special comments for these chambers in the data base[49]. The problems might be caused by a too low high voltage either for the anode or for the drift electrodes.

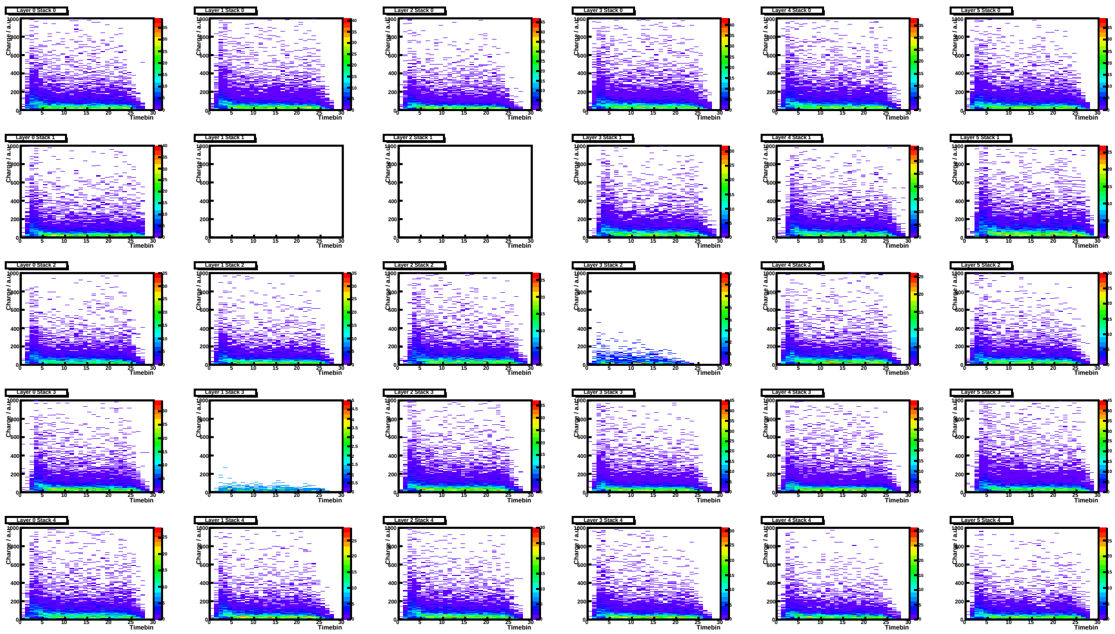

Figure 5.5: The single detectors of sector 0 with statistics from run 96287. One can see that the detectors 7 and 8 are either switched off or did not produce any data at all, but this was only found in run 96287. Detector 15 and 19 show a very small amount of entries compared to the other detectors. This is a regular occurring problem described in the text.

Sector 1 shows a similar behavior like sector 0 and can be seen in figure 5.6. There are chambers with very low entries compared to the other detectors visible in all runs. These detectors are detector 30, detector 32 and detector 52. The corresponding chambers are L0C1_28, L2C1_035 and L4C1_007. In the example plot of run 96287 the number of entries in detectors 30 and 32 is around 1 % compared to the number of entries in the other detectors and detector 52 has no entries at all.

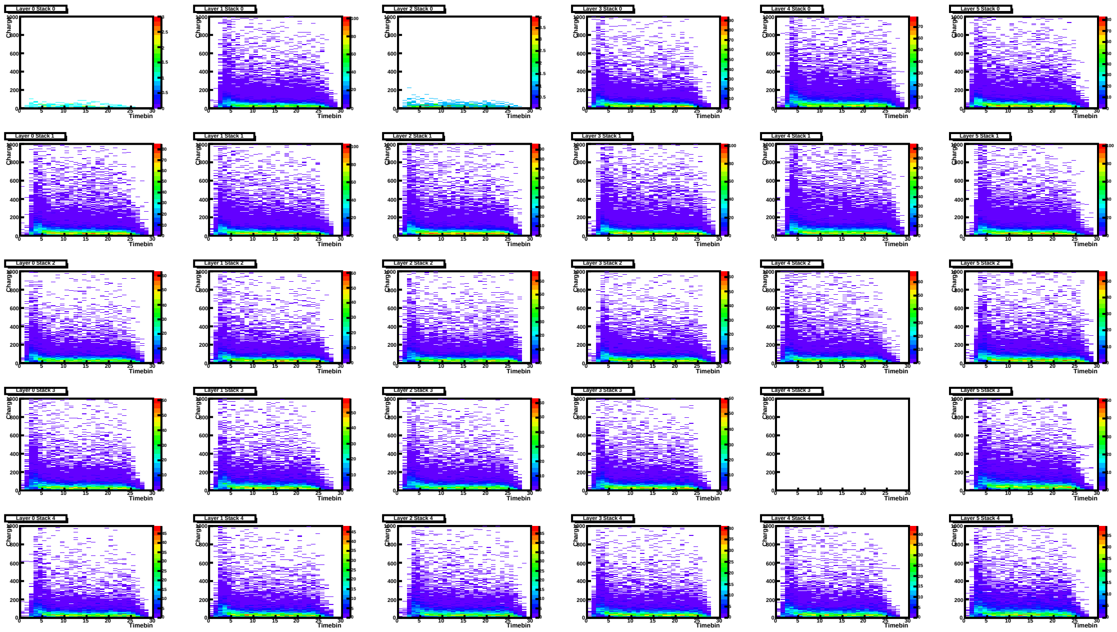

Figure 5.6: The single detectors of sector 1 with statistics from run 96287. One sees the low participation of detectors 30 and 32 and that detector 52 has no entries. All three detectors show a similar behavior in all of the Xe runs. In some runs all three have low entries (run 97873 and run 99031), in other runs one or two of them have no entries. The same can be found in the Ar runs of run period LHC09c as well.

In sector 7 one detector can be found that was switched off in most of the analyzed runs. It is detector 236 which is chamber L2C1_031. This chamber never delivered any data even when it was switched on concerning to the logbook entry. These has to be a deeper problem of the chamber which only can be analyzed when the chamber is exchanged during a maintenance period. Two detectors of stack 3, detector 228 and detector 232, have low entries in the order of 1 % compared to the other detectors that can be seen in figure 5.7. These chambers are L0C1_29 (detector 228) and L4C1_28 (detector 232).

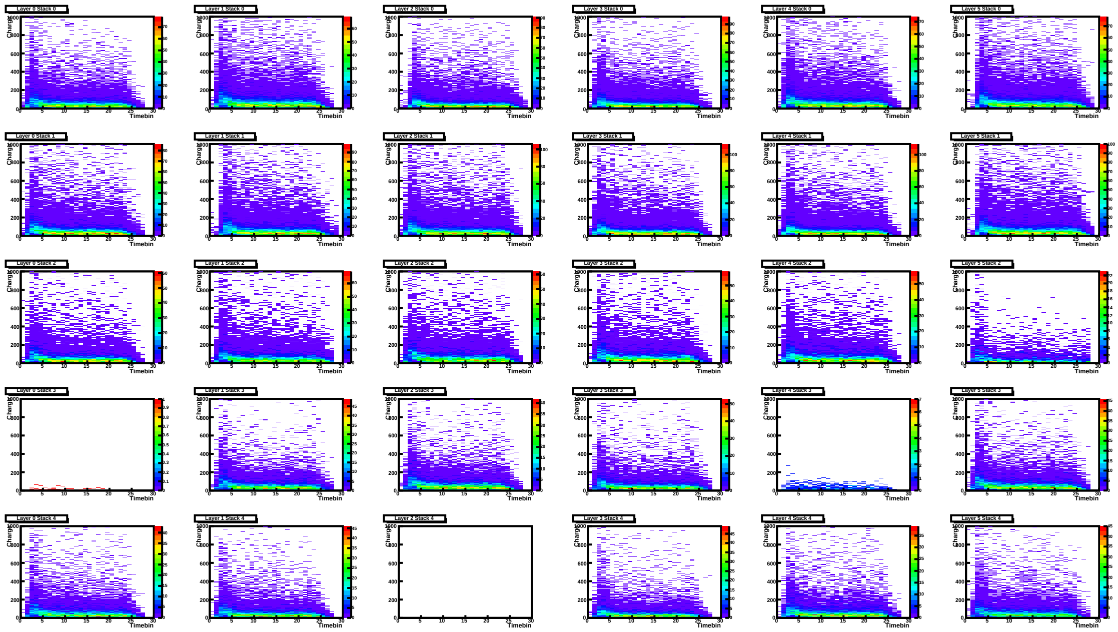

Figure 5.7: The single detectors of Sector 7 with statistics from the Xe run 96287. Detector 228 and detector 232 have low entries in this run and in all other Xe runs as well. Detector 236 which has no entries at all shows the same behavior in all analyzed runs, although it was not explicit turned off in some of the runs. The information if the detector was switched off can be found in the electronic logbook.

There is one detector in sector 8 with very low entries about 2 % in comparison to the other detectors and one detector with low entries in the order of 20 % of the other detector´s entries. The detectors of sector 8 can be seen in figure 5.8 The first one is detector 260, which is chamber L2C1_003, and the latter one is detector 265, which is chamber L1C1_002. None of these two were without entries in any of the high statistic runs. The low entries in detector 260 can not be verified in run 95741 but in all later runs.

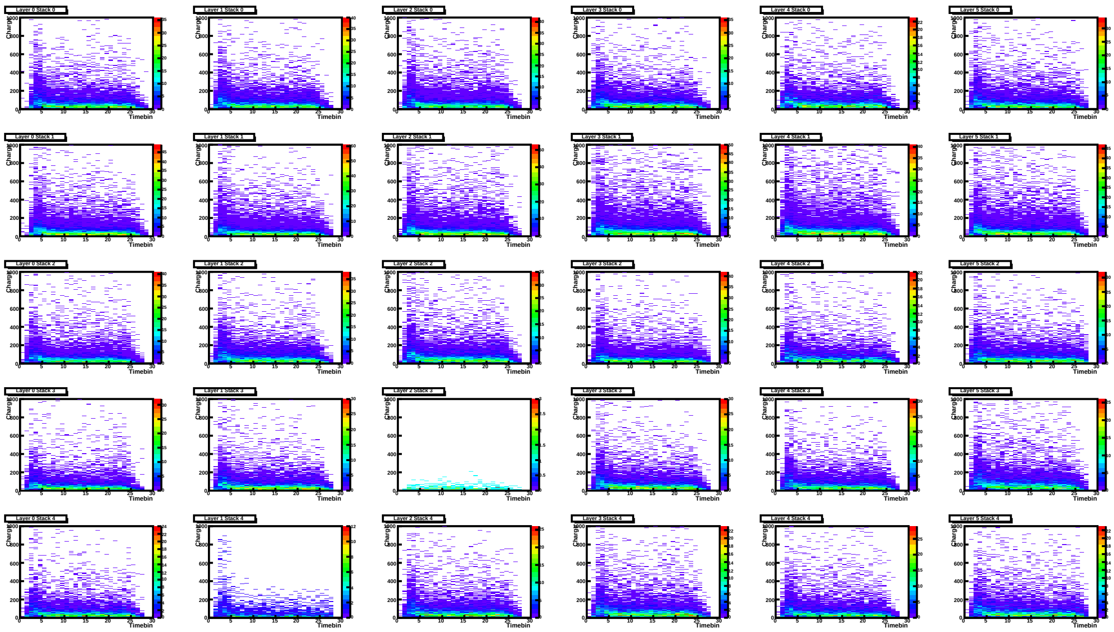

Figure 5.8: The single detectors of sector 8 with statistics from run 96287 are showed in this plot. One can see a small contribution of detector 260 and a reduced contribution of detector 265. Both show this in every Xe run, although they are never completely empty. The number of entries in detector 260 is of the order of 2 % compared to the others, whereas the number of entries in detector 265 is at least 20 % compared to the detectors in the same stack.

For the example run 96287 the single detector overview for sector 9, which can be seen in figure 5.9, there are in total 5 detectors with conspicuous entries. These are detector 272 and 273 of stack 0, detectors 276 and 280 of stack 1 and detector 289 of stack 3. The latter one still has a quite good performance as there are 50 % entries in comparison with the other detectors of the same stack. Only the very low entries of detector 273 (approximately 0,5 %) can be found in the other Xe runs as well. Therefore only chamber L3C1_15 (detector 273) remains suspicious. The other detectors might have failed during this single run.

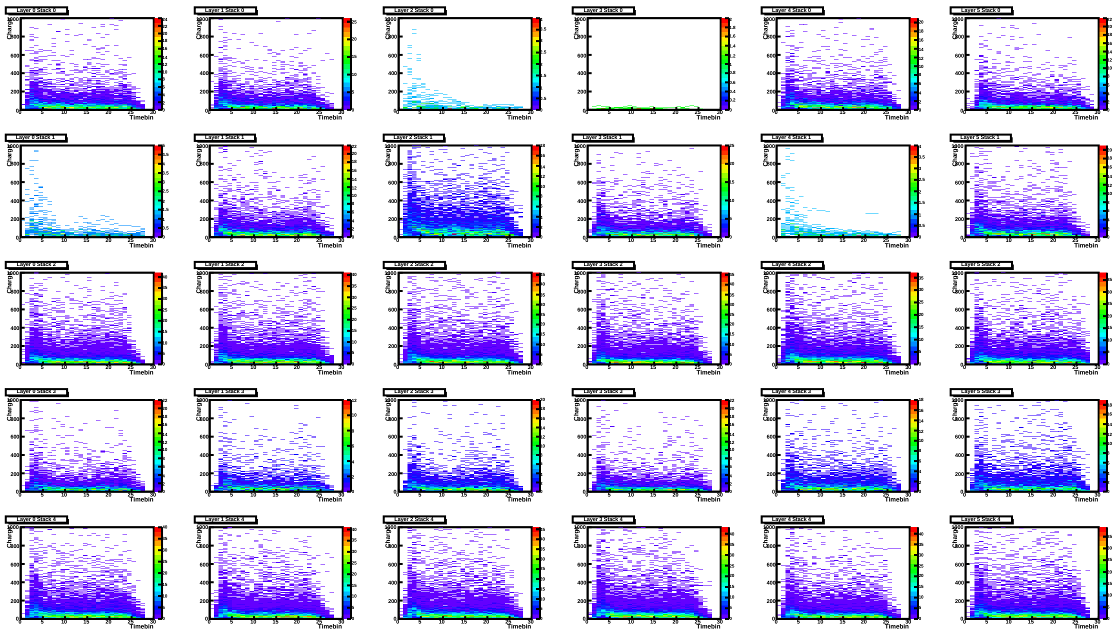

Figure 5.9: The single detectors of sector 9 for the high statistic Xe run 96287. The low entries in detector 273 are very obvious. For the detectors 272, 276 and 280 one can see a reduced number of entries but not as obvious as in detector 273. The smaller amount of entries in detector 289 can only be found when looking into the plot statistics, which show 6600 entries for this detector but around 11000 entries for the neighboring detectors of the same stack.

Sector 10 shows a very nice behavior with lots of entries that can be seen in figure 5.10. There is only detector 318 (chamber L0C1_058) which is without entries, but it is not clear if this one was switched off or if there are problems, because in run 98371 it appears with the same number of entries compared to its stack neighbors. Nevertheless one very interesting issue should be mentioned. If one looks at the distribution of entries throughout a stack, it can be seen that there seems to be an order. Detectors of stack 0 have the smallest number of entries followed by stack 1, stack 2 and stack 4. The detectors of stack 3 have a very high number of entries, approximately 30 % more than the sectors' average. This can be seen in figure 5.2 as well in the distribution of total number of entries in the sector. During the Ar run of run period LHC09c a fraction of runs show no entries in the complete sector at all, although sector 10 was proposed in the logbook to take part in these run. Maybe a failure in the reconstruction occured to prevent this sectors information to be processed.

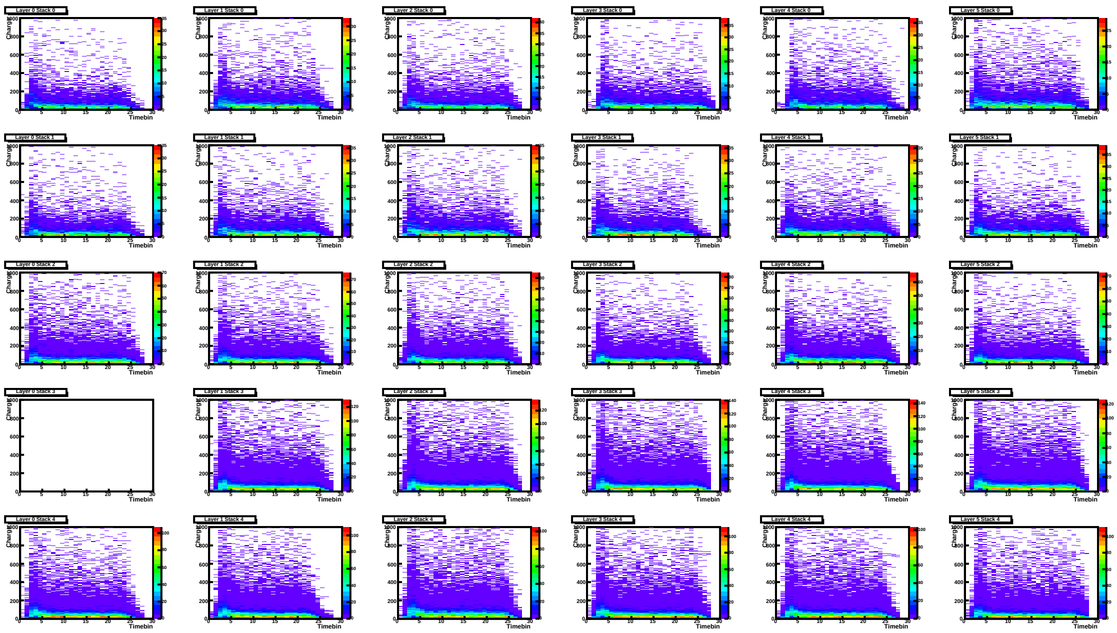

Figure 5.10: The single detectors of sector 10 with statistics of run 96287. One can see a quite uniform filling of all detectors, except for detector 318 which has no entries at all. Nevertheless one can find that the detectors of stack 3 show a slightly higher number of entries compared to the other detectors in the sector. The missing detector 318 was found in run 97873 and run 99031 as well.

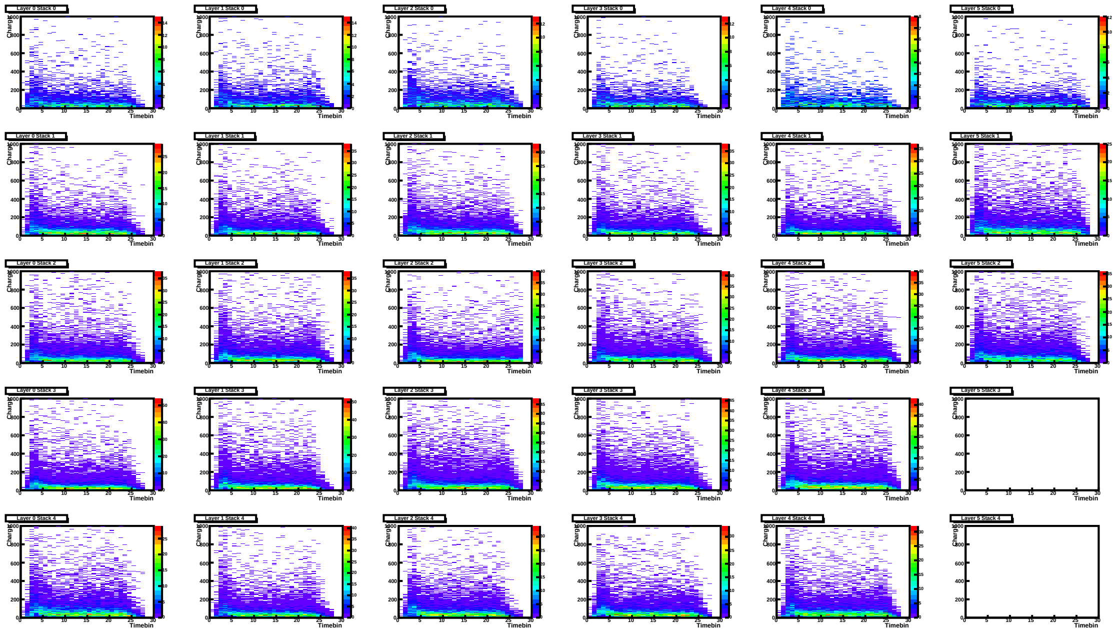

Figure 5.11: The single detectors of sector 17 with the statistics of run 96287. One can see that the detectors 533 and 539 do not contain any entries. This can be reproduced in all of the Xe runs, whereas in run 97873 detector 521 is without entries as well.

Finally looking at sector 17 it shows two detectors which are without any entries in all the analyzed runs. They are detector 533 and 539, both chambers of layer 5, namely L5C1_010 and L5C1_033. All other detectors yield reliable values for their entries. Except for one Xe run (97873), in which detector 521 has no entries as well. All three detectors belong to layer 5. In the older Ar runs detector 539 was switched off frequently. The overview for sector 17 can be found in figure 5.11.

5.2 Analysis of run period LHC08d

In the following section an overview of the monitor plots from run period LHC08d is given. Some of these runs suffer from poor statistic, but in most cases the expected trends can be seen. The subsections contain information about the date of the corresponding run, its duration measured in seconds and if a magnetic field was applied or not. At the end of the section there is an overview over the number of clusters, the number of tracklets and the number of tracks which were found in the runs from this run period. These information are summarized in table 5.1. Another summary table containing the number of tracks and the duration in seconds can be found in the appendix.

5.2.1 Run 60283

Run 60283 took place on September 19th, 2008 without magnetic field. The duration of this run was 36952 s, that makes it the longest analyzed run of run period LHC08d. This run was analyzed using the debug information.

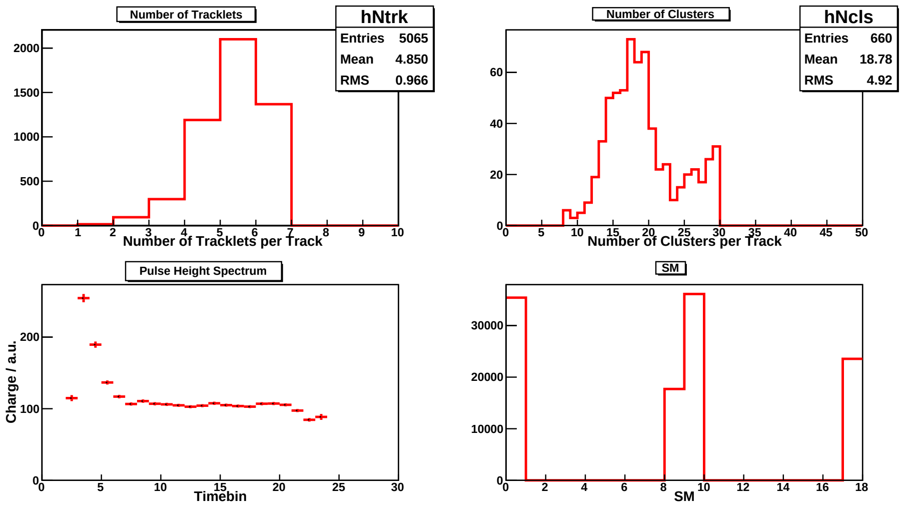

Figure 5.12: Monitor Plot run 60283

5.2.2 Run 60419

Run 60419 took place on September 22nd, 2008 without magnetic field. The duration of this run was 6305 s. This run was analyzed using the debug information.

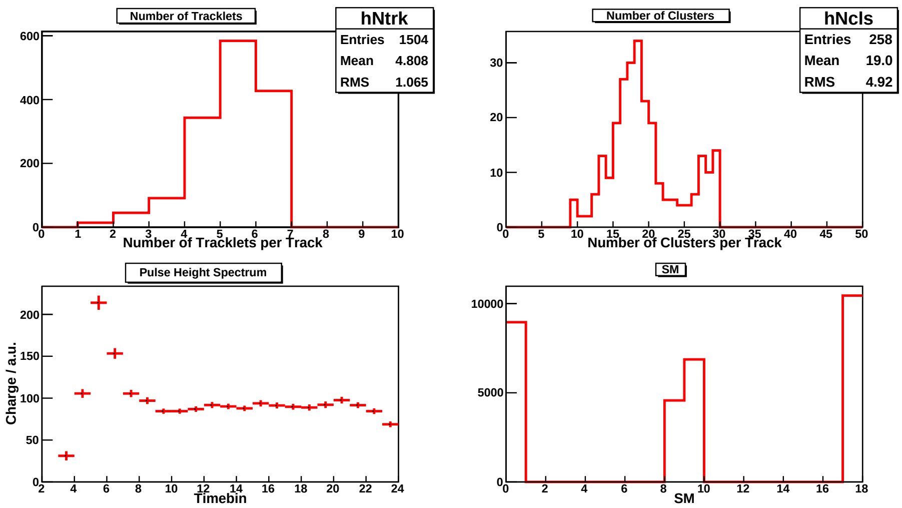

Figure 5.13: Monitor Plot Run 60419

5.2.3 Run 60517

Run 60517 took place on September 23rd, 2008 without magnetic field. The duration of this run was only 15s, that makes it the shortest analyzed run overall. This run was analyzed using the debug information.

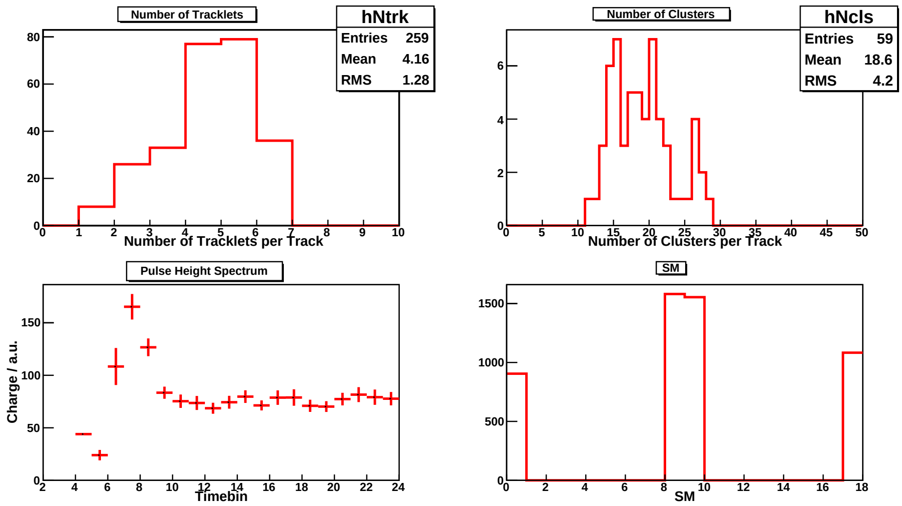

Figure 5.14: Monitor Plot Run 60517

5.2.4 Run 60545

Run 60545 took place on September 23rd, 2008 without magnetic field as well. The duration of this run was 5955 s. The analysis plot was mainly used as reference. This run was analyzed using the debug information.

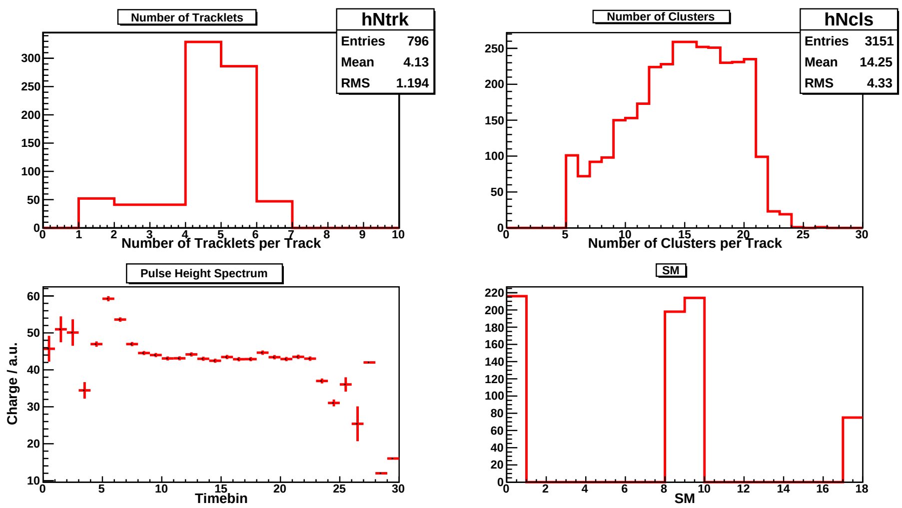

Figure 5.15: Monitor Plot Run 60545

5.2.5 Run 60668

Run 60668 took place on September 24th, 2008 without magnetic field. The duration of this run was 2083 s. This run was analyzed using the debug information.

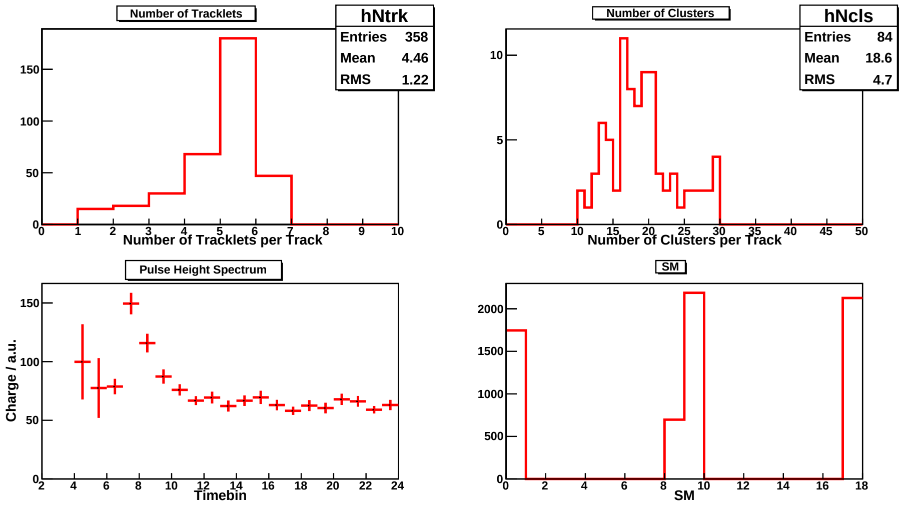

Figure 5.16: Monitor Plot Run 60668

5.2.6 Run 60813

Run 60813 took place on September 25th, 2008 without magnetic field. The duration of this run was 6299 s.

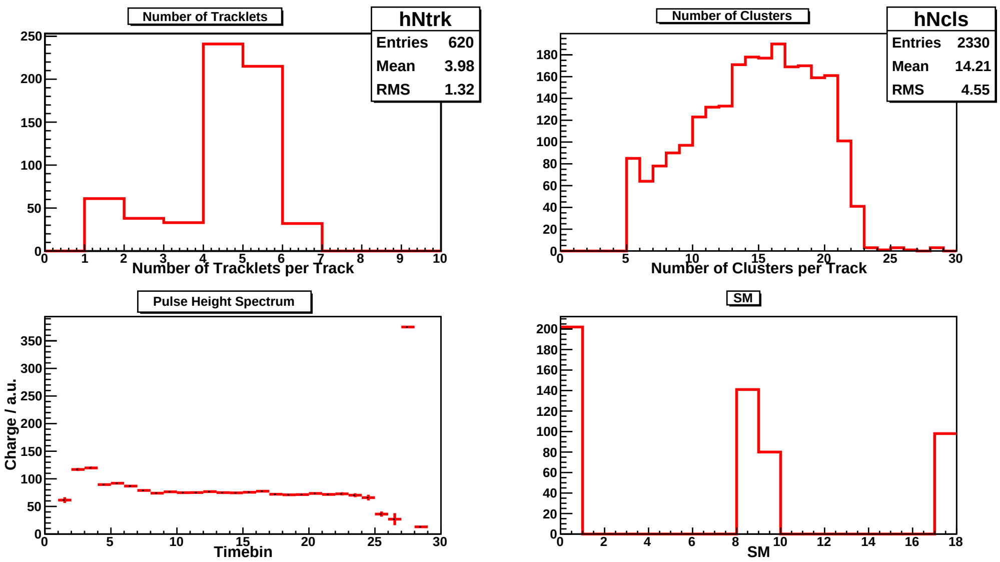

Figure 5.17: Monitor Plot Run 60813

5.2.7 Run 60920

Run 60920 took place on September 26th, 2008 without magnetic field. The duration of this run was 9601 s.

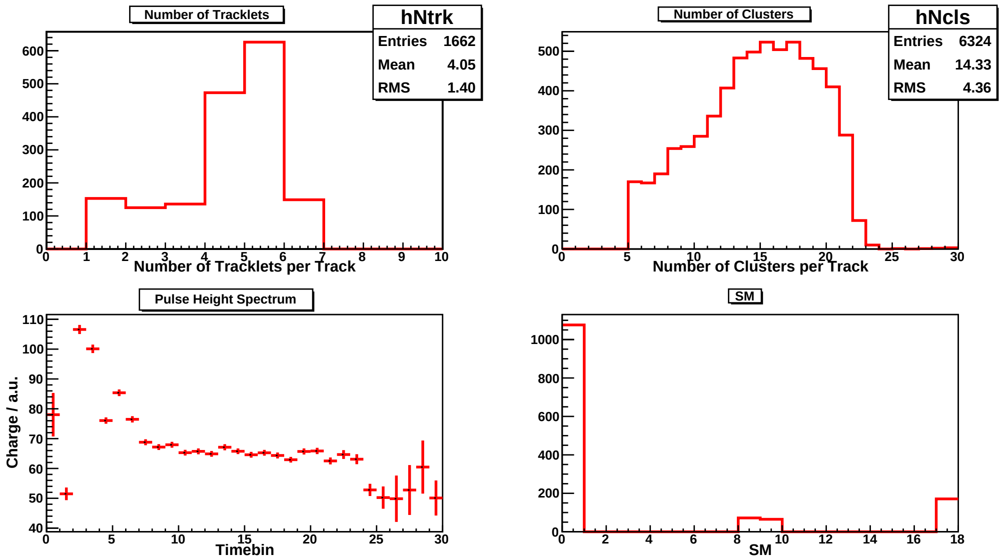

Figure 5.18: Monitor Plot Run 60920

5.2.8 Run 60977

Run 60977 took place on September 27th, 2008 without magnetic field. The duration of this run was 2693 s.

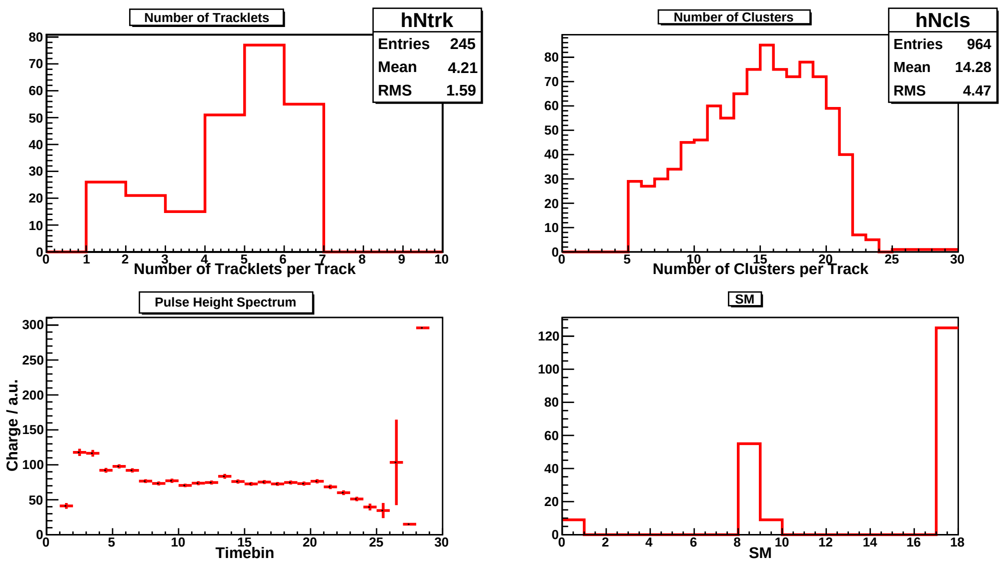

Figure 5.19: Monitor Plot Run 60977

5.2.9 Run 60984

Run 60984 took place on September 27th, 2008 without magnetic field. The duration of this run was 12451 s.

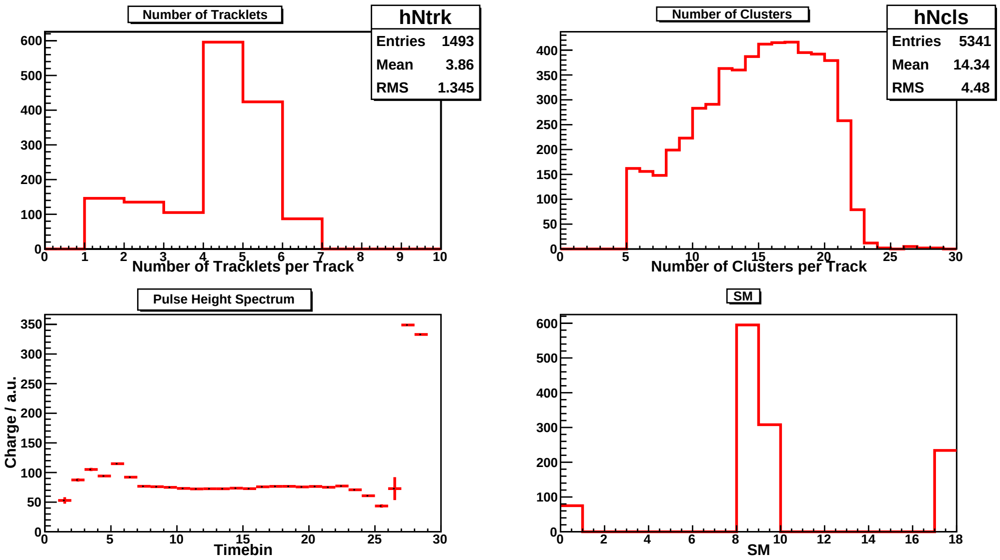

Figure 5.20: Monitor Plot Run 60984

5.2.10 Run 60993

Run 60993 took place on September 27th, 2008 without magnetic field as well. The duration of this run was 2946 s.

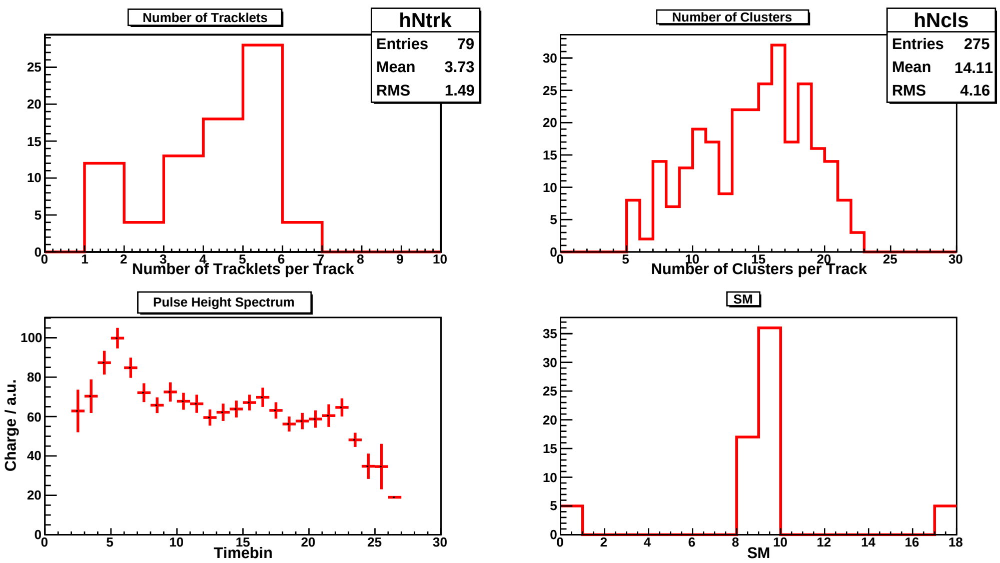

Figure 5.21: Monitor Plot Run 60993

5.2.11 Run 61048

Run 61048 took place on September 28th, 2008 without magnetic field. The duration of this run was 12050 s.

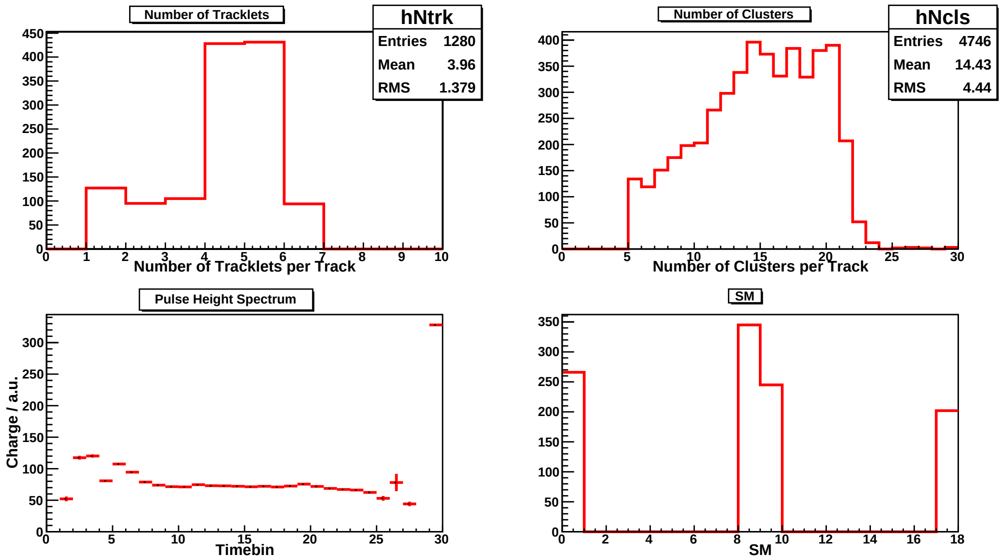

Figure 5.22: Monitor Plot Run 61048

5.2.12 Run 61120

Run 61120 took place on September 29th, 2008 without magnetic field. The duration of this run was 18590 s.

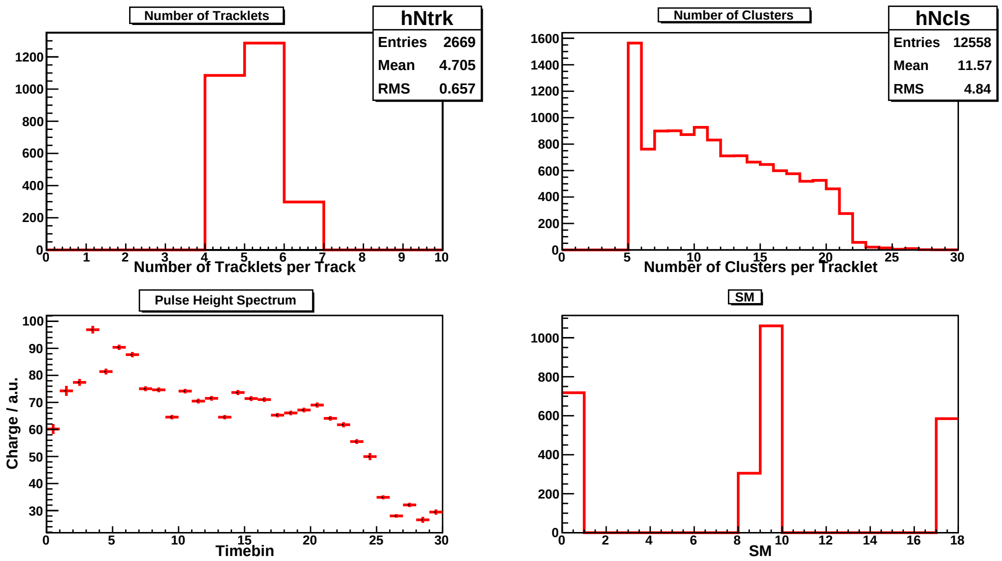

Figure 5.23: Monitor Plot Run 61120

5.2.13 Run 61694

Run 61694 took place on October 3rd, 2008 without magnetic field. The duration of this run was 2872 s. The run was stopped because of problems with detector S3L2 in sector 8.

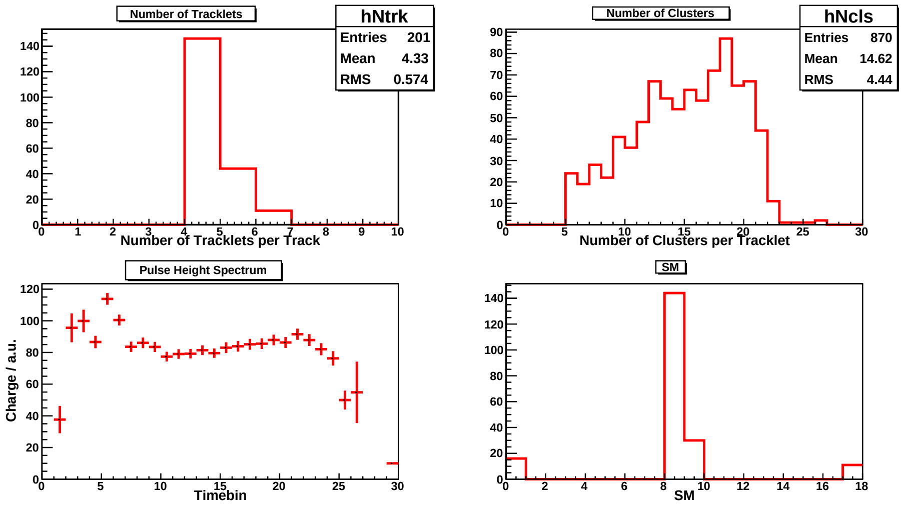

Figure 5.24: Monitor Plot Run 61694

5.2.14 Run 61796

Run 61796 took place on October 5th, 2008 without magnetic field. The duration of this run was 4507 s.

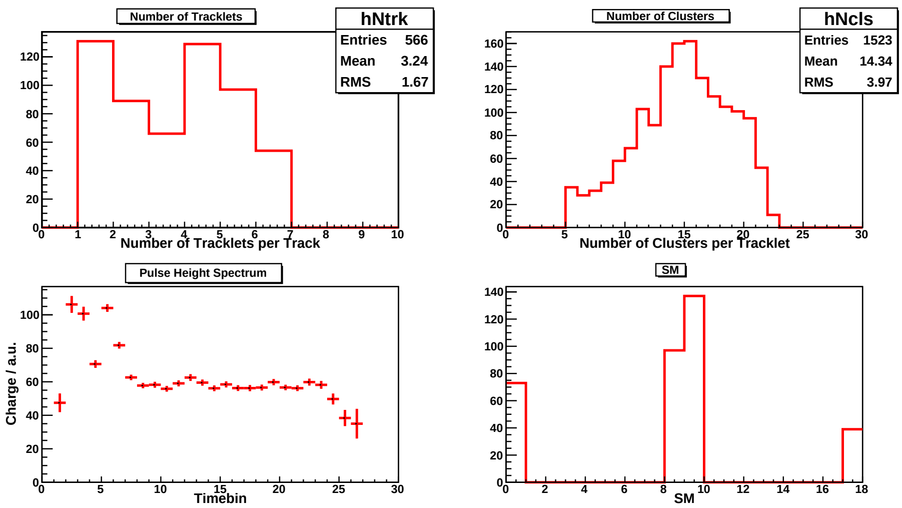

Figure 5.25: Monitor Plot Run 61796

5.2.15 Run 61858

Run 61858 took place on October 6th, 2008 without magnetic field. The duration of this run was 3900 s.

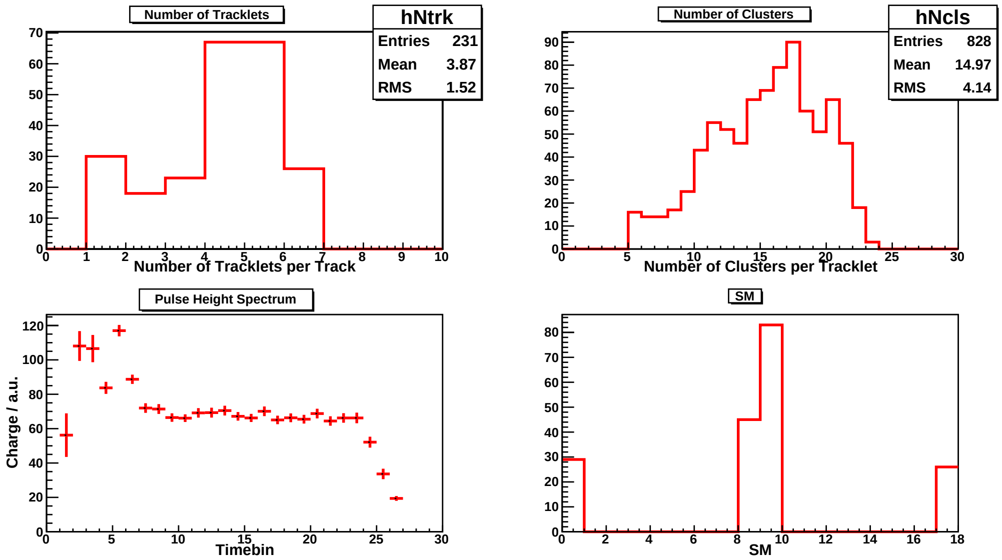

Figure 5.26: Monitor Plot Run 61858

5.2.16 Run 61869

Run 61869 took place on October 6th, 2008 without magnetic field. The duration of this run was 1772s.

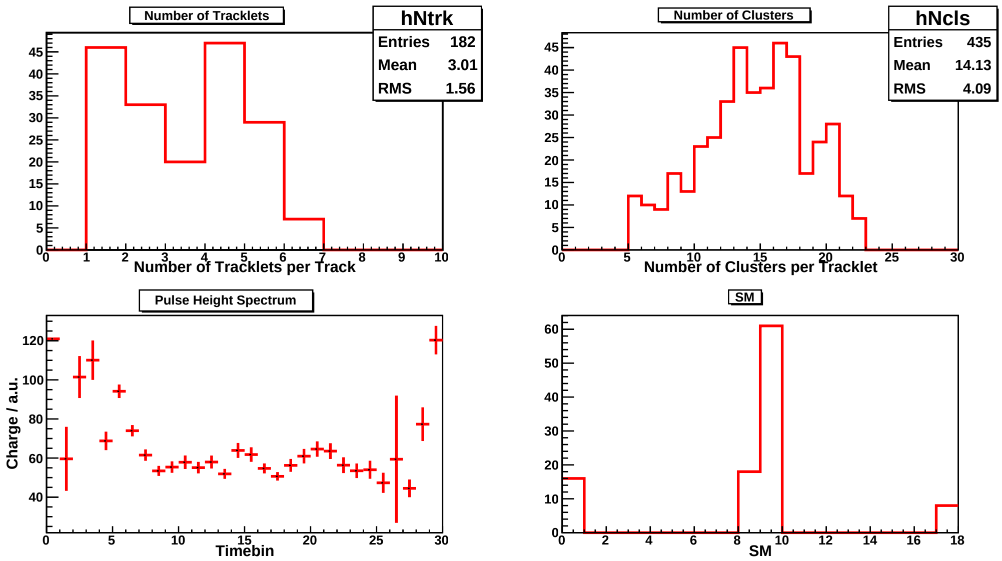

Figure 5.27: Monitor Plot Run 61869

5.2.17 Run 61872

Run 61872 took place on October 6th, 2008 without magnetic field as well. The duration of this run was 2879 s.

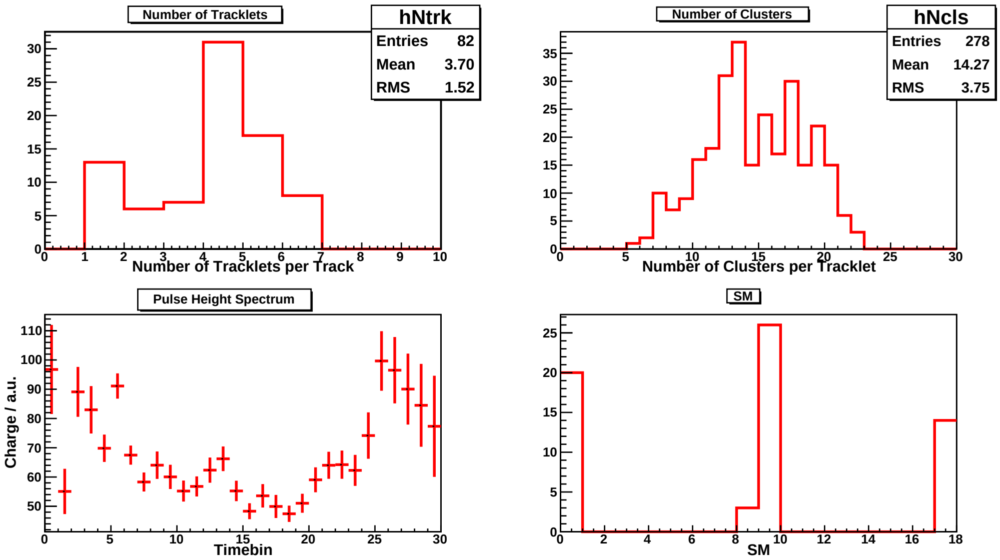

Figure 5.28: Monitor Plot Run 61872

5.2.18 Run 62006

Run 62006 took place on October 7th, 2008 with a magnetic field of + 0,5 T. The duration of this run was 9713 s.

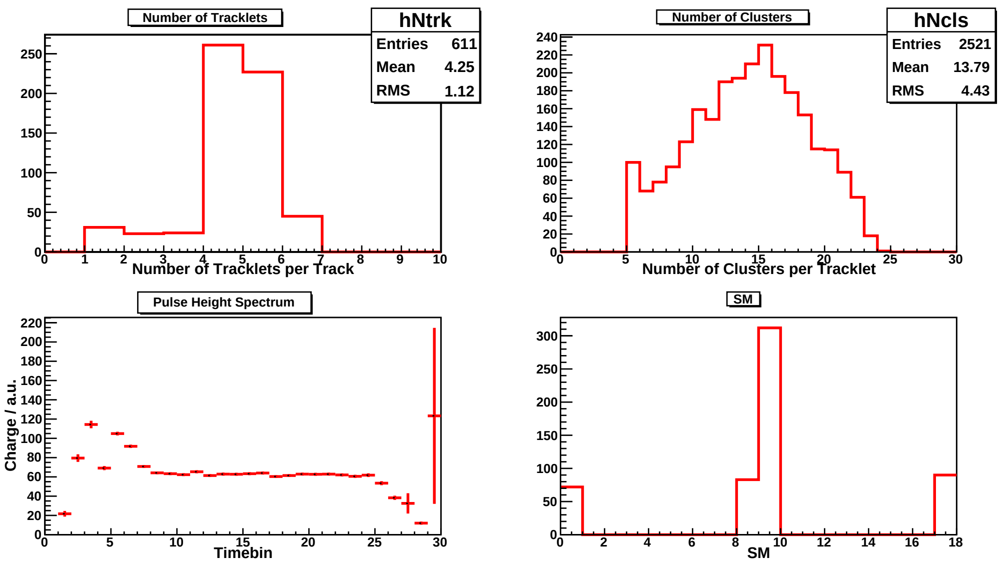

Figure 5.29: Monitor Plot Run 62006

5.2.19 Run 62029

Run 62029 took place on October 7th, 2008 with a magnetic field of + 0,5 T as well. The duration of this run was 10409 s.

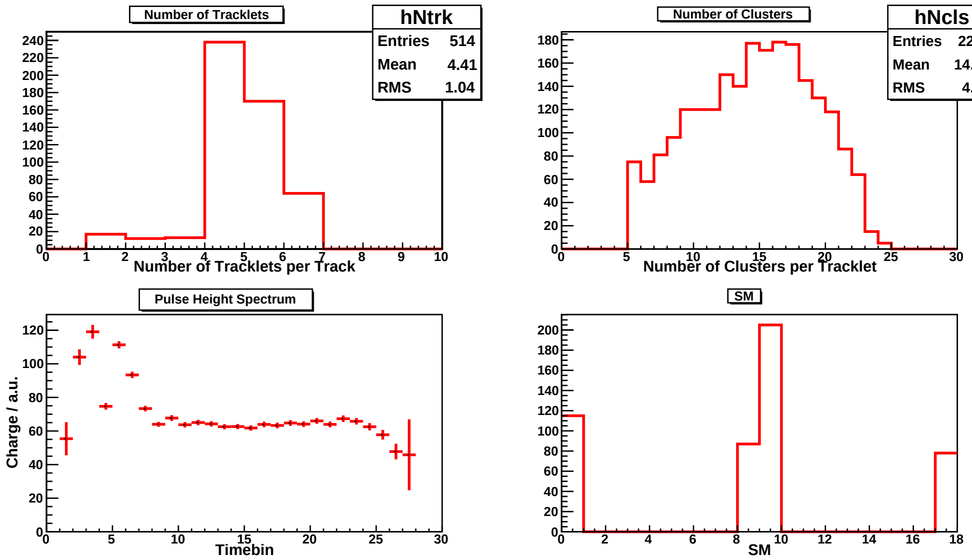

Figure 5.30: Monitor Plot Run 62029

5.2.20 Run 62065

Run 62065 took place on October 8th, 2008 without magnetic field. The duration of this run was 4431 s.

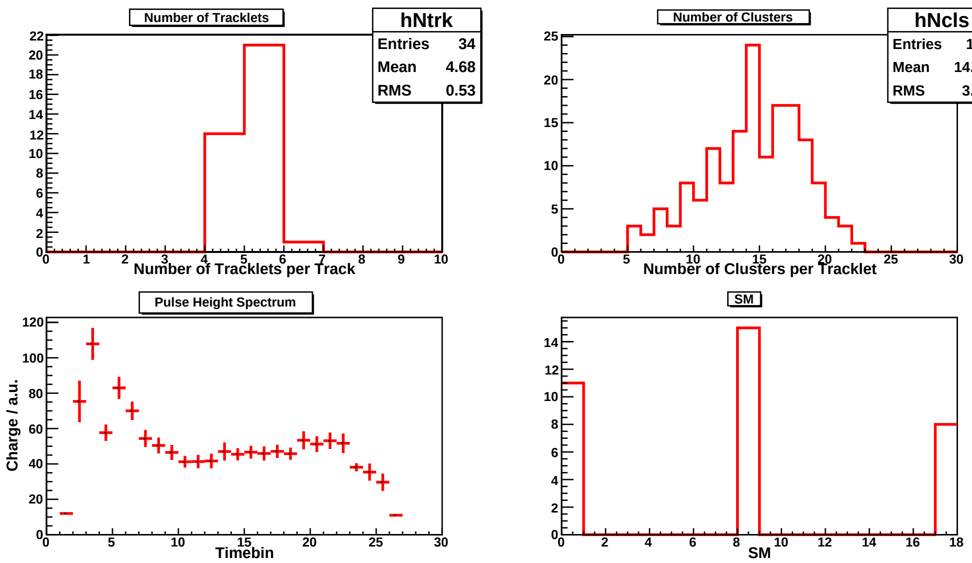

Figure 5.31: Monitor Plot Run 62065

5.2.21 Run 62084

Run 62084 took place on October 8th, 2008 with a magnetic field of - 0,5 T. The duration of this run was 16914 s.

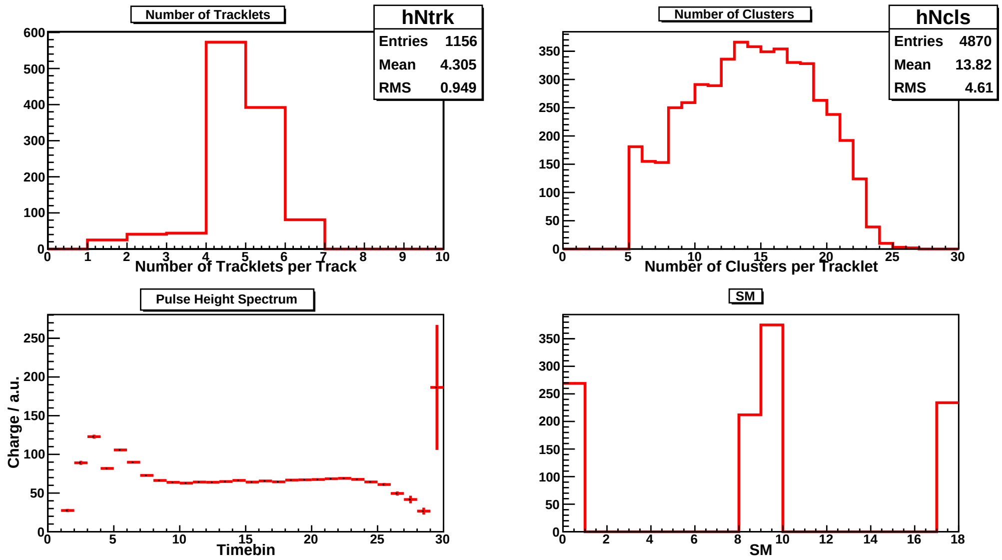

Figure 5.32: Monitor Plot Run 62084

5.2.22 Run 62102

Run 62102 took place on October 8th, 2008 with a magnetic field of - 0,5 T as well. The duration of this run was 19508 s.

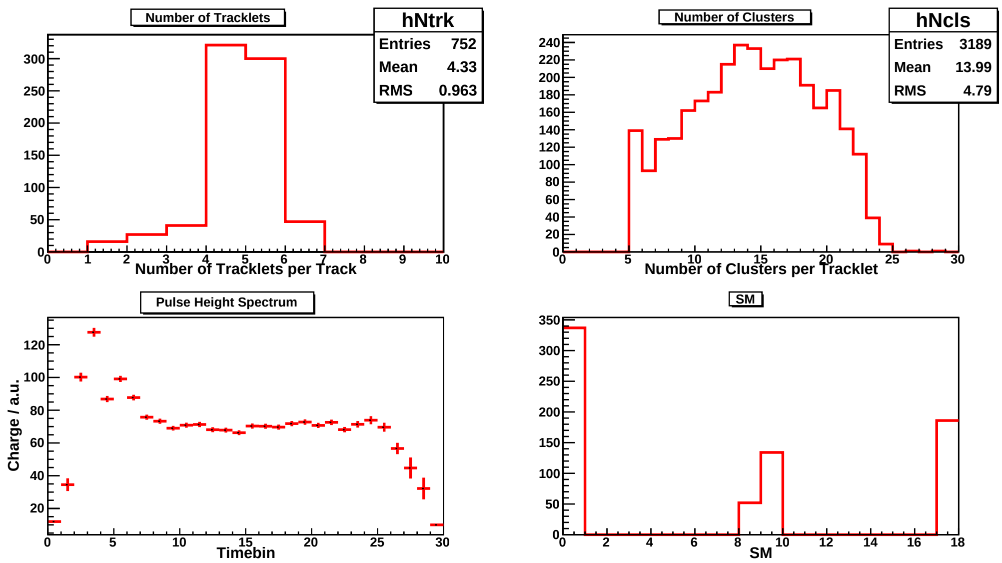

Figure 5.33: Monitor Plot Run 62102

5.2.23 Run 62414

Run 62414 took place on October 10th, 2008 without magnetic field. The duration of this run was 9820 s.

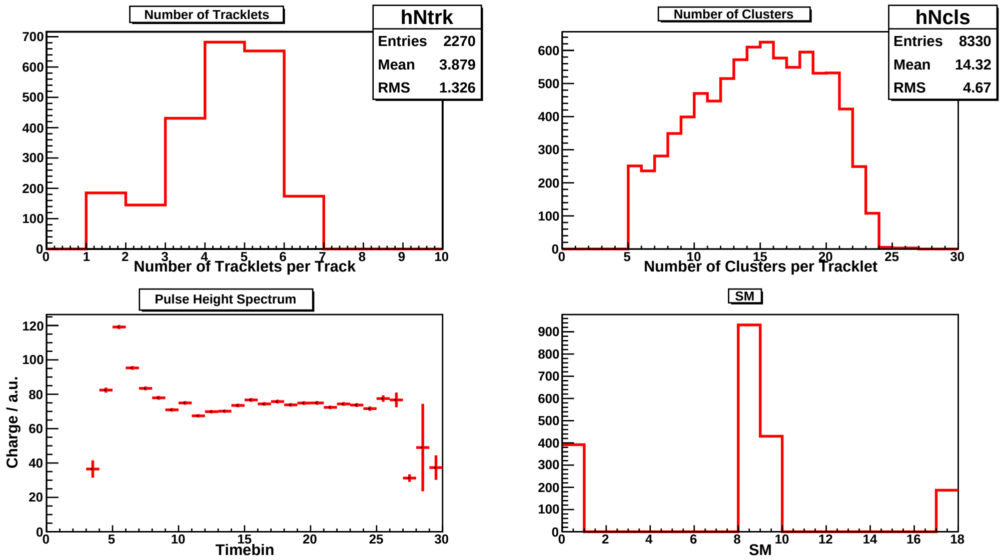

Figure 5.34: Monitor Plot Run 62414

5.2.24 Run 62434

Run 62434 took place on October 10th, 2008 without magnetic field as well. The duration of this run was 5789 s.

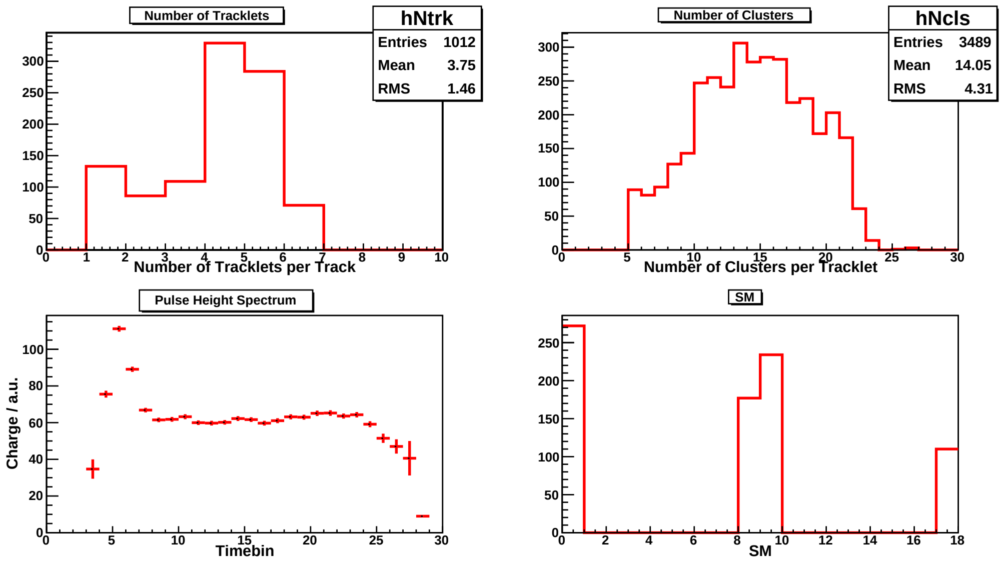

Figure 5.35: Monitor Plot Run 62434

5.2.25 Run 62439

Run 62439 took place on October 11th, 2008 without magnetic field. The duration of this run was 9304 s.

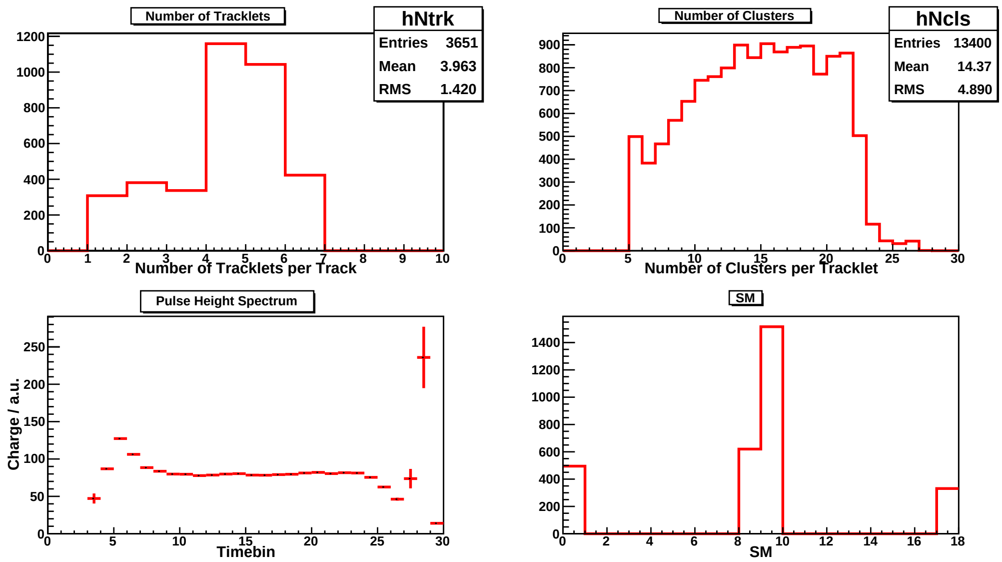

Figure 5.36: Monitor Plot Run 62439

5.2.26 Run 62512

Run 62512 took place on October 12th, 2008 without magnetic field. The duration of this run was 8316 s.

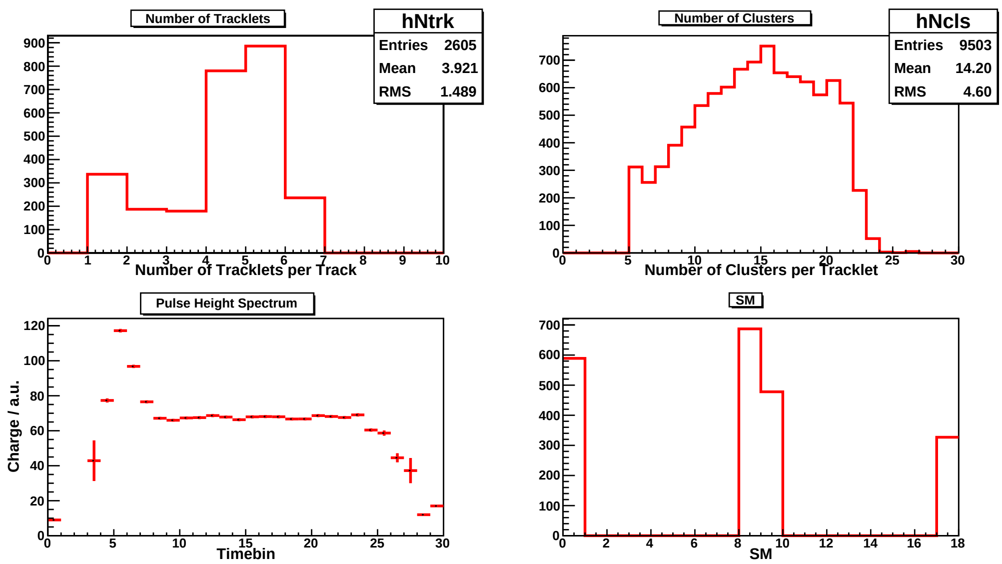

Figure 5.37: Monitor Plot Run 62512

5.2.27 Run 62517

Run 62517 took place on October 12th, 2008 without magnetic field. The duration of this run was 4437 s.

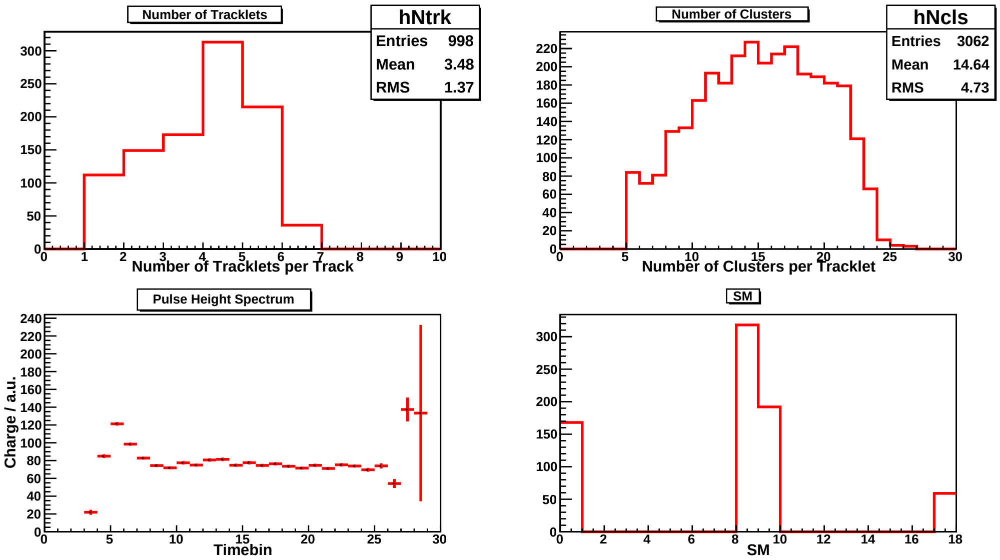

Figure 5.38: Monitor Plot Run 62517

5.2.28 Run 62521

Run 62521 took place on October 12th without magnetic field as well. The duration of this run was 12899 s.

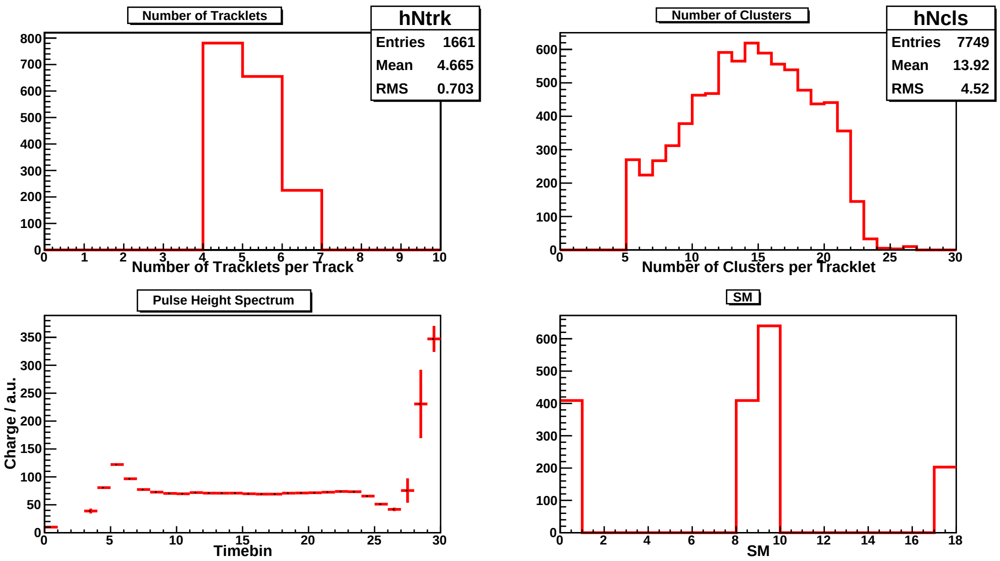

Figure 5.39: Monitor Plot Run 62521

5.2.29 Overview Run period LHC08d

In the following table the number of clusters, the number of tracklets and the number of tracks are summarized for each run of run period LHC08d.

Run Number	Number of Clusters	Number of Tracklets	Number of Tracks
60283	112758	5065	660
60419	30854	1504	258
60517	5123	259	59
60545	31393	3151	796
60668	6758	358	84
60813	30973	2330	620
60920	87321	6324	1662
60977	12743	964	245
60984	71868	5341	1493
60993	3776	275	79
61048	64816	4746	1280
61120	137524	12558	2669
61694	11801	870	201
61796	21193	1523	566
61858	11990	828	231
61869	6041	435	182
61872	3941	278	82
62006	33688	2521	611
62029	30237	2225	514
62065	2199	159	34
62084	64299	4870	1156
62102	42460	3189	752
62414	105085	8330	2270
62434	47017	3489	1012
62439	174640	13400	3651
62512	129131	9503	2605
62517	40256	3062	998
62521	101877	7749	1661

Table 5.1: Overview of the number of clusters, the number of tracklets and the number of tracks produced during the cosmic run period LHC08d.

5.3 Analysis of run period LHC09c

This period of cosmic analysis started in August 2009 and proceeded until November 2009 just before the start of collisions in the LHC. In this run period all seven sectors were installed and participated in data taking. For the runs 95741 to 99031 the fill gas of the TRD was exchanged from Argon to Xenon. In these Xe runs the magnetic field at the foreseen strength of +0,2 T was applied as well. Furthermore there was a change in the AliRoot version used for both reconstruction and analysis starting from run 85618. At the end of this section there will be a summary table of the number of clusters, the number of tracklets and the number of tracks found in all of the runs from the given run period. Similar to section 5.2 there will be an additional summary table containing the number of tracks and the run duration, which can be found in the appendix as well. Excluded chambers are mentioned in the text whenever information were given in the electronic logbook.

5.3.1 Run 81043

Run 81043 took place on August 22nd, 2009 without magnetic field. The duration of this run was 28654 s. Chamber S4L2 in sector 7 was excluded in this run.

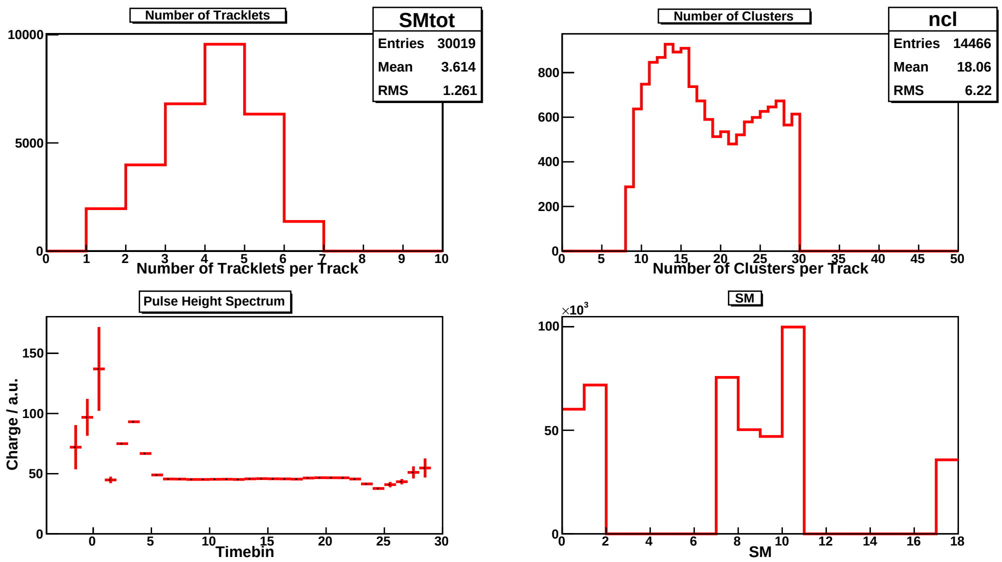

Figure 5.40: Monitor Plot Run 81043

5.3.2 Run 81116

Run 81116 took place on August 23rd, 2009 without magnetic field. The duration of this run was 3858 s. This run was used for testing the plotting macro.

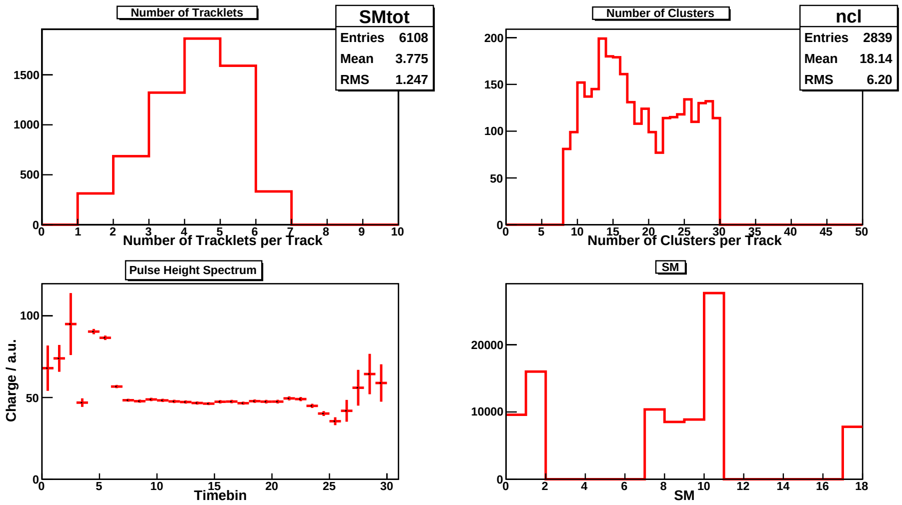

Figure 5.41: Monitor Plot Run 81116

5.3.3 Run 85618

Run 85618 took place on September 11th, 2009 without magnetic field. The duration of this run was 20744 s. In this run the chambers S4L2 of sector 7, S0L4 of sector 8 and S3L5 of sector 17 were turned off.

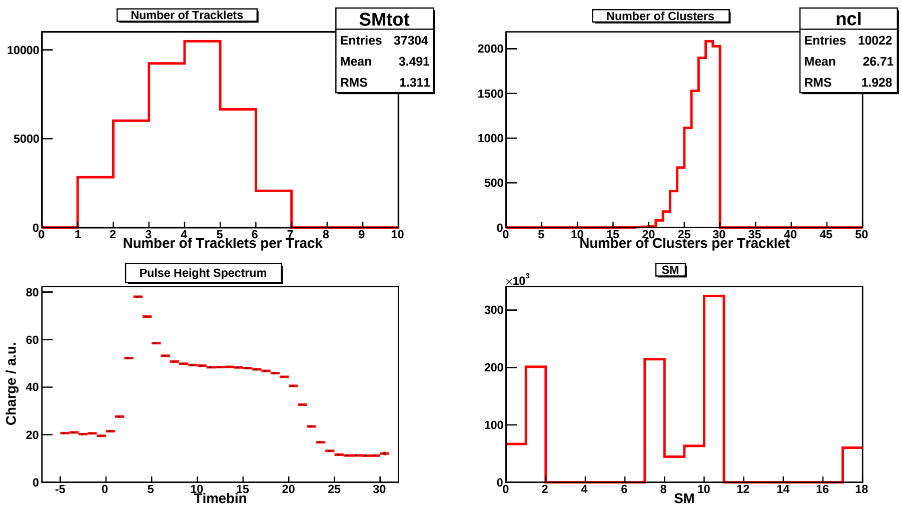

Figure 5.42: Monitor Plot Run 85618

5.3.4 Run 85657

Run 85657 took place on September 12th, 2009 without magnetic field. The duration of this run was 3662 s. In this run the chambers S4L2 of sector 7, S0L4 of sector 8 and S3L5 of sector 17 were turned off.

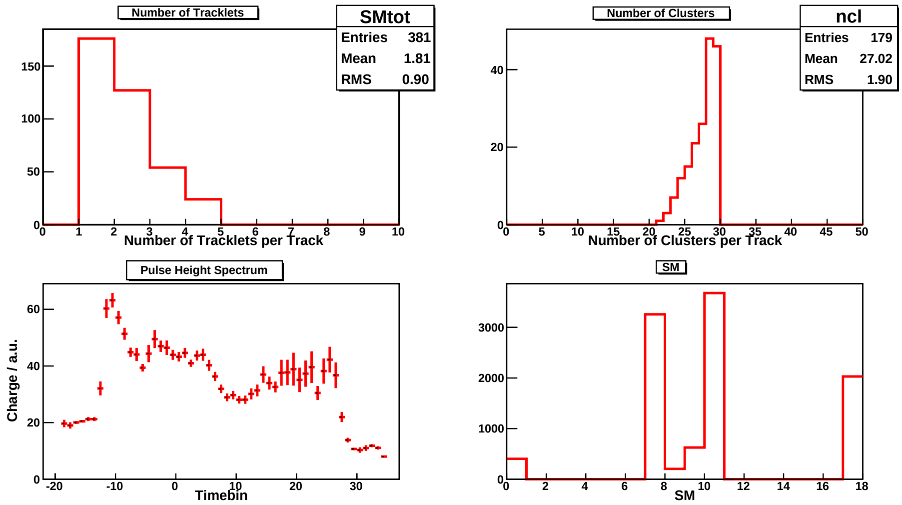

Figure 5.43: Monitor Plot Run 85657

5.3.5 Run 85658

Run 85658 took place on September 12th, 2009 without magnetic field. The duration of this run was 5391 s. In this run the chambers S4L2 of sector 7, S0L4 of sector 8 and S3L5 of sector 17 were turned off.

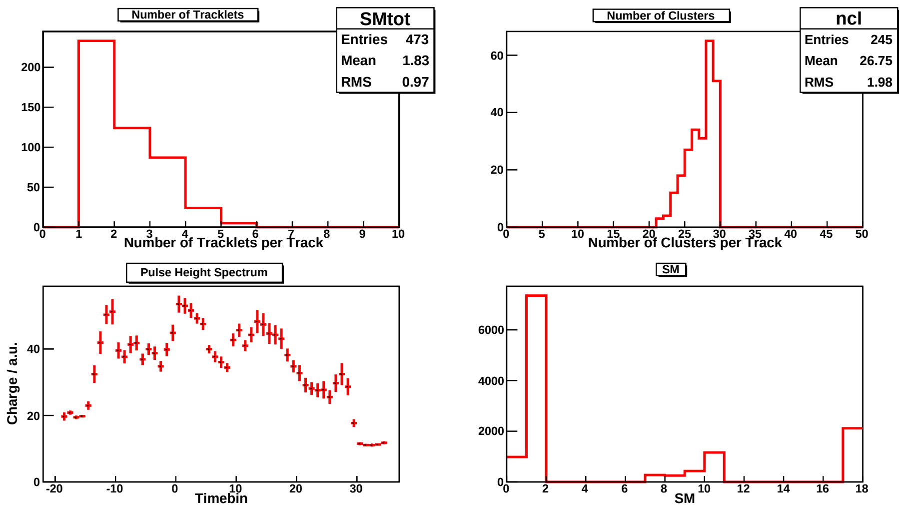

Figure 5.44: Monitor Plot Run 85658

5.3.6 Run 85660

Run 85660 took place on September 12th, 2009 without magnetic field as well. The duration of this run was 8302 s. In this run the chambers S4L2 of sector 7, S0L4 of sector 8 and S3L5 of sector 17 were turned off.

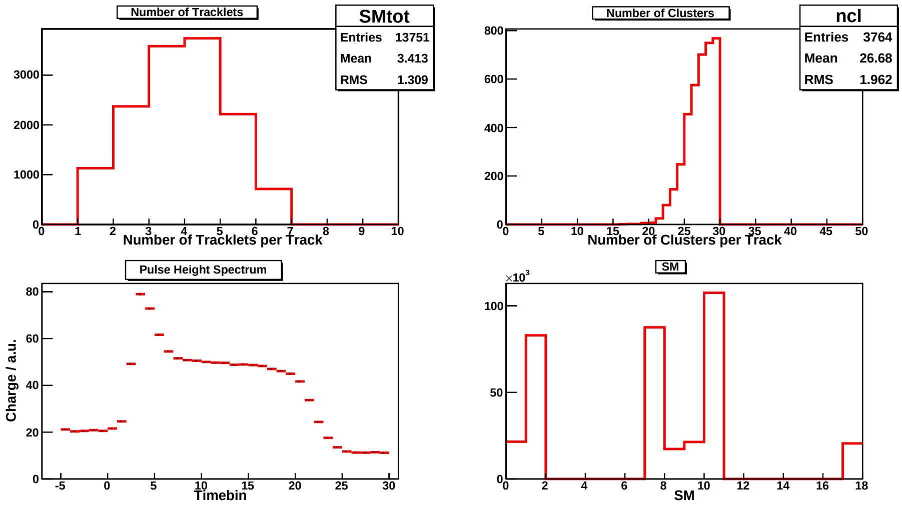

Figure 5.45: Monitor Plot Run 85660

5.3.7 Run 88546

Run 88546 took place on October 3rd, 2009 without magnetic field. The duration of this run was 3336 s.

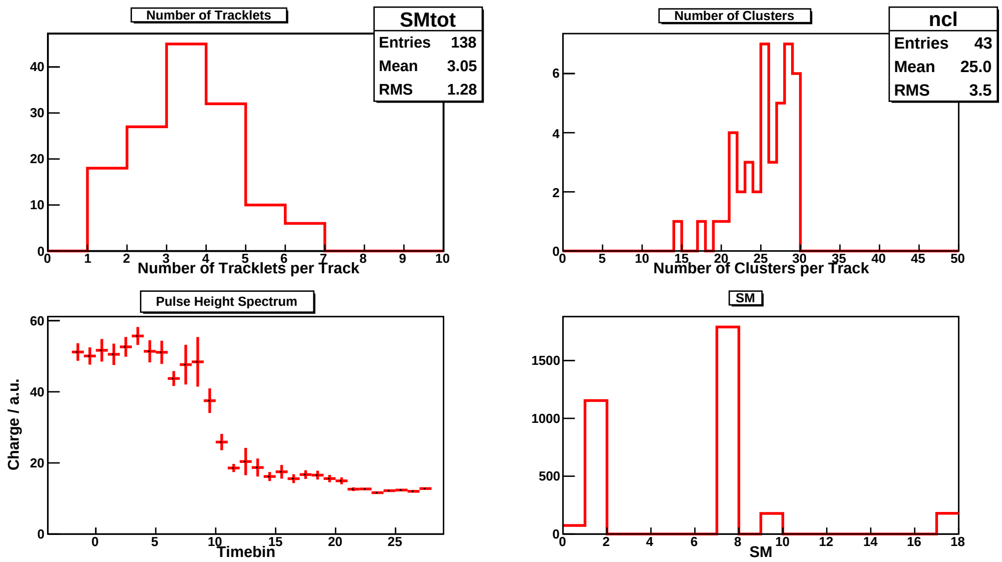

Figure 5.46: Monitor Plot Run 88546

5.3.8 Run 88884

Run 88884 took place on October 6th, 2009 without magnetic field. The duration of this run was 3230 s.

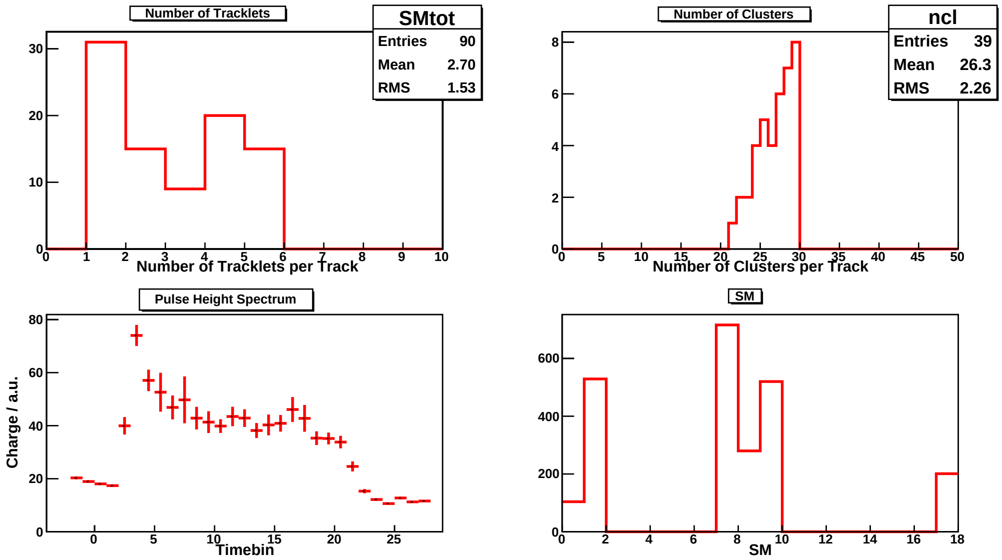

Figure 5.47: Monitor Plot Run 88884

5.3.9 Run 89069

Run 89069 took place on October 7th, 2009 without magnetic field. The duration of this run was 10111 s.

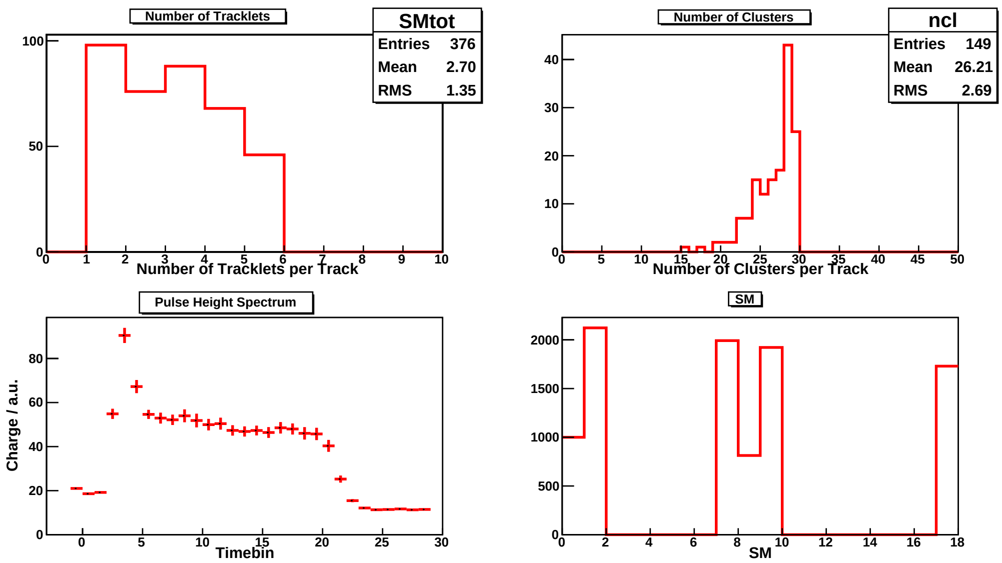

Figure 5.48: Monitor Plot Run 89069

5.3.10 Run 89097

Run 89097 took place on October 8th, 2009 without magnetic field. The duration of this run was 8346 s.

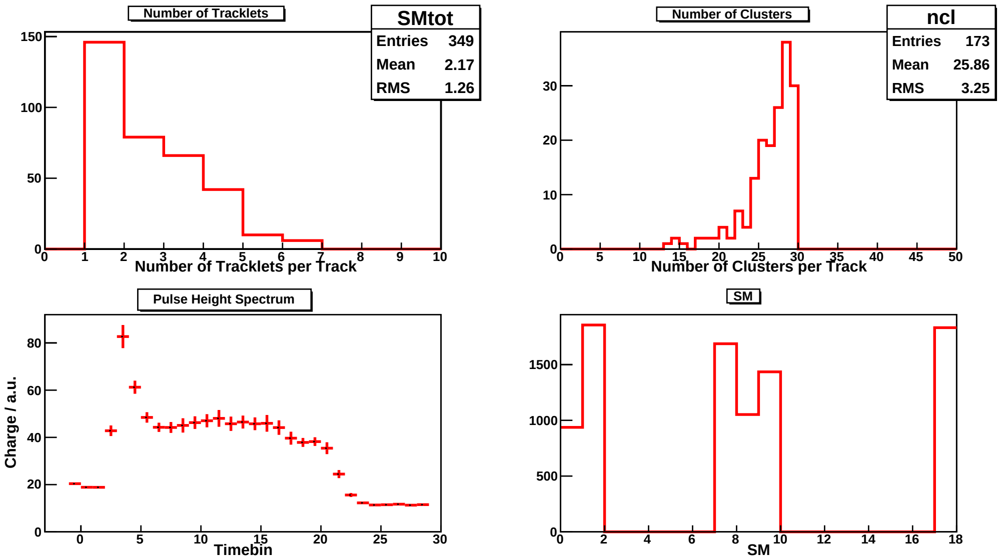

Figure 5.49: Monitor Plot Run 89097

5.3.11 Run 95741

Run 95741 took place on November 4th, 2009 with a magnetic field + 0,2 T. The duration of this run was 4665 s.

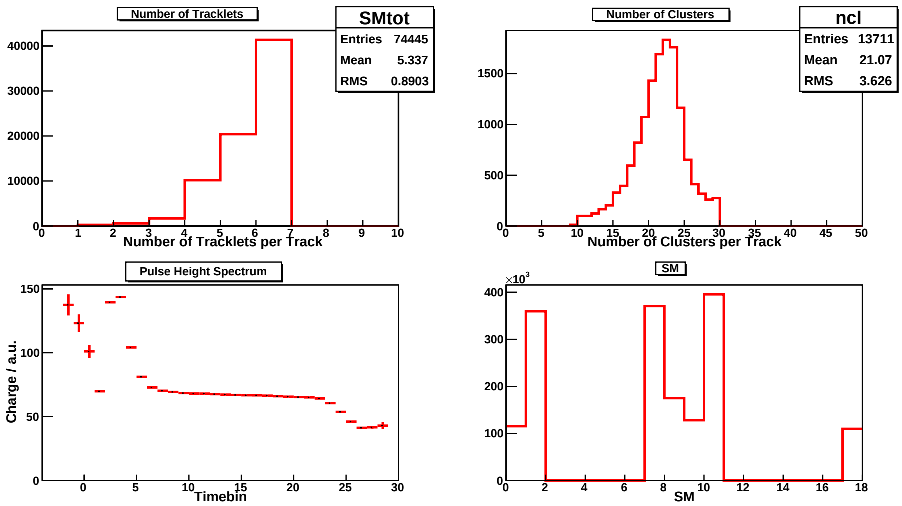

Figure 5.50: Monitor Plot Run 95741

5.3.12 Run 96287

Run 96287 took place on November 6th, 2009 with a magnetic field of + 0,2 T. The duration of this run was 26346 s. This run has the best statistic with over 8000000 cluster entries and 67808 tracks.

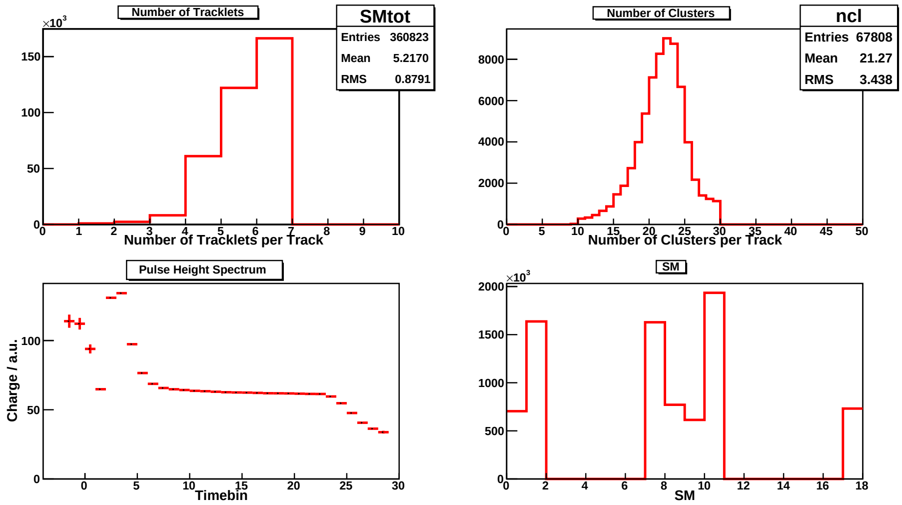

Figure 5.51: Monitor Plot Run 96287

5.3.13 Run 97873

Run 97873 took place on November 12th, 2009 with a magnetic field of + 0,2 T. The duration of this run was 12441 s.

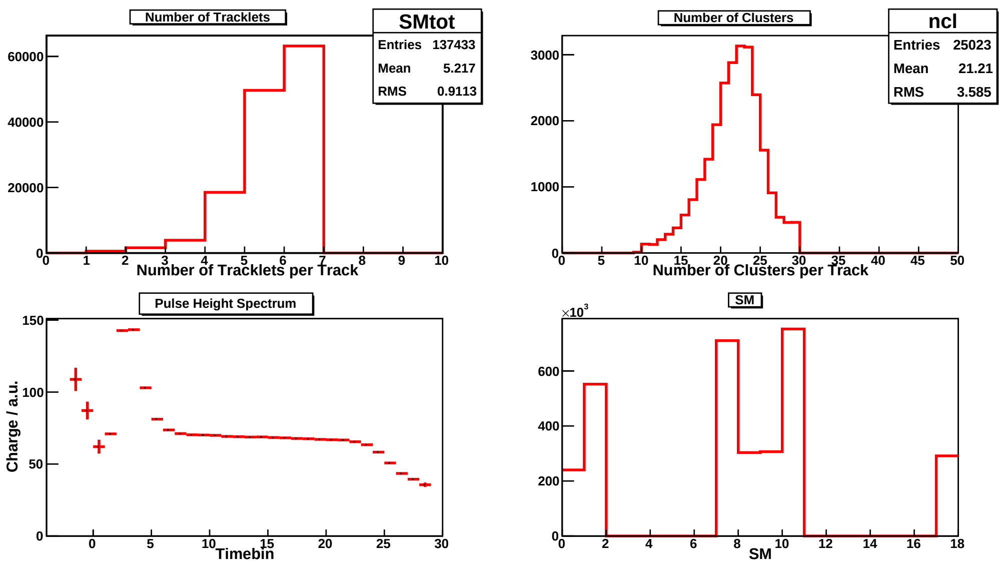

Figure 5.52: Monitor Plot Run 97873

5.3.14 Run 98371

Run 98371 took place on November 13th, 2009 with a magnetic field of + 0,2 T. The duration of this run was 2031 s.

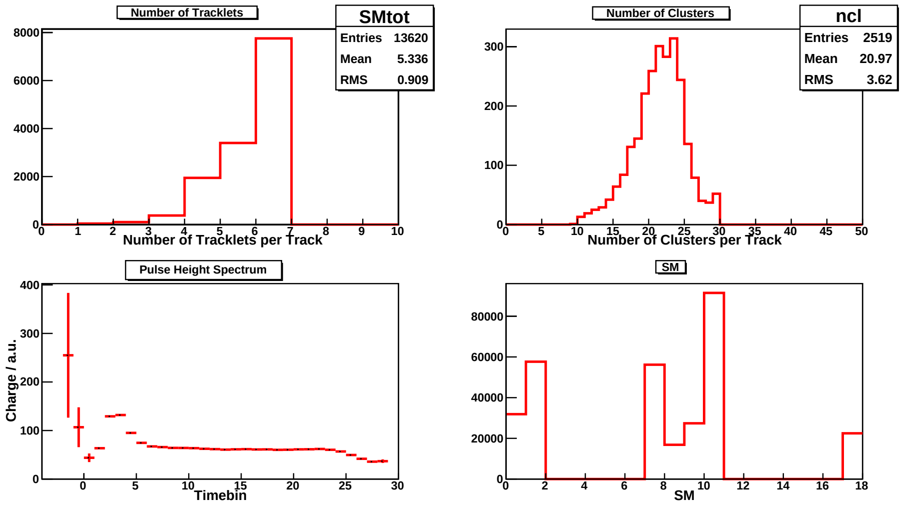

Figure 5.53: Monitor Plot Run 98371

5.3.15 Run 99031

Run 99031 took place on November 15th, 2009 with a magnetic field of + 0,2 T. The duration of this run was 9394 s. In this run chamber S4L2 of sector 7 and chamber S3L5 of sector 17 were switched off, chamber S3L0 of sector 10 was in standby mode.

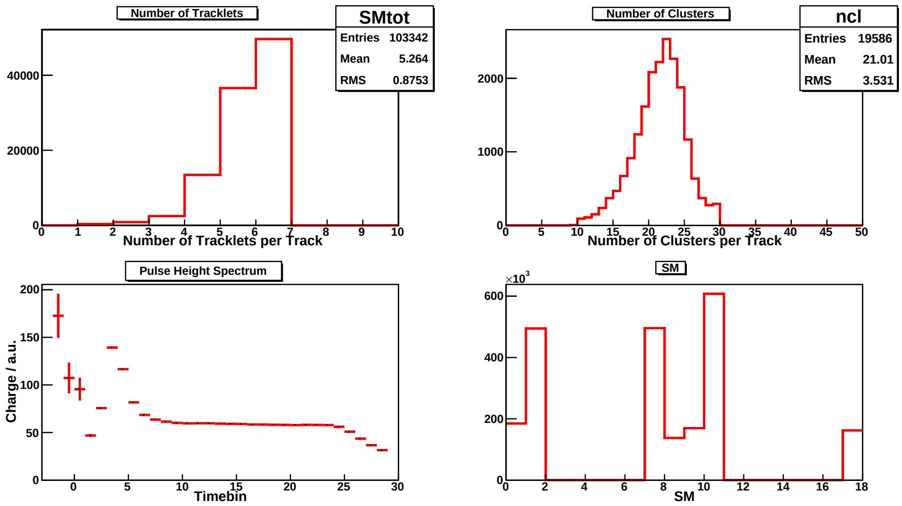

Figure 5.54: Monitor Plot Run 99031

5.3.16 Overview clusters, tracklets and tracks Run period LHC09c

In the following table the number of clusters, the number of tracklets and the number of tracks are summarized for each run of run period LHC09c.

Run Number	Number of Clusters	Number of Tracklets	Number of Tracks
81043	440406	30019	14466
81083	652	45	20
81116	88834	6108	2839
85618	975633	37304	10022
85625	243	9	5
85657	10200	381	179
85658	12564	473	245
85660	358697	13751	3764
88376	605	24	10
88546	3375	138	43
88884	2350	90	39
89069	9580	376	149
89097	8797	349	173
95741	1654092	74445	13711
96287	8020831	360823	67808
97873	3156371	137433	25023
98371	303901	13620	2519
99031	2252290	103342	19586

Table 5.2: Overview of the number of clusters, number of tracklets and number of tracks for the cosmic run period LHC09c, which lasted from August 2009 until November 2009.

Chapter 6

Conclusion and outlook

6.1 Performance Conclusions

As it was showed in the previous chapter the performance of the TRD during cosmic data taking fits quite good with the expected trends for the average pulse height spectra. But there was clearly an unexpected behavior for all runs reconstructed and analyzed with the older AliRoot version. Starting from run 85618 the typical trend with a maximum at low timebins and a plateau which drops around timebin 25, which belongs to the longest drift times in the drift volume and therefore marks the edge of the radiator, is reproduced in every following run, except for low statistic perturbations. Some runs show contributions in low timebins which belong to drift times smaller then 0,5 μs. The origin of these perturbations is not quite understood yet.
The distribution of number of clusters per tracklet shows in principle three different forms. For all the runs of run period LHC08d and the first runs of run period LHC09c, which are all produced with the older software, a very broad distribution with a center around 15 clusters was observed. The Ar runs with the new reconstruction software show a distribution which looks like one half of a Gaussian as if it was cut in the middle with respect to the mean. The Xe runs finally show a simple Gaussian distribution for the number of clusters per tracklet. This is due to the fact that for these runs a newer revision of AliRoot v4-17 was used. The shift of the mean when comparing the Ar runs and the Xe runs can be explained alike.
The number of tracklets per track is determined by the distribution of clusters per tracklet. In the cases when the clusters have a broad distribution the number of tracklets per track has a rather broad distribution as well. This is true for the plots created before run 85618. Afterwards the tracklet distribution shows an irregular behavior according to statistics and shows peaks at 1 tracklet or broad distributions. In contrary the Xe runs show a distribution with a clear peak at 5 or 6 tracklets.
The total number of entries in the single sectors show that sectors with a smaller zenith angle with respect to the vertical are favored over those sectors with zenith angles near 90° because of the higher muon threshold caused by the higher ma-

terial budget. One could expect that for the yet not installed sectors (2, 6, 11 and 15) the number of entries in cosmic run events will show a maximum in these sectors, because they will be at the preferred zenith position where the muon energy threshold shows a minimum due to the supply shaft crossing. But one has to consider the effect of the L3 magnetic field as well for the determination of the maximum number of entries.

On the other hand for the pp collisions a uniform distribution in all sectors is expected, because the charged particles should be distributed isotropic. For a comparison on can see the results from one of the very first pp collision runs (104321) in figure 6.1, which took place on December, 8th 2009. The average pulse height is shown similar produced like the ones for the cosmic runs. One can see the uniform distribution in the number of entries as expected with one exception. In sector 10 one can see that the detectors of stack 3 still contribute with a higher number, in this case approximately 8% more than in the other detectors.

The single detector performance showed that some detectors are either switched off during most of the runs (e.g. detector 236), or had problems during the single run, producing only a small amount of data. When compared to the pp run, most of these detectors show these problems again. In sector 0 detectors 15 and 19 still have a low number of entries. In this sector a new low entry detector occurred in this single run (detector 12). Sector 1 shows the same low entry detectors as described for the Xe cosmic runs (detectors 30, 32 and 52). The same is true for sector 7 in which two detectors deliver a small amount of data (detector 228 and detector 232) and detector 236 has no entries at all. Detectors 260 and 265 of sector 8 do also contain a small amount of data as it was seen before. On the contrary in sector 9 all detectors except detector 273, which has low entries, look good. In sector 10 all detectors contribute without any problems, although stack 3 still has a higher number of entries compared to the other detectors of the sector. Finally in sector 17 detector 533 has no entries at all, detector 539 has a small amount of entries, which was seen before, and detector 532, which was not conspicuous before, has a small number of entries.

As a conclusion one can say that the single detector performance especially for the xenon runs 95741, 96287, 97873, 98371 and 99031 predicts the performance of the TRD during pp collisions very good. The still problematic detectors have to be checked with respect to their test results from the electronic integration and from the construction of the chambers to bring them back into operation mode.

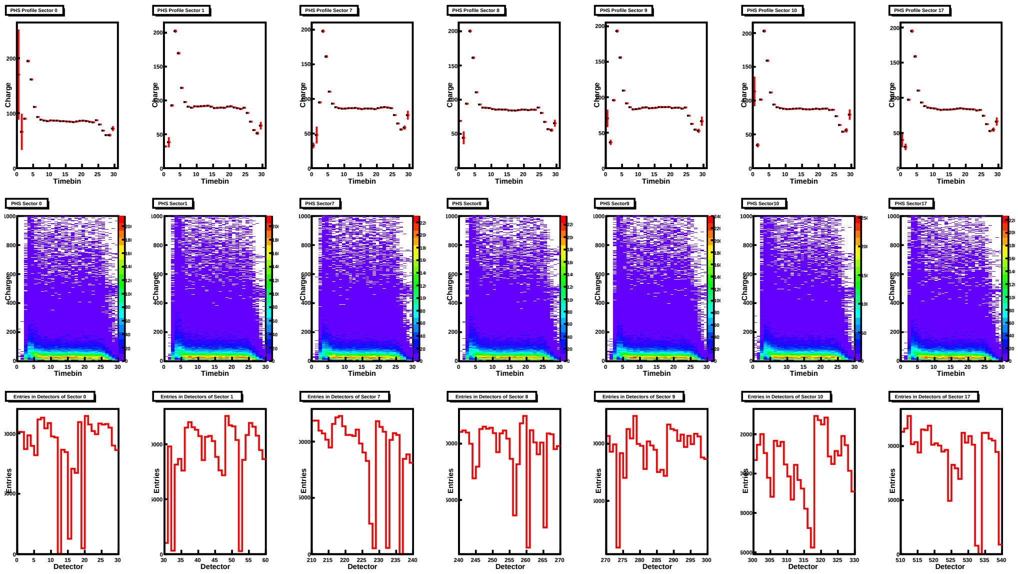

Figure 6.1: Average pulse height spectrum for the pp run 104321. One can see the uniform distribution of the total number of entries in every sector. The slightly higher number of stack 3 in sector 10 was found in the cosmic runs as well.

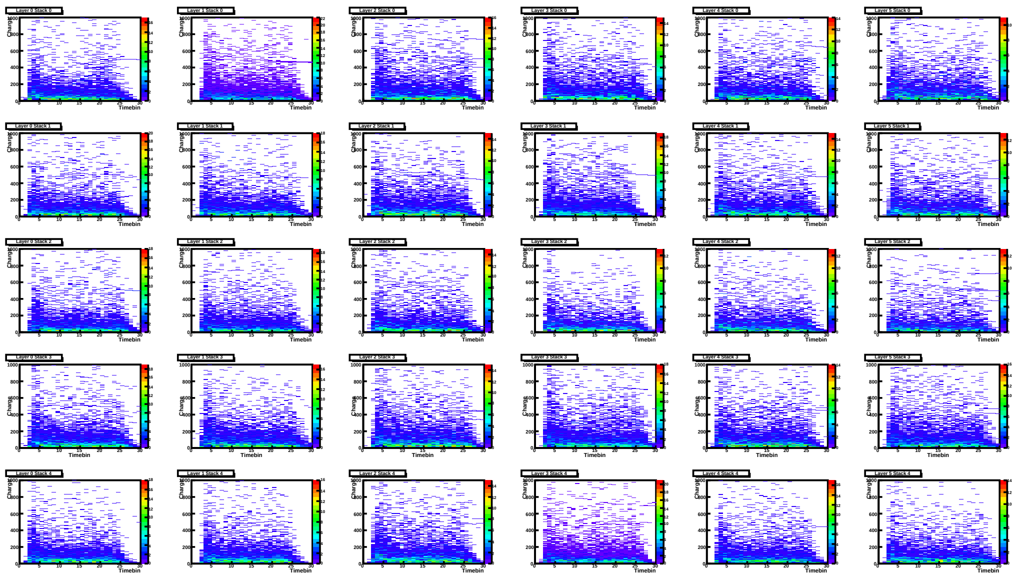

Figure 6.2: Overview of the single detectors of sector 10 during one of the first pp collision runs (104321). This plot is shown as an example for comparison with the single detector plots shown in Chapter 5.

6.2 Outlook

What needs to be done for the future? First of all the completion of the eleven remaining supermodules and their installation into ALICE must be done from the hardware side. The installation can take place during the maintenance of the LHC which will be at the beginning of 2011. The performance of all those sectors will be tested with cosmics prior to their final install. This will be done with every single supermodule during its assembly in Münster and after installation with the available sectors in upcoming cosmic runs. Meanwhile the performance of the yet installed sectors with pp-collision data has to be checked and compared with the performance with cosmics. This will be done continuously with the new sectors, too. For lead-lead collisions the performance tests can be applied as well.

Appendix A

Appendix

A.1 ROOT Analysis Code

The plotting macro PlotPHSsectors.C which was used to analyse the cosmic runs was developed parallel to the analysis of the cosmic runs at GSI. It is based on a simple C++ code and can be optimized introducing more elegant solutions looping over all detectors. This could help reducing the computing time, which exceeds one hour for the high statistic run 96287 at the moment. The macro can be found and altered on any GSI machine in the directory u/mfreuden/aliroot/cosmics/.

A.2 Table of Runs

All analyzed runs are summarized in the following tables. The run number, the duration of the run in seconds, which can be found in the electronic logbook, and the number of tracks that were derived from the analysis are found in these tables.

Cosmic Run Period LHC08d			
Run number	Duration in s	Number of Tracks	Comments
60283	36952	660	
60419	6305	258	
60517	15	59	
60545	5955	796	
60668	2083	84	
60813	6299	620	
60920	9601	1662	
60977	2693	245	
60984	12451	1493	
60993	2946	79	
61048	12050	1280	
61120	18590	2669	
61694	2872	201	Sec08_S3L2 off
61796	4507	566	
61858	3900	231	
61869	1772	182	
61872	2879	82	
62006	9713	611	with magnetic field +0,5 T
62029	10409	514	with magnetic field +0,5 T
62065	4431	34	
62084	16914	1156	with magnetic field -0,5 T
62102	19508	752	with magnetic field -0,5 T
62414	9820	2270	
62434	5789	1012	
62439	9304	3651	
62512	8316	2605	
62517	4437	998	
62521	12899	1661	

Table A.1: Conclusion of the runs from cosmic run period LHC08d. The duration of the runs is taken from the electronic logbook, the number of tracks is derived from the analysis plots.

Cosmic Run Period LHC09c			
Run Number	Duration in s	Number of Tracks	Comments
81043	28654	1466	Sec07_S4L2 off Sec08_S2L0 high temperature
81116	3858	2839	
85618	20744	10022	Sec07_S4L2, Sec08_S0L4, Sec17_S3L5 off
85625	184	5	Sec07_S4L2, Sec08_S0L4, Sec17_S3L5 off
85657	3662	179	Sec07_S4L2, Sec08_S0L4, Sec17_S3L5 off
85658	5391	245	Sec07_S4L2, Sec08_S0L4, Sec17_S3L5 off
85660	8302	3764	Sec07_S4L2, Sec08_S0L4, Sec17_S3L5 off
88546	3336	43	Sector 10 no data
88884	3230	39	Sector 10 no data
89069	10111	149	Sector 10 no data
89097	8346	173	Sector 10 no data
95741	4665	13711	Xe run, magnetic field 0,2T
96287	26346	67808	Xe run, magnetic field 0,2T
97873	12441	25023	Xe run, magnetic field 0,2T
98371	2031	2519	Xe run, magnetic field 0,2T
99031	9394	19586	Xe run, magnetic field 0,2T

Table A.2: Conclusion of the runs from cosmic run period LHC09c. The duration of the runs is taken from the electronic logbook, the number of tracks is derived from the analysis plots.

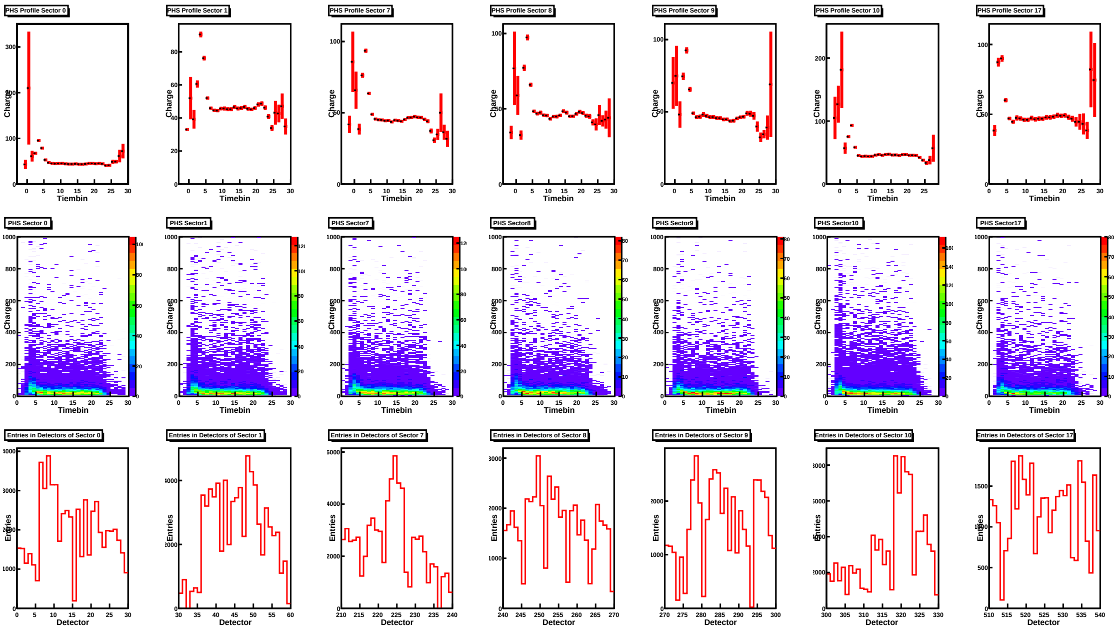

Figure A.1: PHS Profile, PHS and Total Entries per Sector for Run 81043

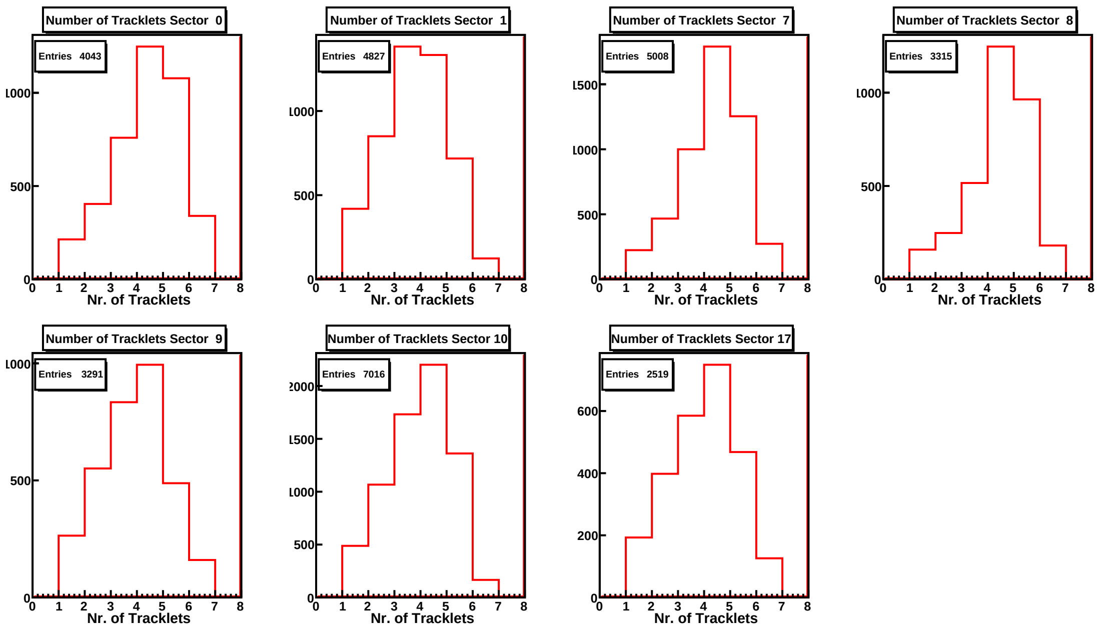

Figure A.2: Tracklets per Track Run 81043

A.3 Single Sector Performance

In the following plots one can see the single sector performance for the runs of runperiod LHC09c.

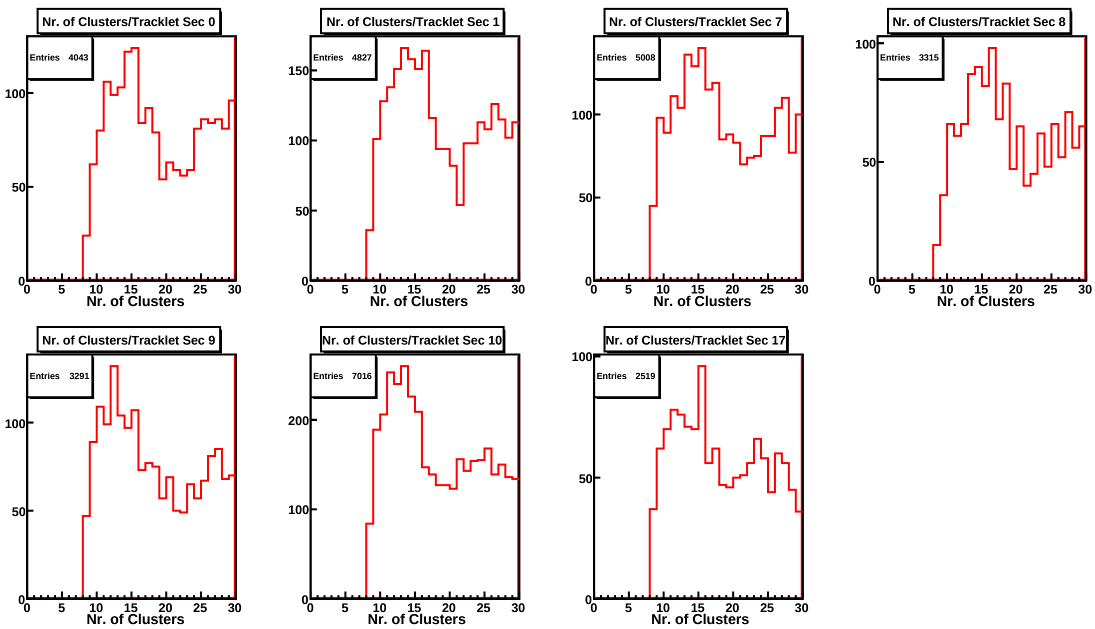

Figure A.3: Clusters per Track Run 81043

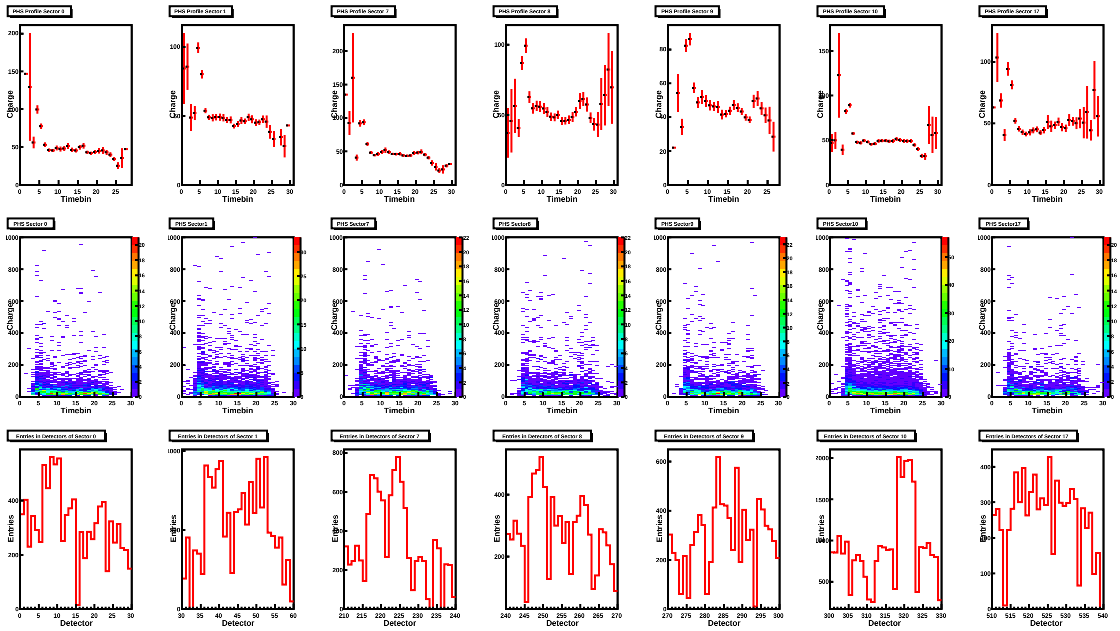

Figure A.4: PHS Profile, PHS and Total Entries per Sector for Run 81116

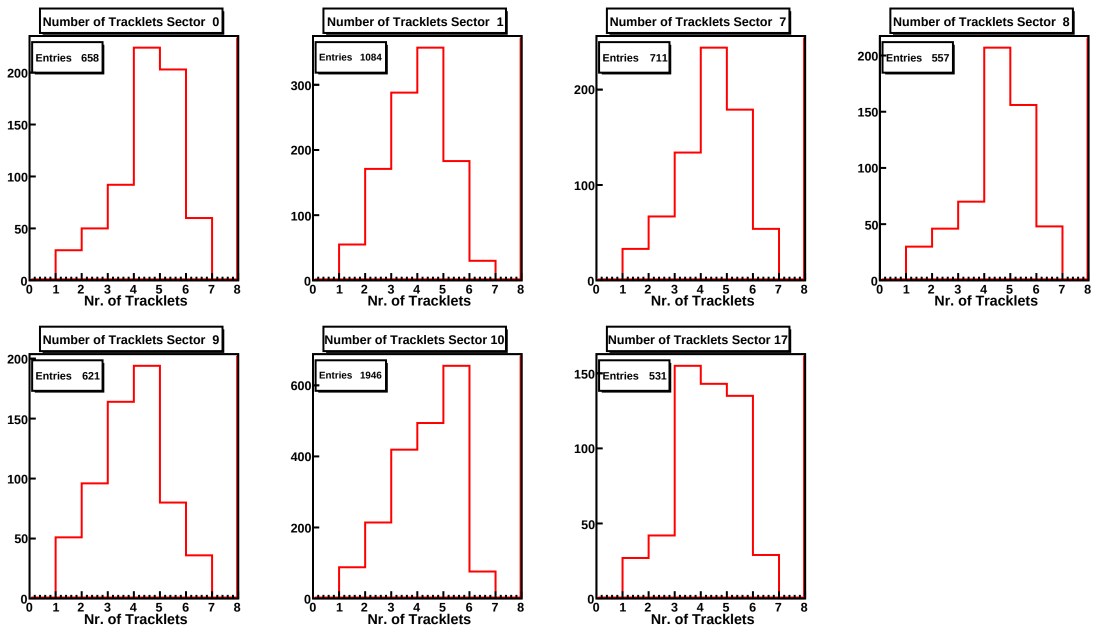

Figure A.5: Tracklets per Track Run 81116

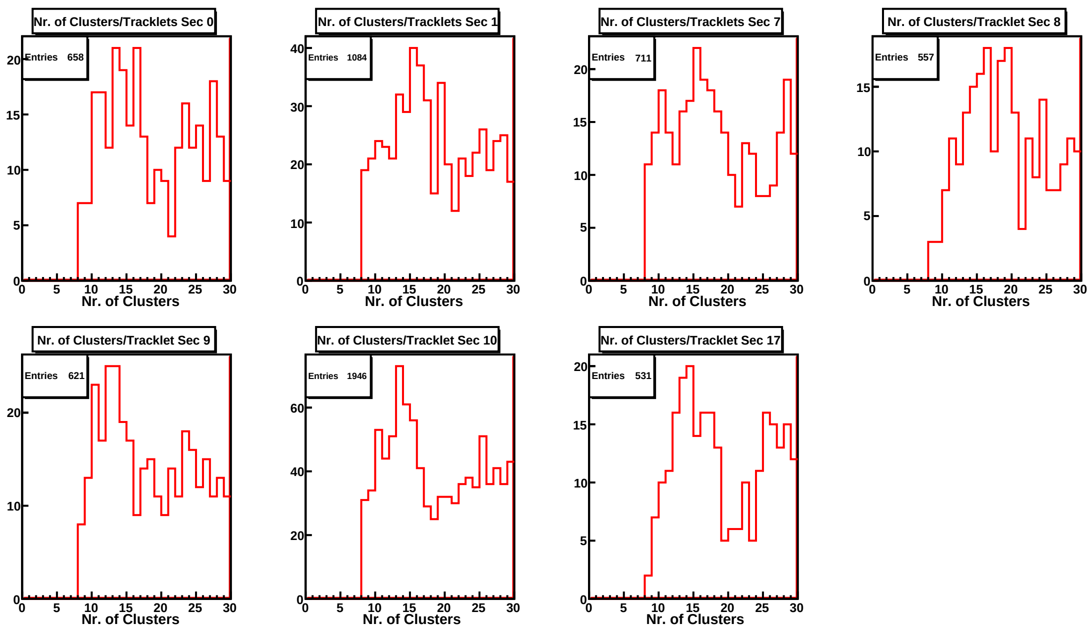

Figure A.6: Clusters per Track Run 81116

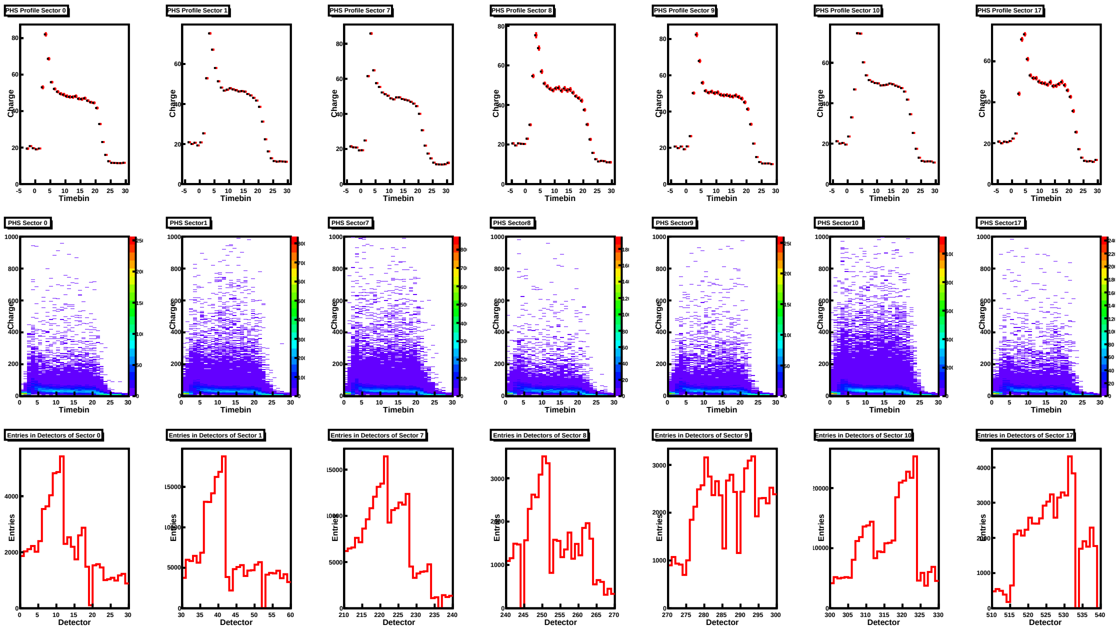

Figure A.7: PHS Profile, PHS and Total Entries per Sector for Run 85618

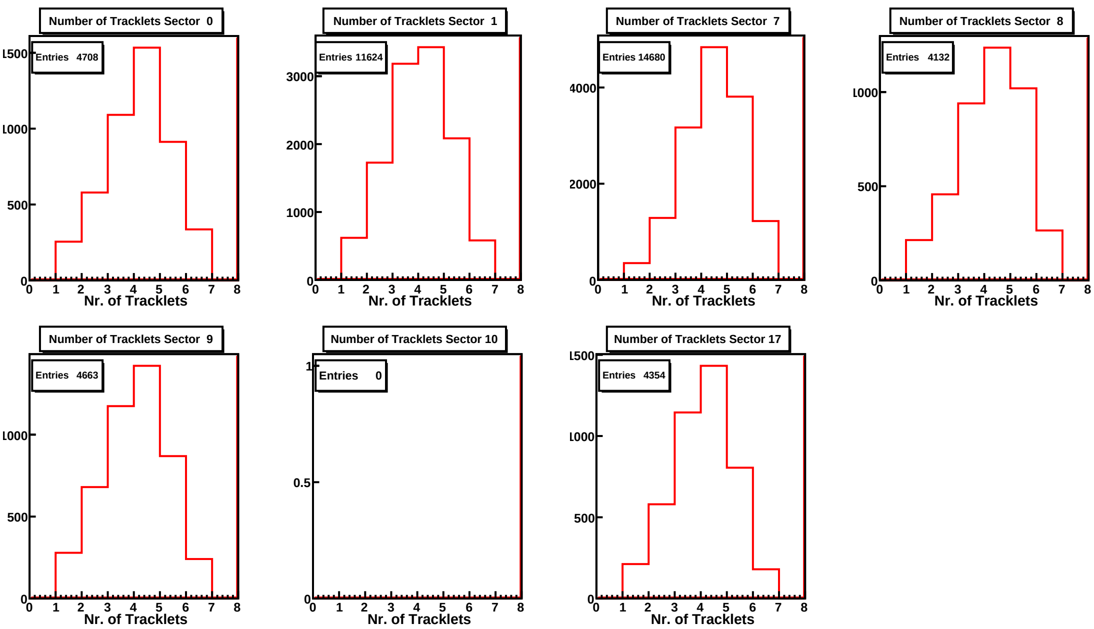

Figure A.8: Tracklets per Track Run 85618

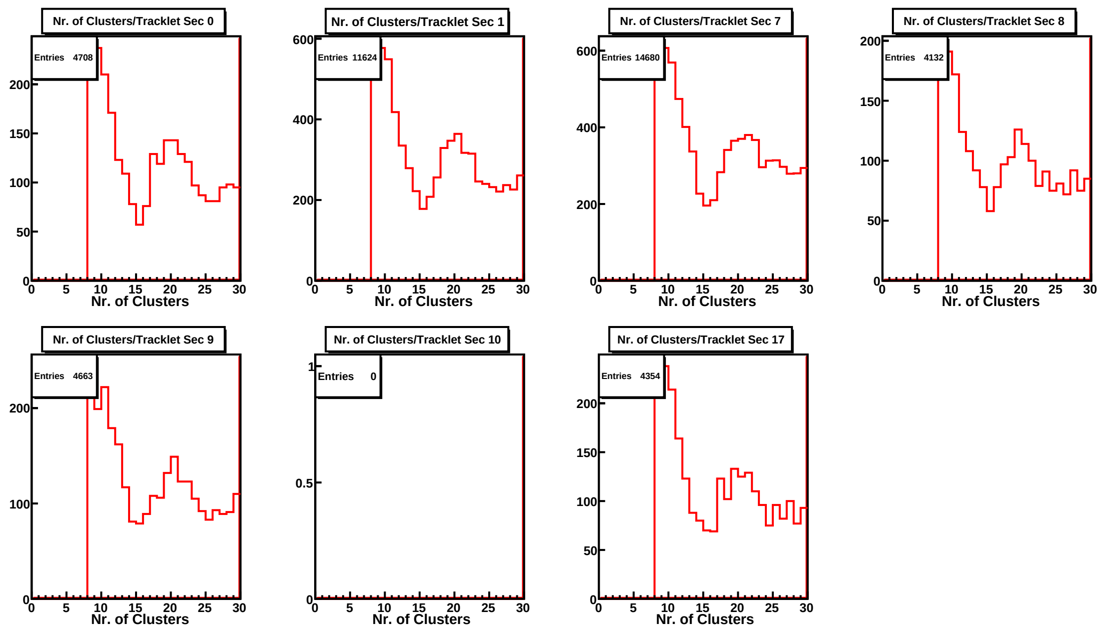

Figure A.9: Clusters per Track Run 85618

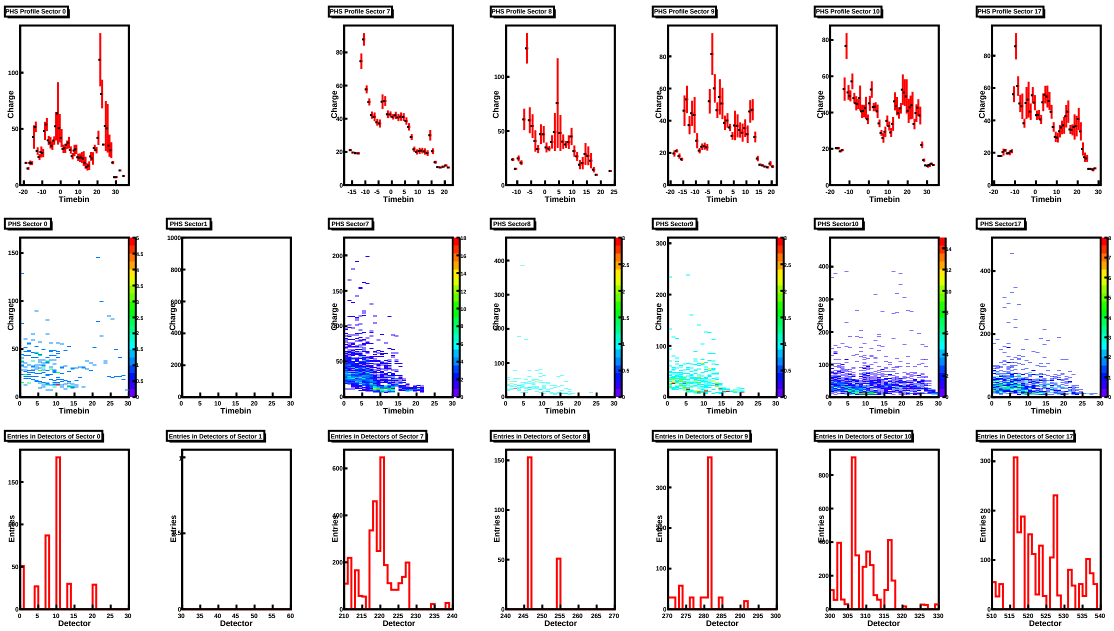

Figure A.10: PHS Profile, PHS and Total Entries per Sector for Run 85657

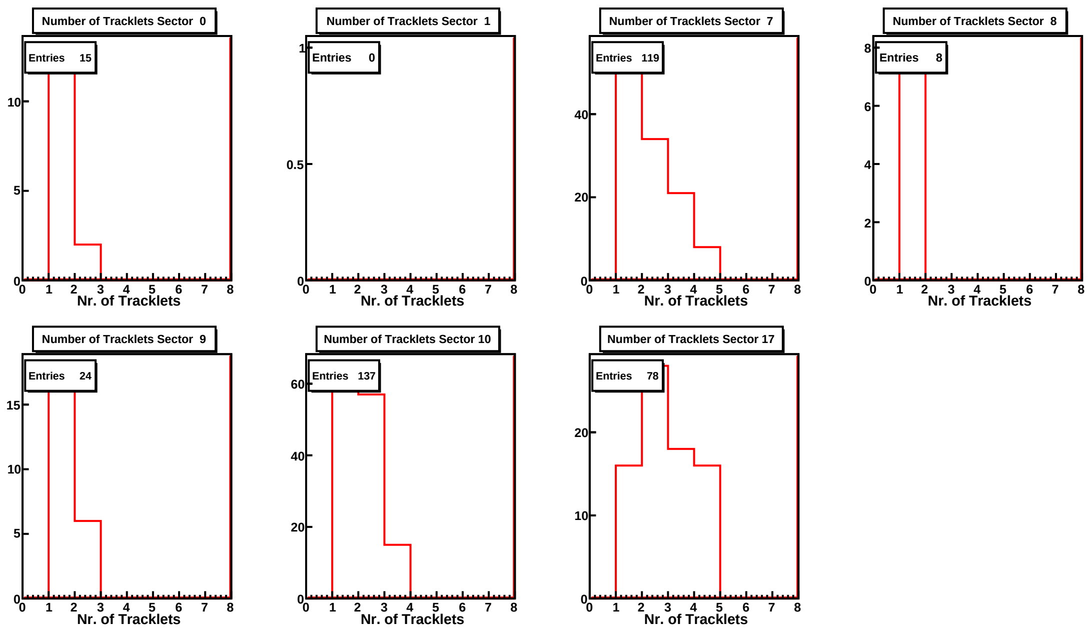

Figure A.11: Tracklets per Track Run 85657

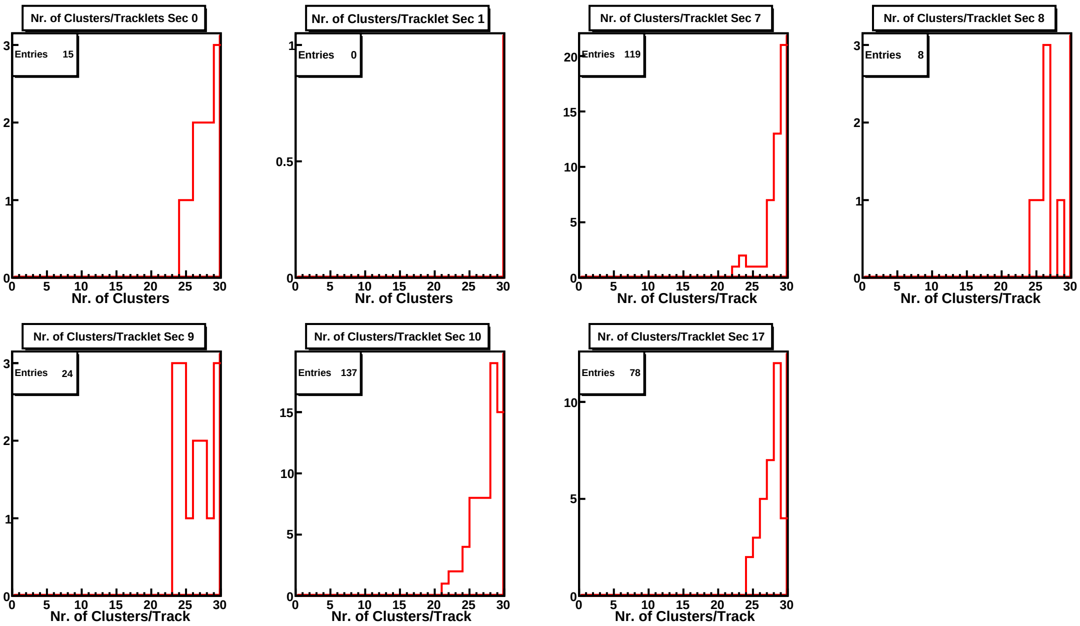

Figure A.12: Clusters per Track Run 85657

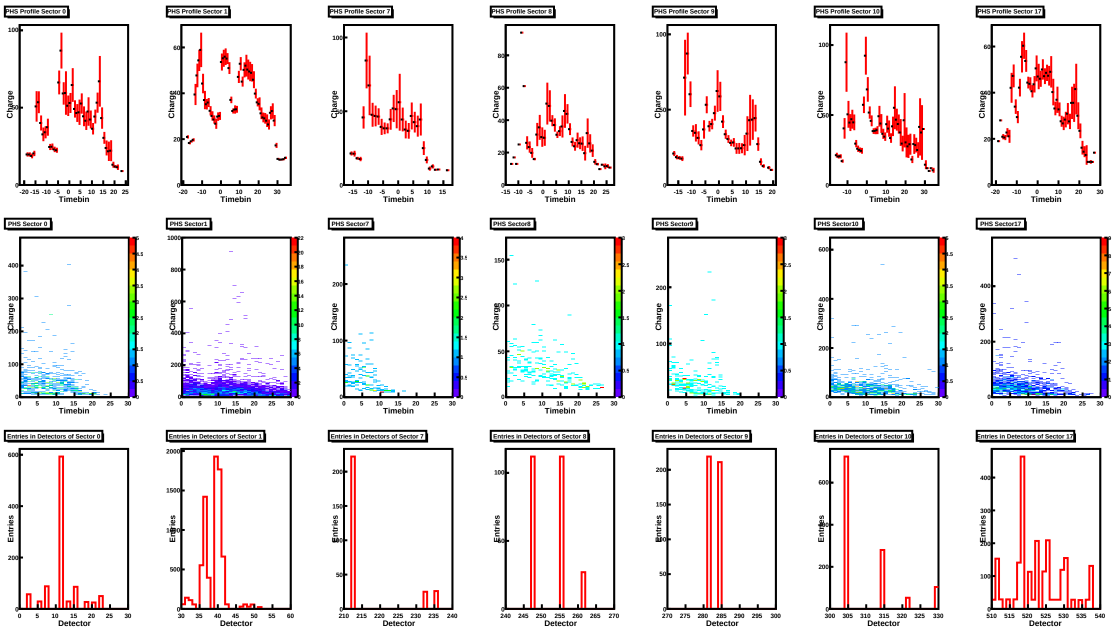

Figure A.13: PHS Profile, PHS and Total Entries per Sector for Run 85658

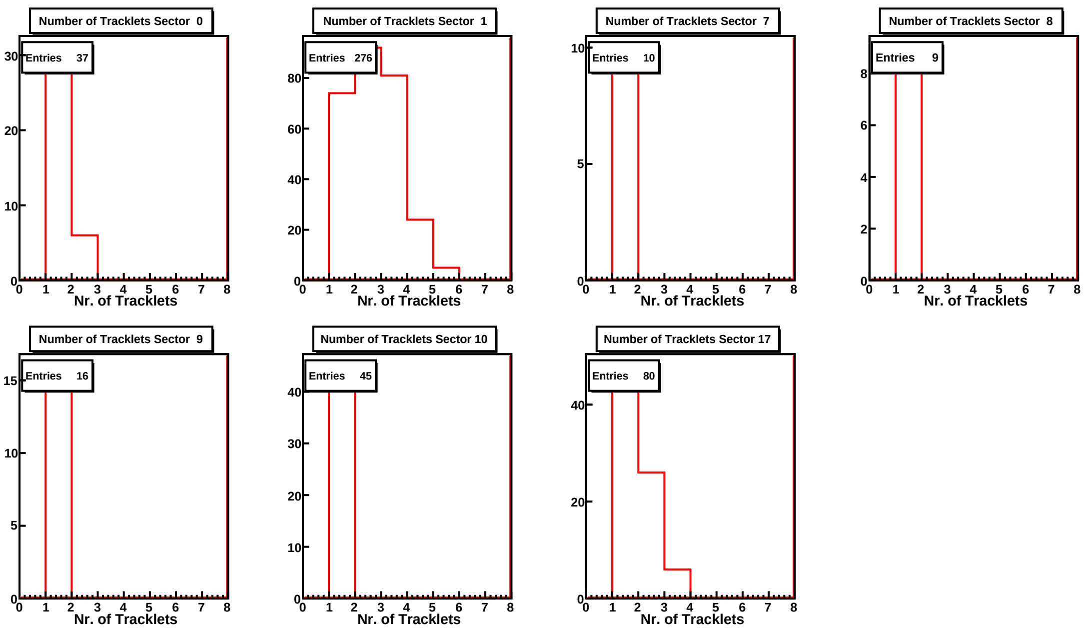

Figure A.14: Tracklets per Track Run 85658

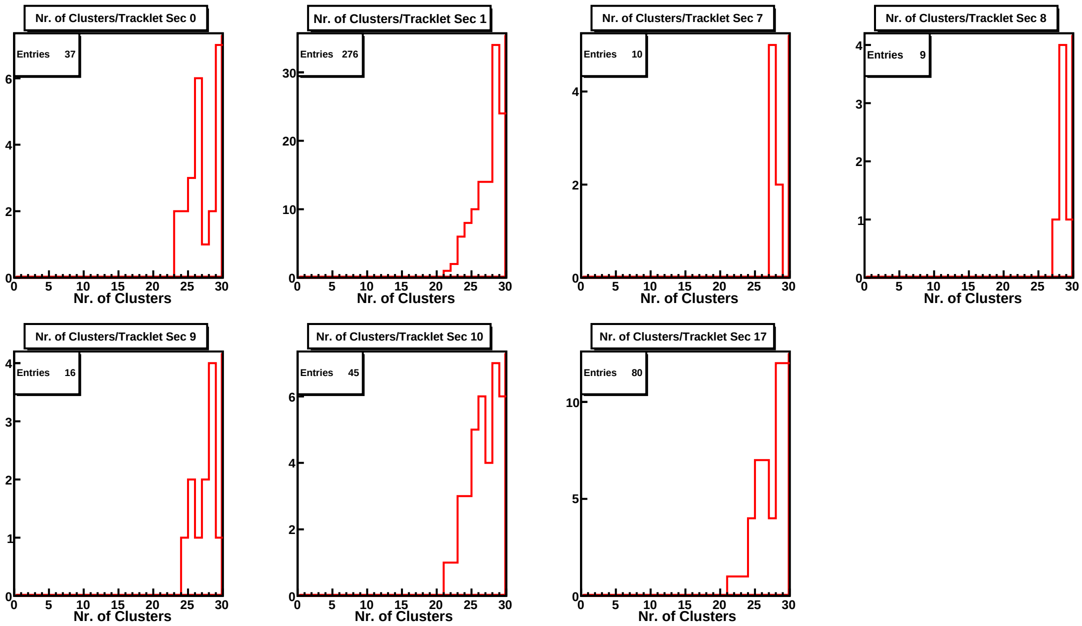

Figure A.15: Clusters per Track Run 85658

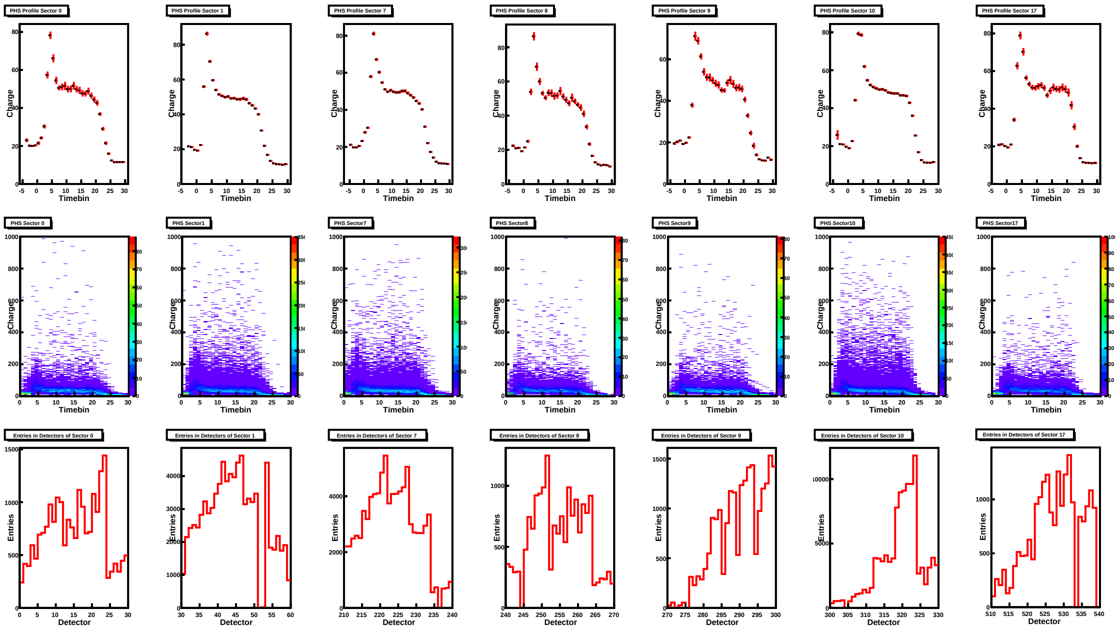

Figure A.16: PHS Profile, PHS and Total Entries per Sector for Run 85660

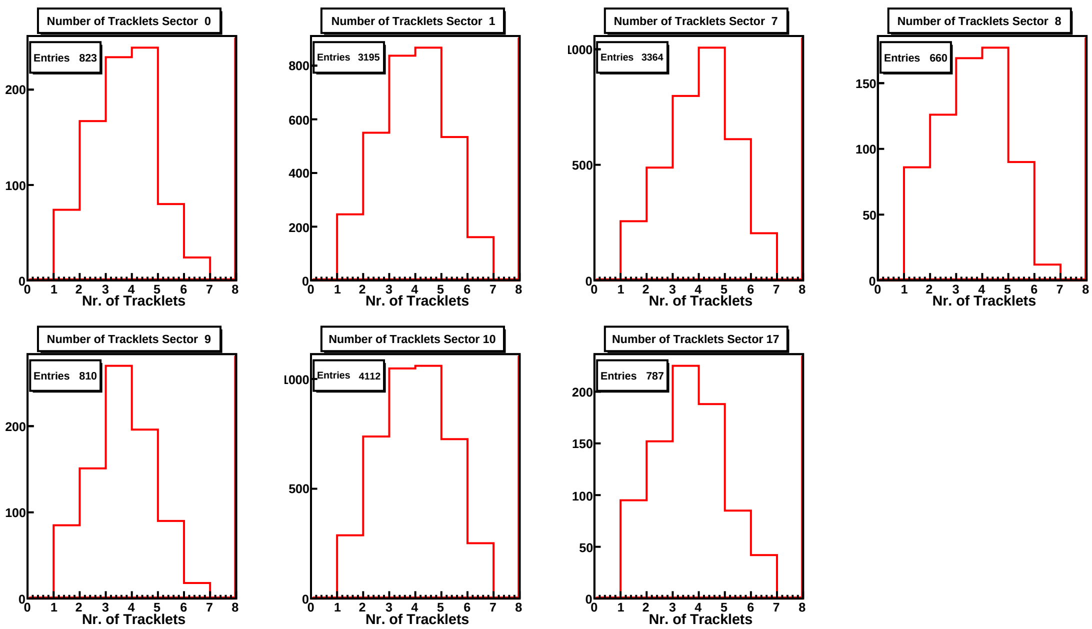

Figure A.17: Tracklets per Track Run 85660

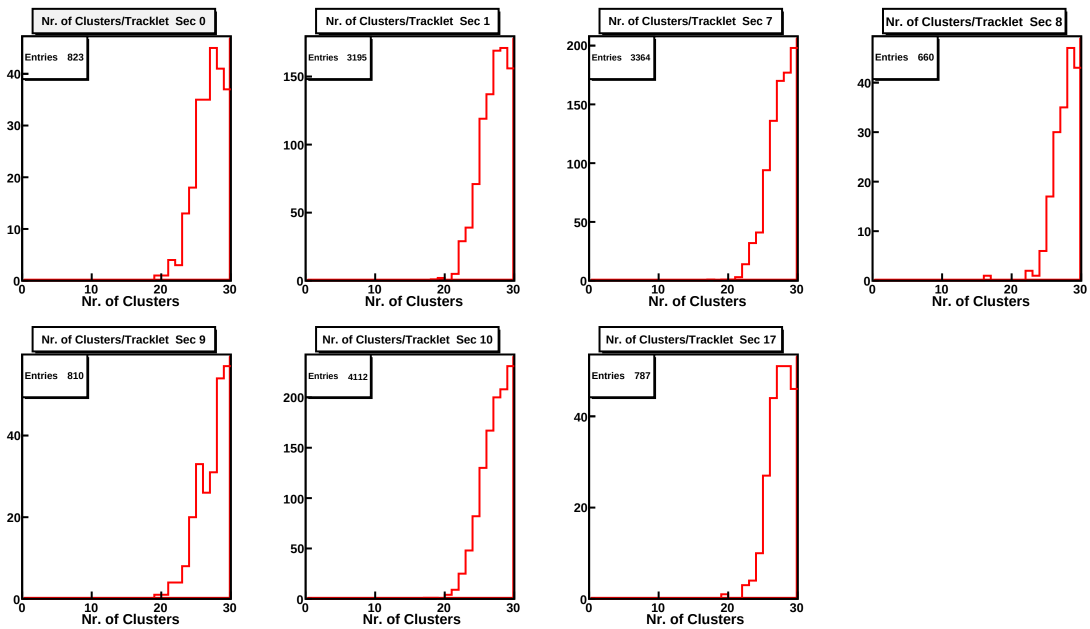

Figure A.18: Clusters per Track Run 85660

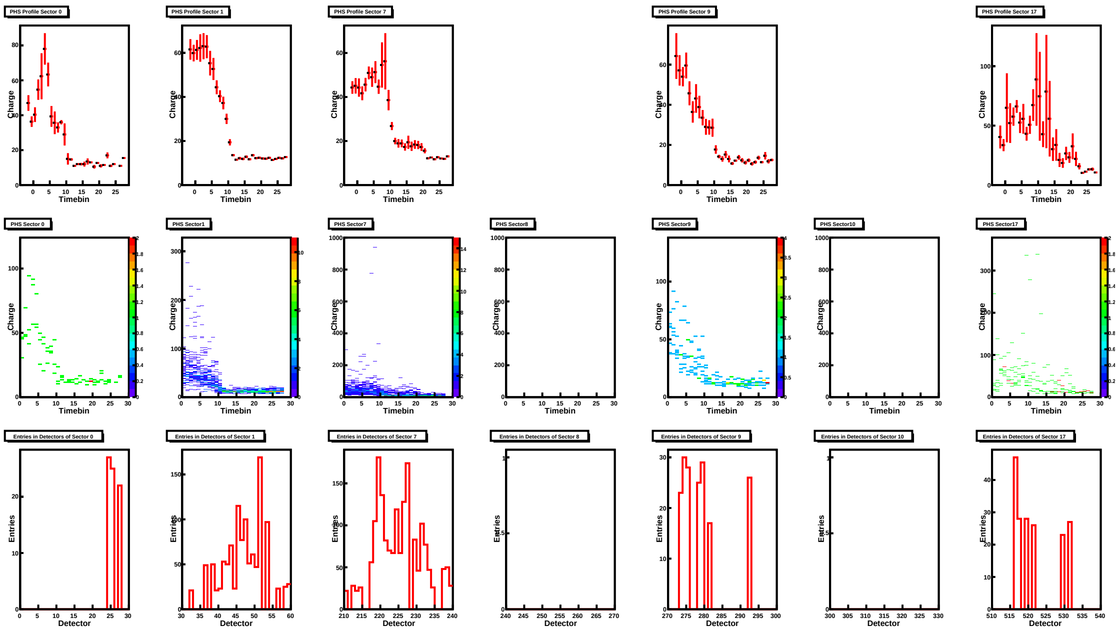

Figure A.19: PHS Profile, PHS and Total Entries per Sector for Run 88546

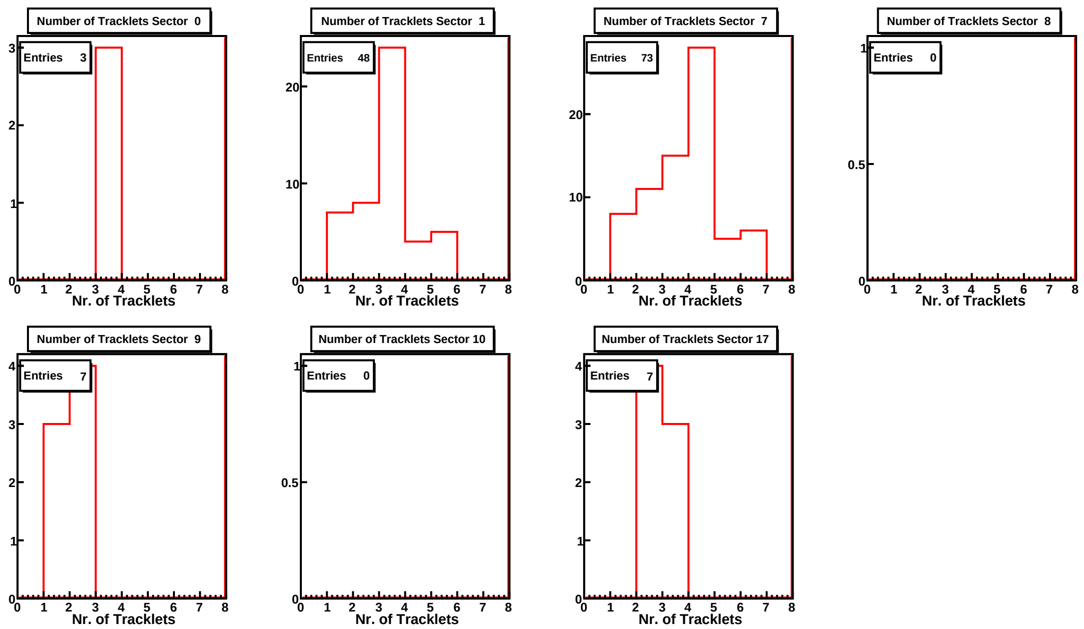

Figure A.20: Tracklets per Track Run 88546

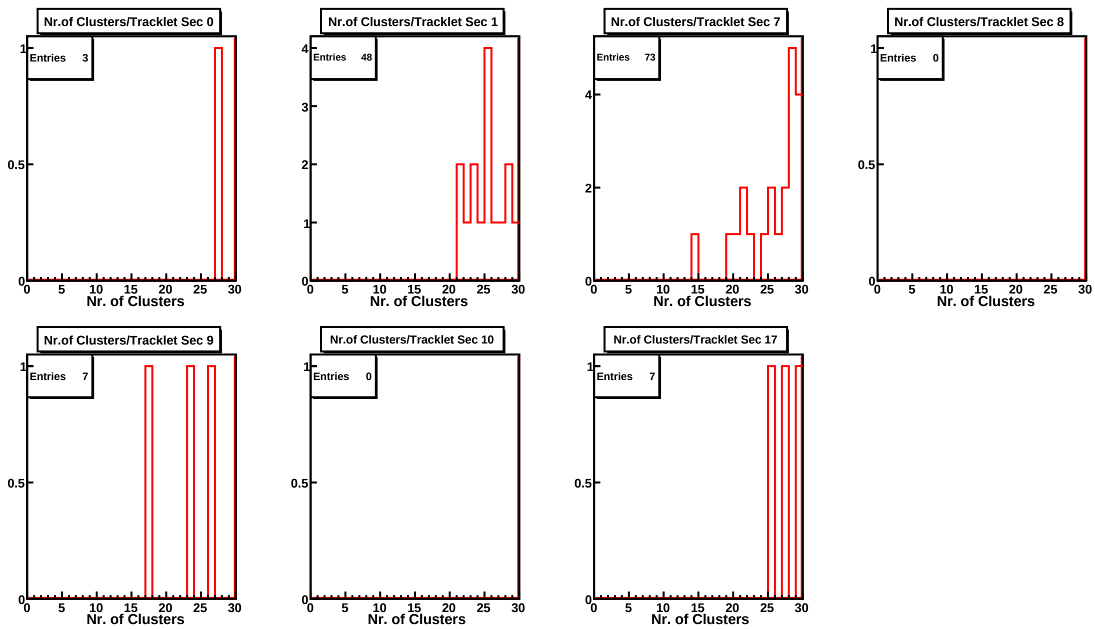

Figure A.21: Clusters per Track Run 88546

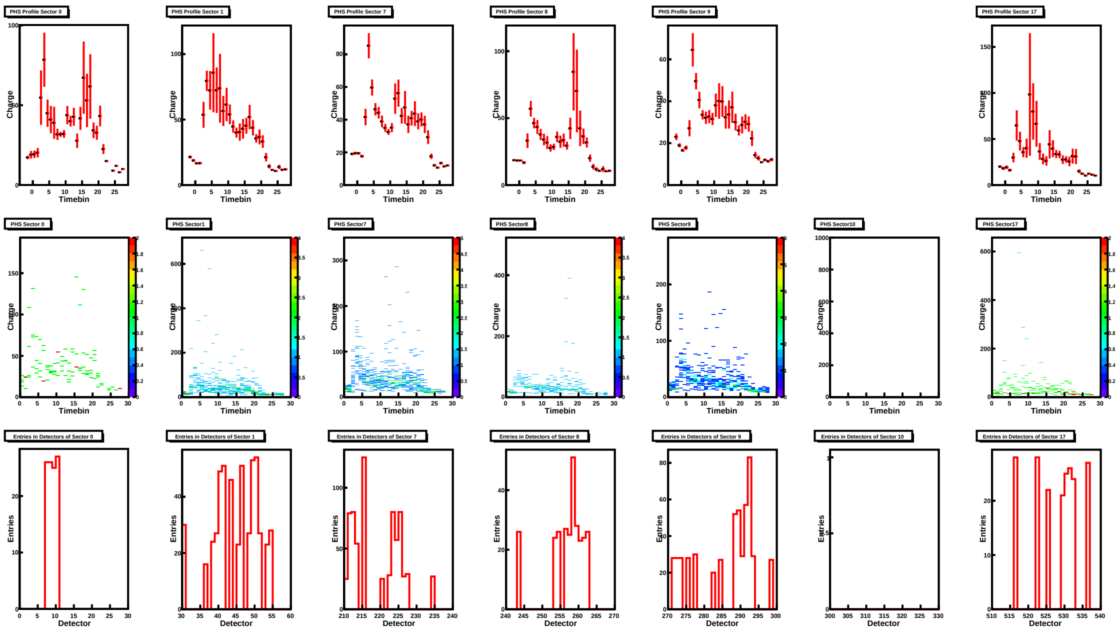

Figure A.22: PHS Profile, PHS and Total Entries per Sector for Run 88884

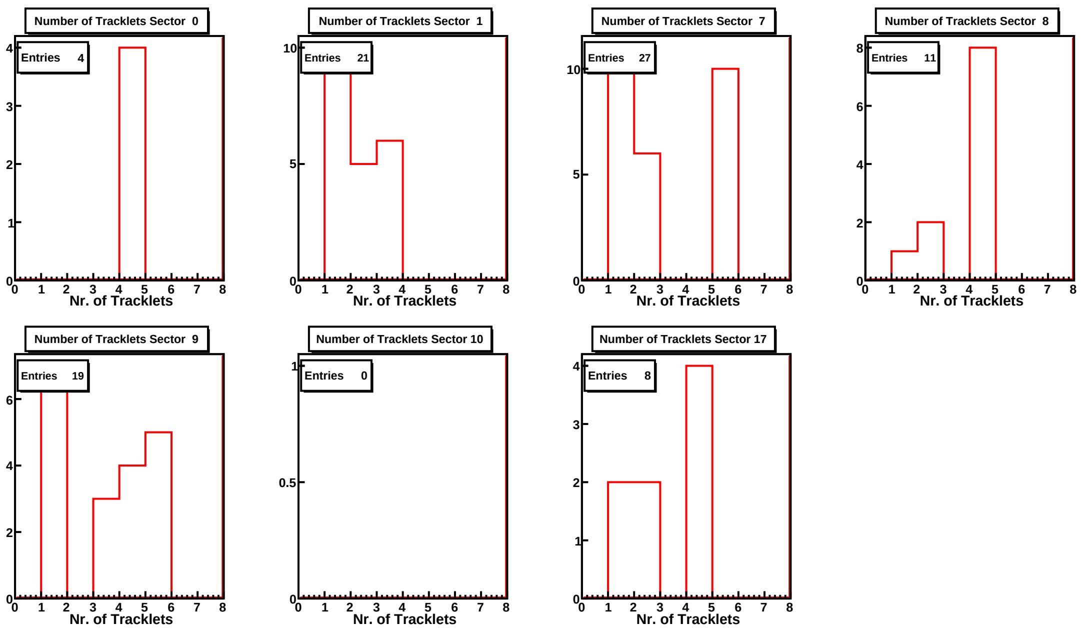

Figure A.23: Tracklets per Track Run 88884

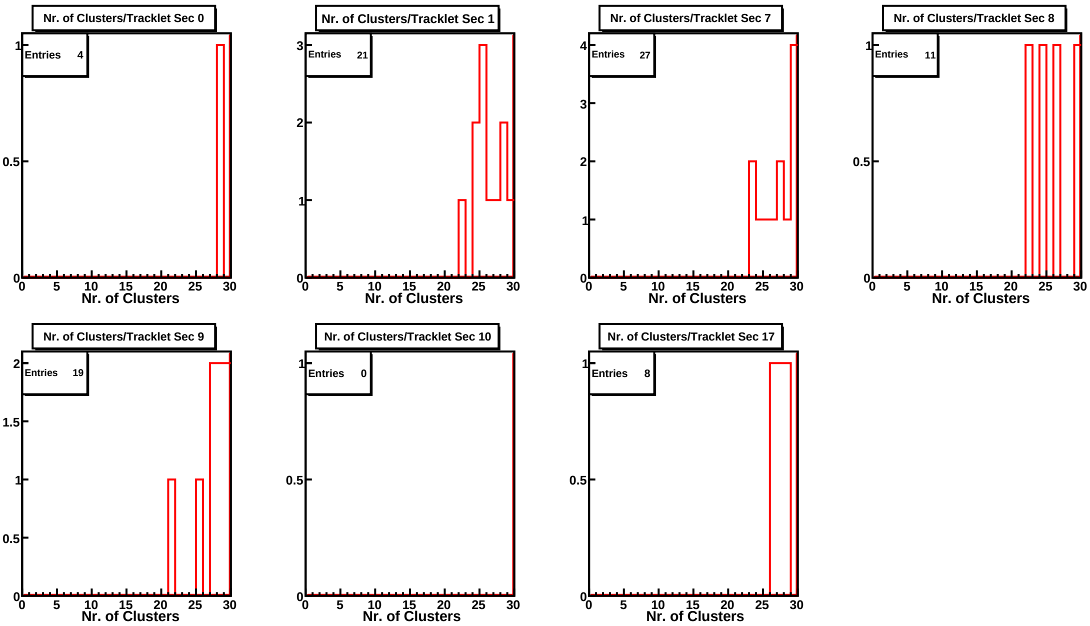

Figure A.24: Clusters per Track Run 88884

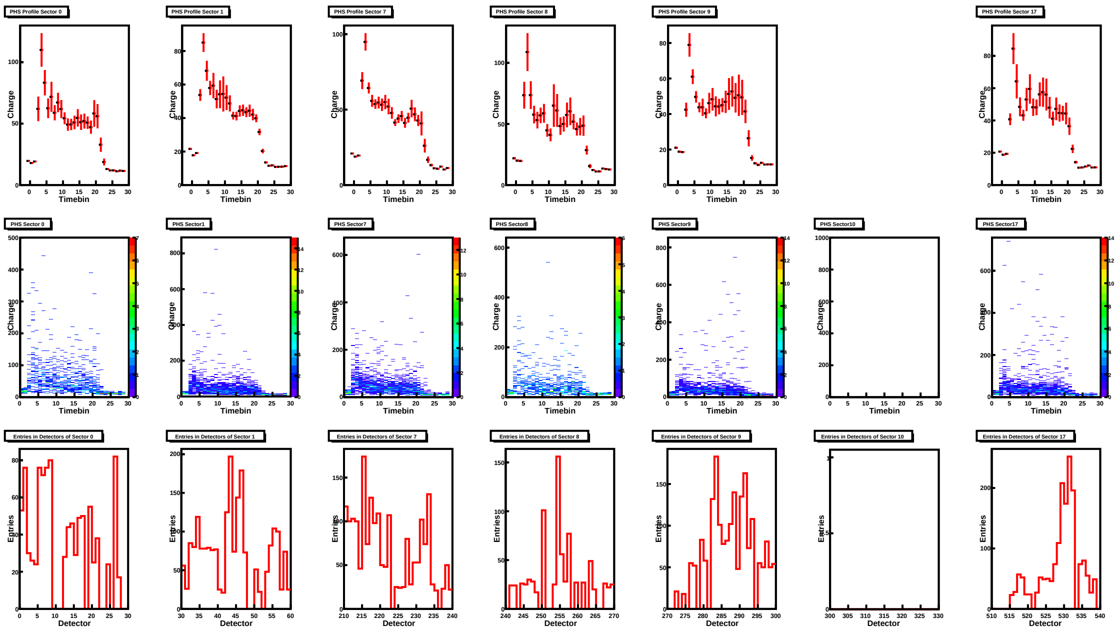

Figure A.25: PHS Profile, PHS and Total Entries per Sector for Run 89069

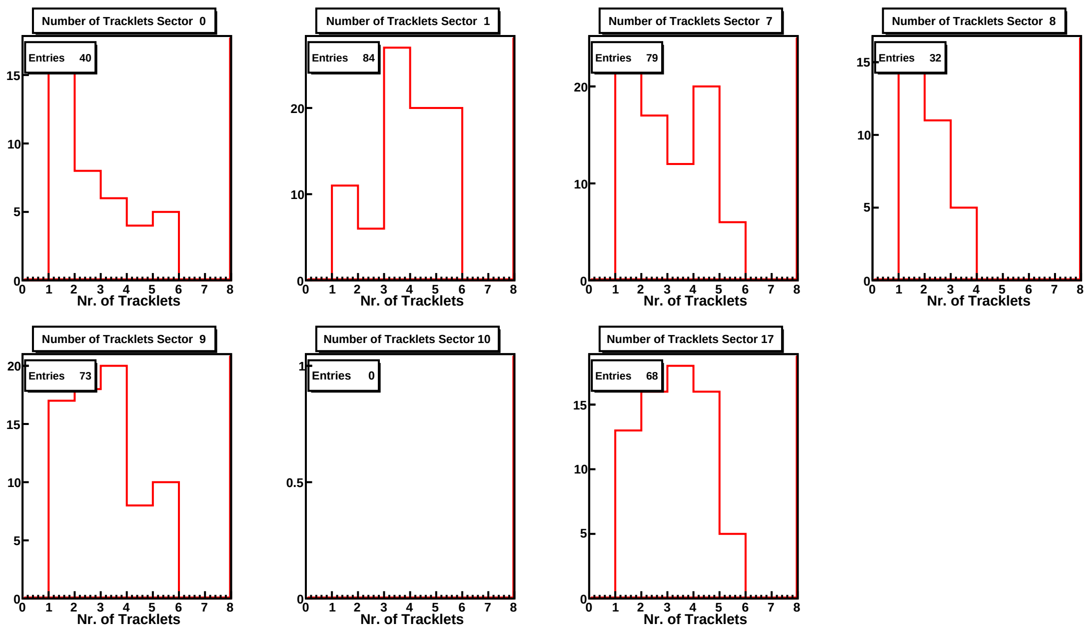

Figure A.26: Tracklets per Track Run 89069

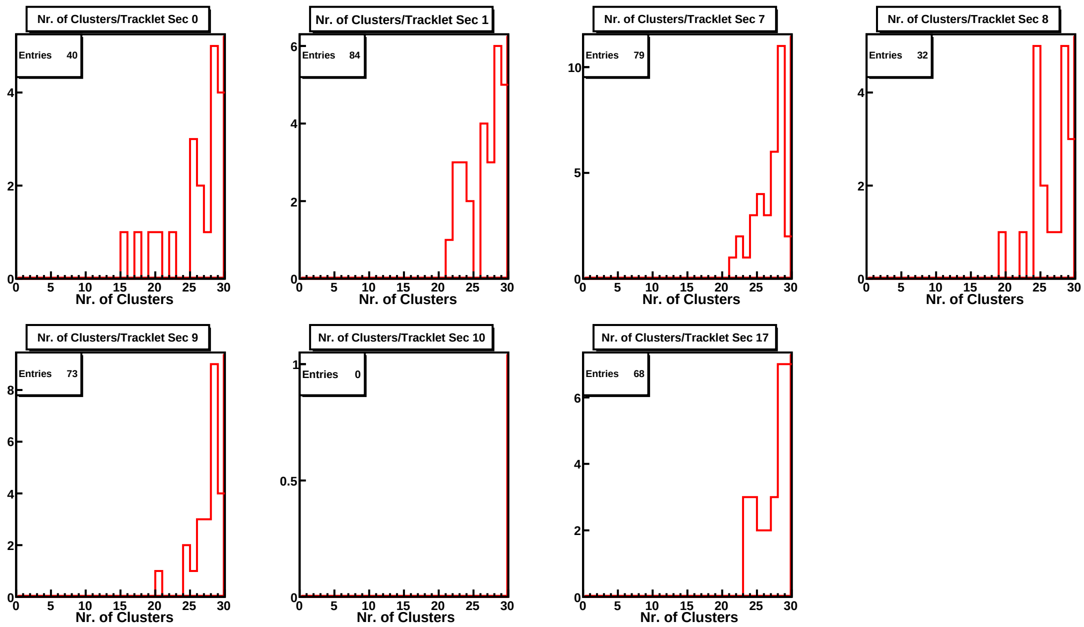

Figure A.27: Clusters per Track Run 89069

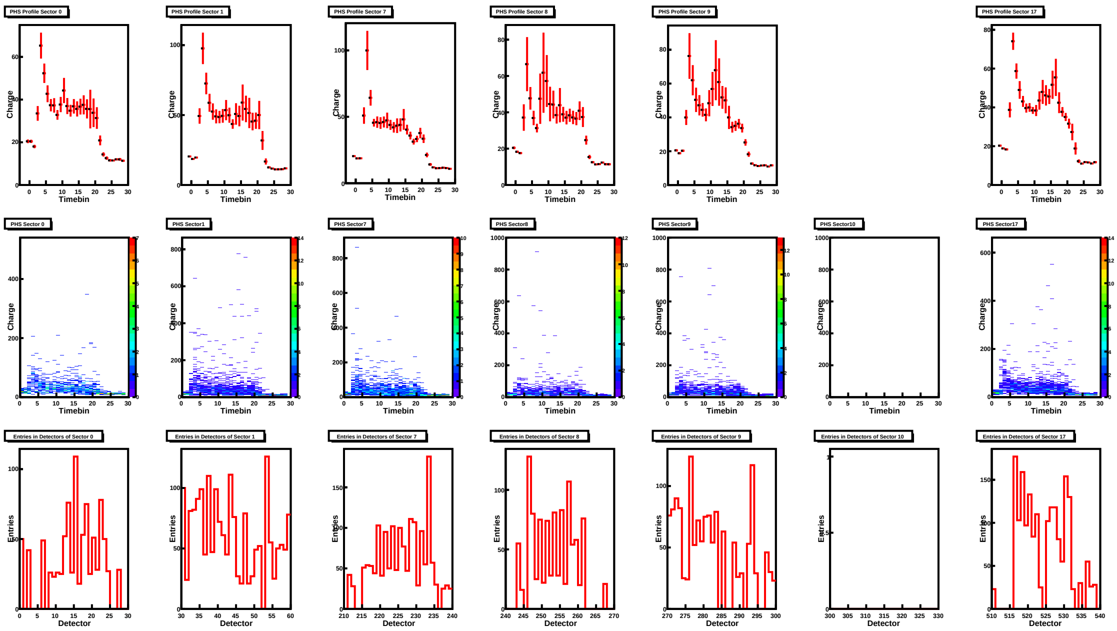

Figure A.28: PHS Profile, PHS and Total Entries per Sector for Run 89097

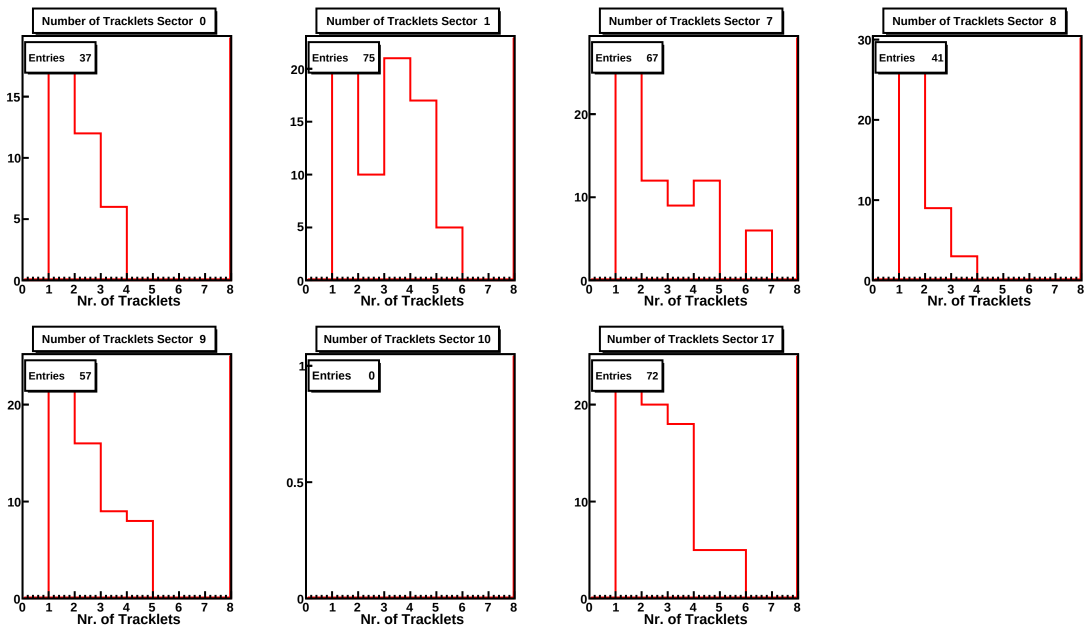

Figure A.29: Tracklets per Track Run 89097

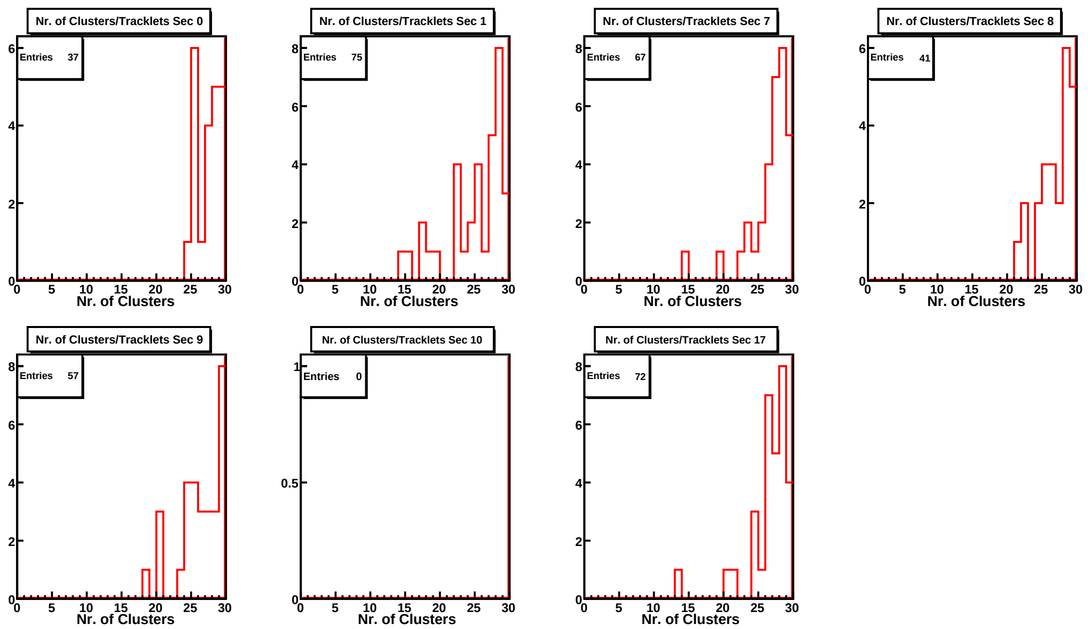

Figure A.30: Clusters per Track Run 89097

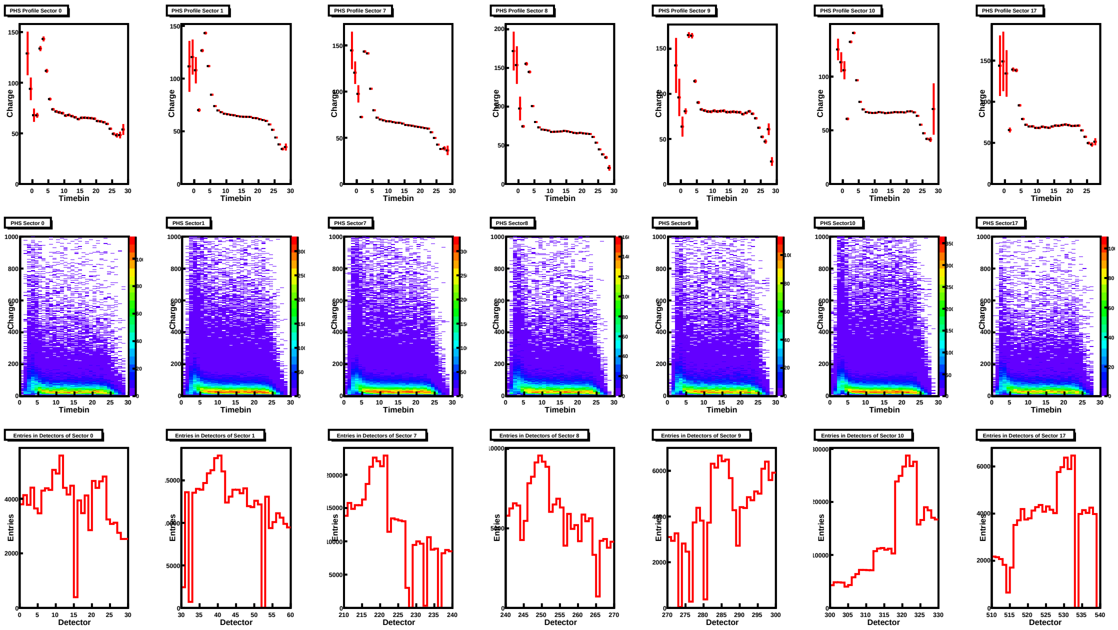

Figure A.31: PHS Profile, PHS and Total Entries per Sector for Run 95741

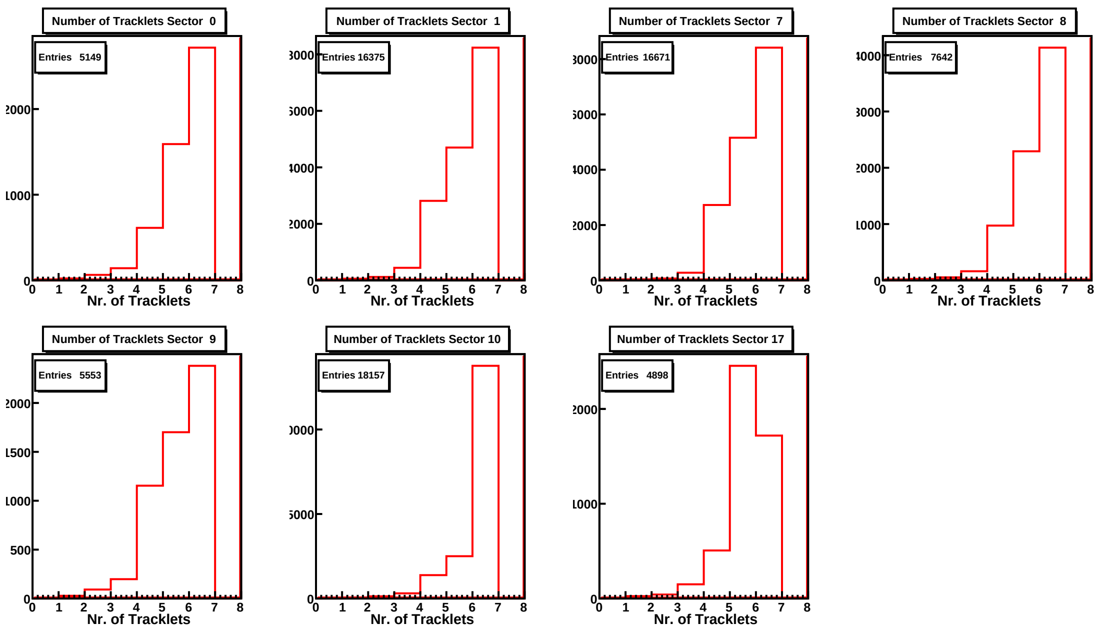

Figure A.32: Tracklets per Track Run 95741

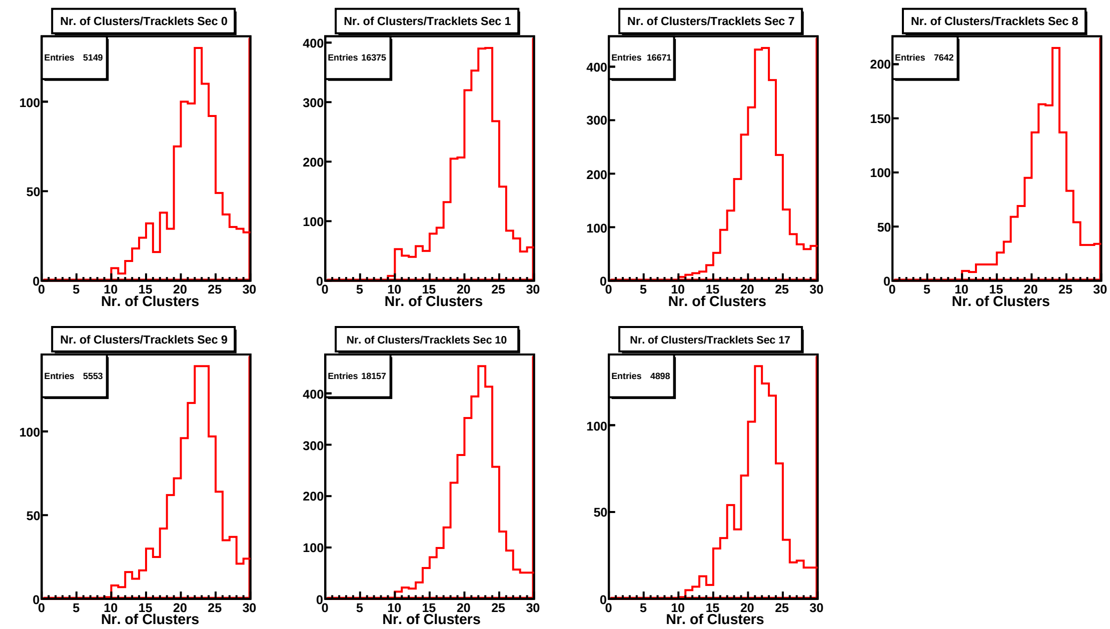

Figure A.33: Clusters per Track Run 95741

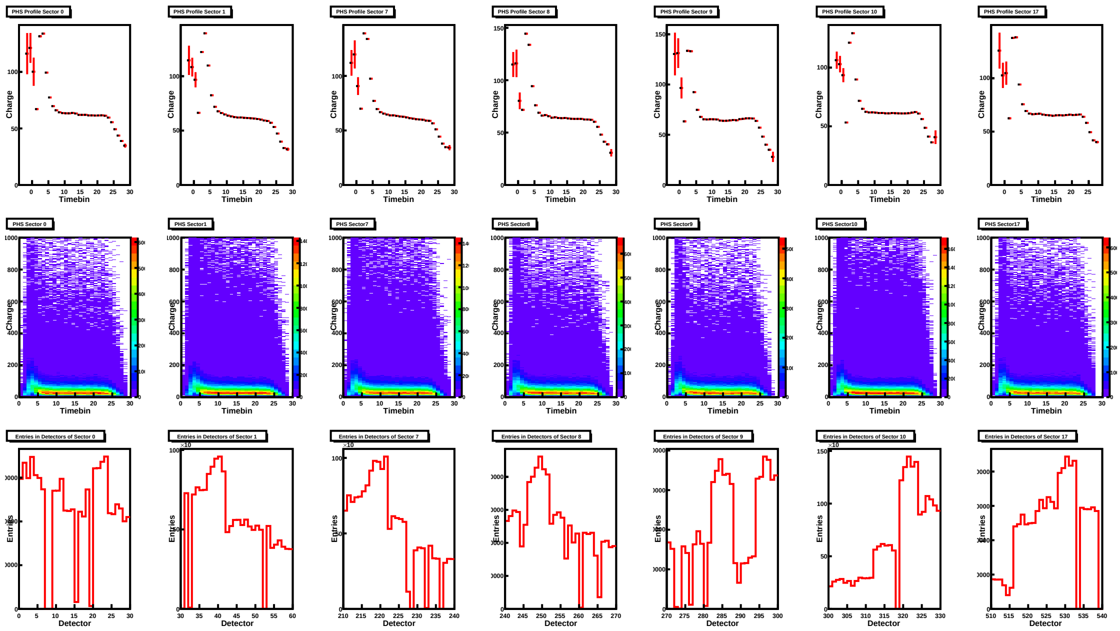

Figure A.34: PHS Profile, PHS and Total Entries per Sector for Run 96287

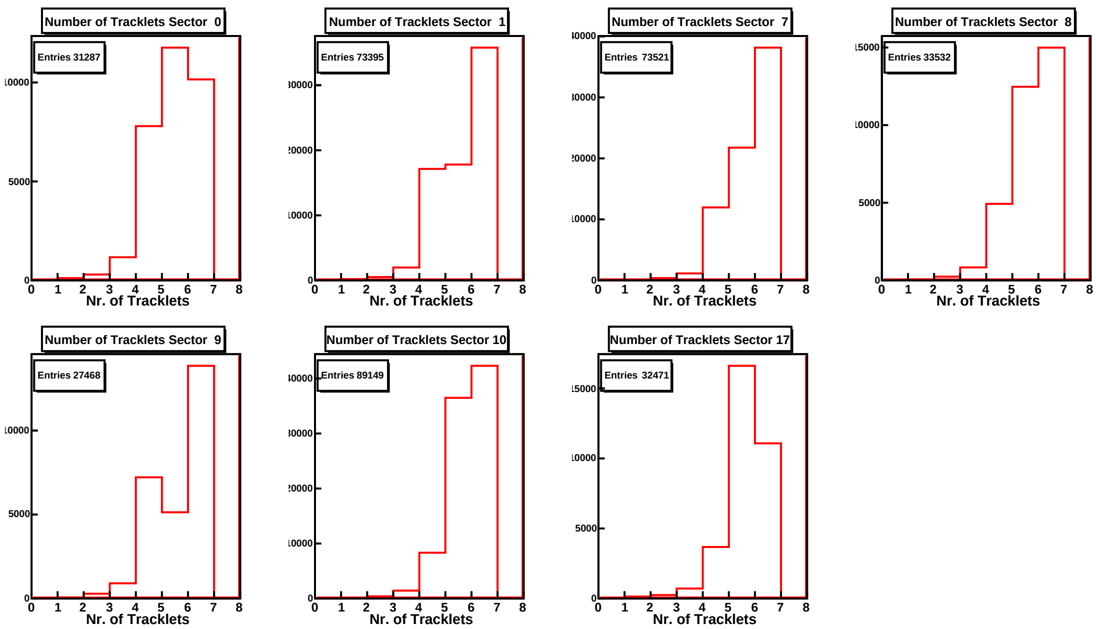

Figure A.35: Tracklets per Track Run 96287

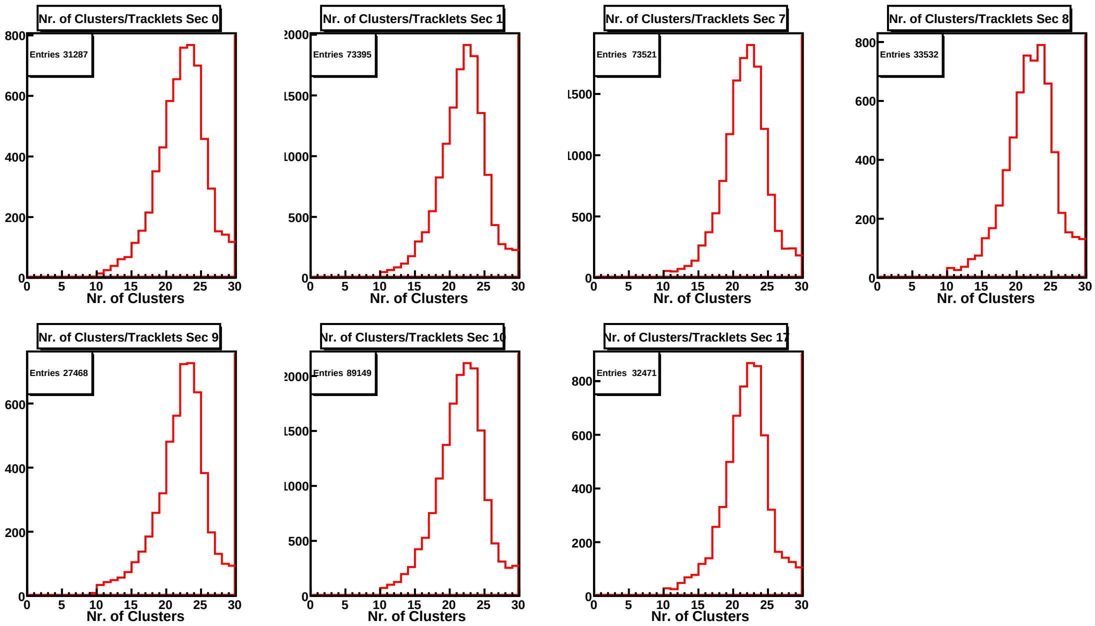

Figure A.36: Clusters per Track Run 96287

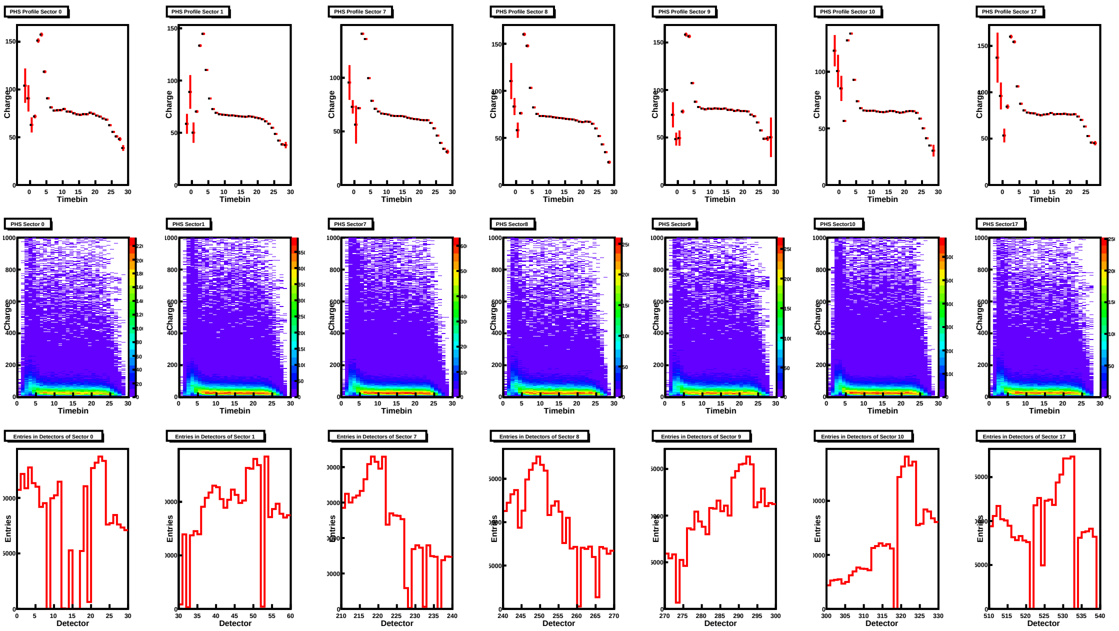

Figure A.37: PHS Profile, PHS and Total Entries per Sector for Run 97873

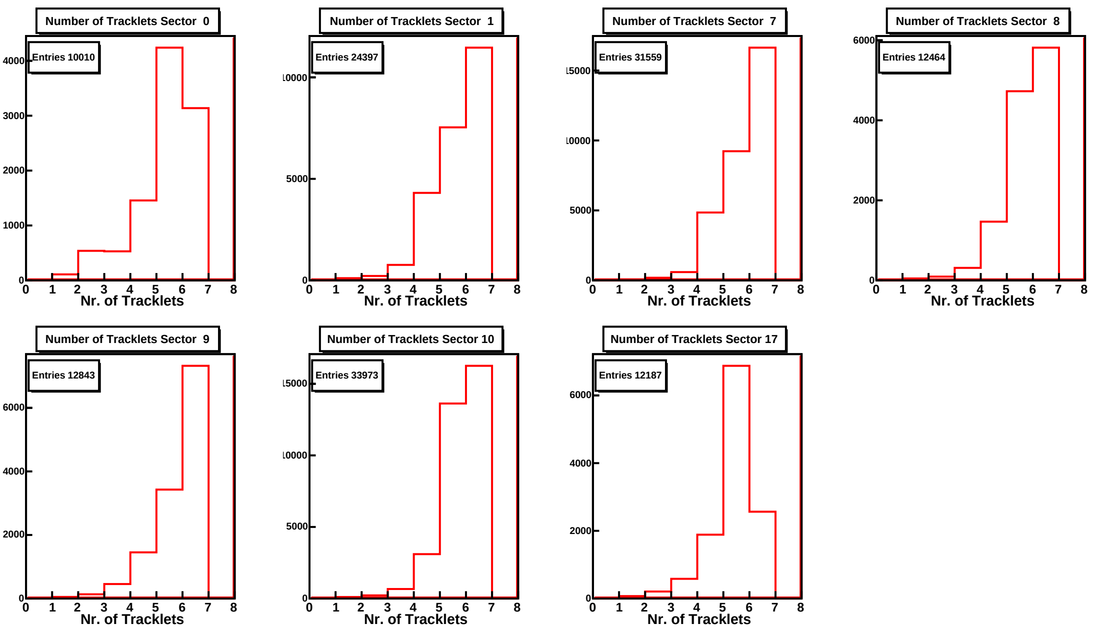

Figure A.38: Tracklets per Track Run 97873

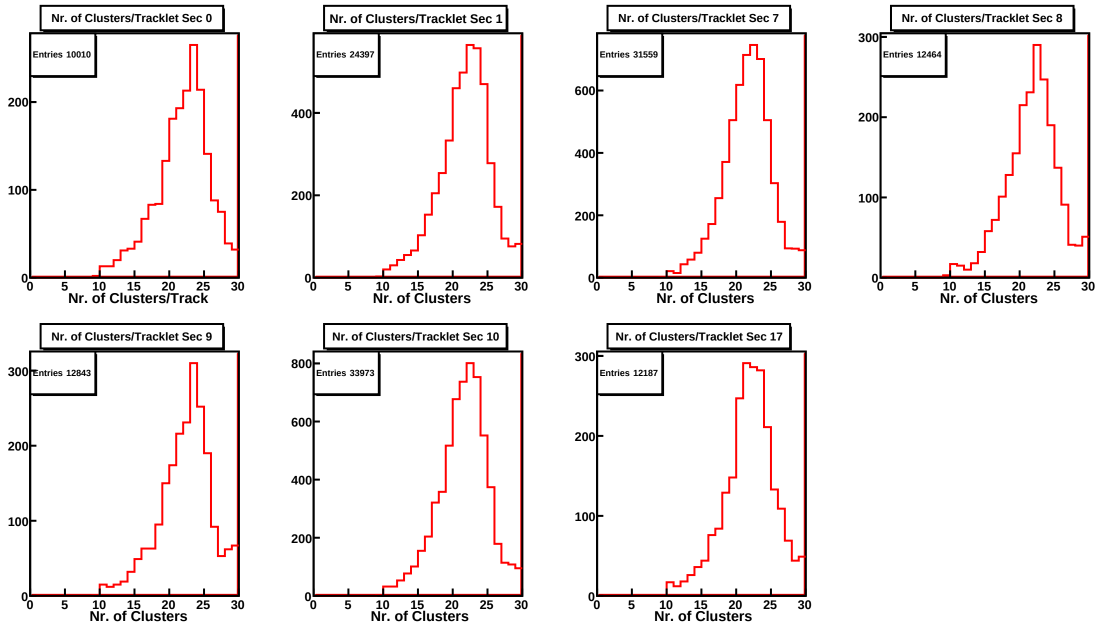

Figure A.39: Clusters per Track Run 97873

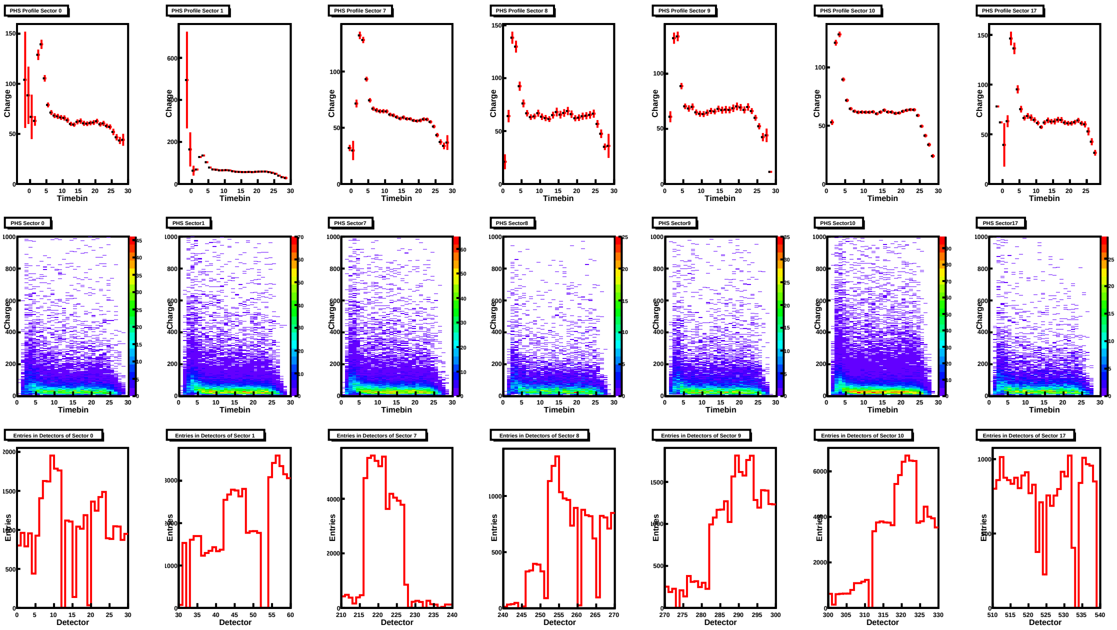

Figure A.40: PHS Profile, PHS and Total Entries per Sector for Run 98371

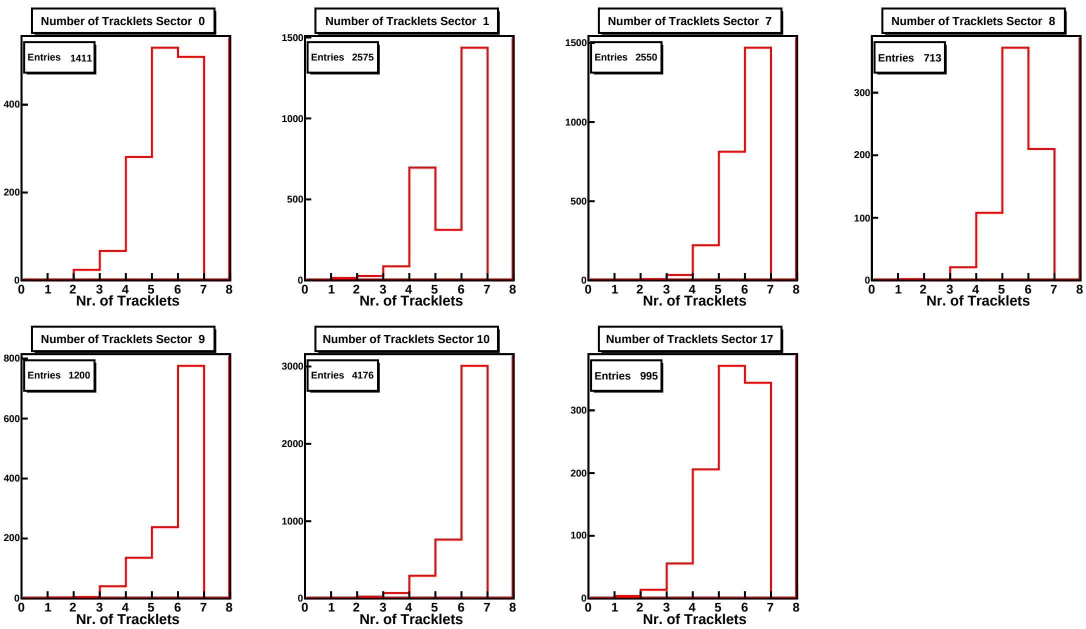

Figure A.41: Tracklets per Track Run 98371

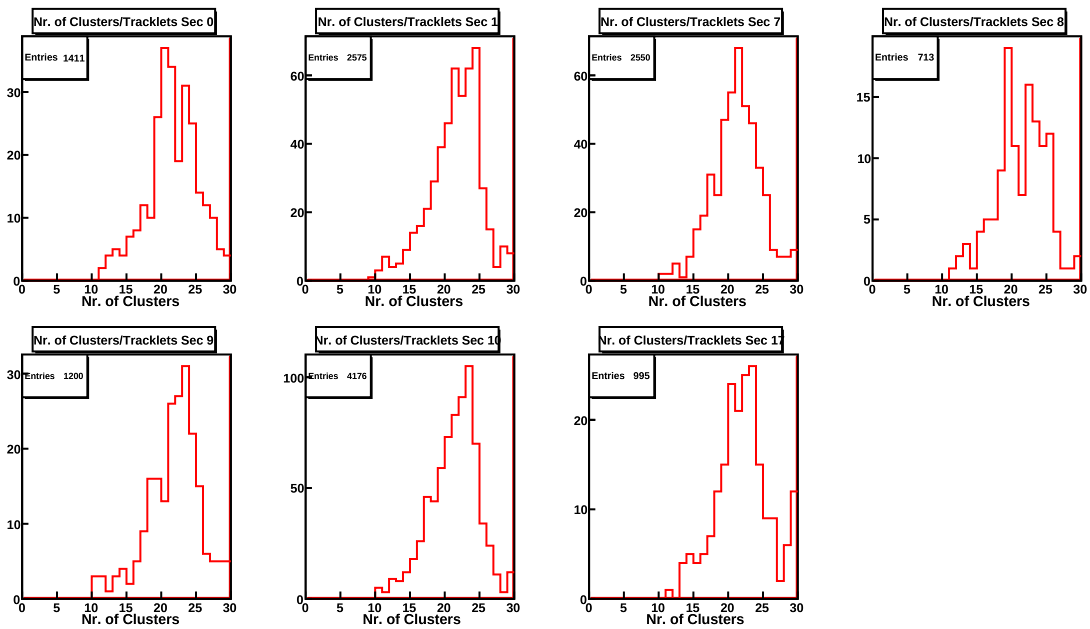

Figure A.42: Clusters per Track Run 98371

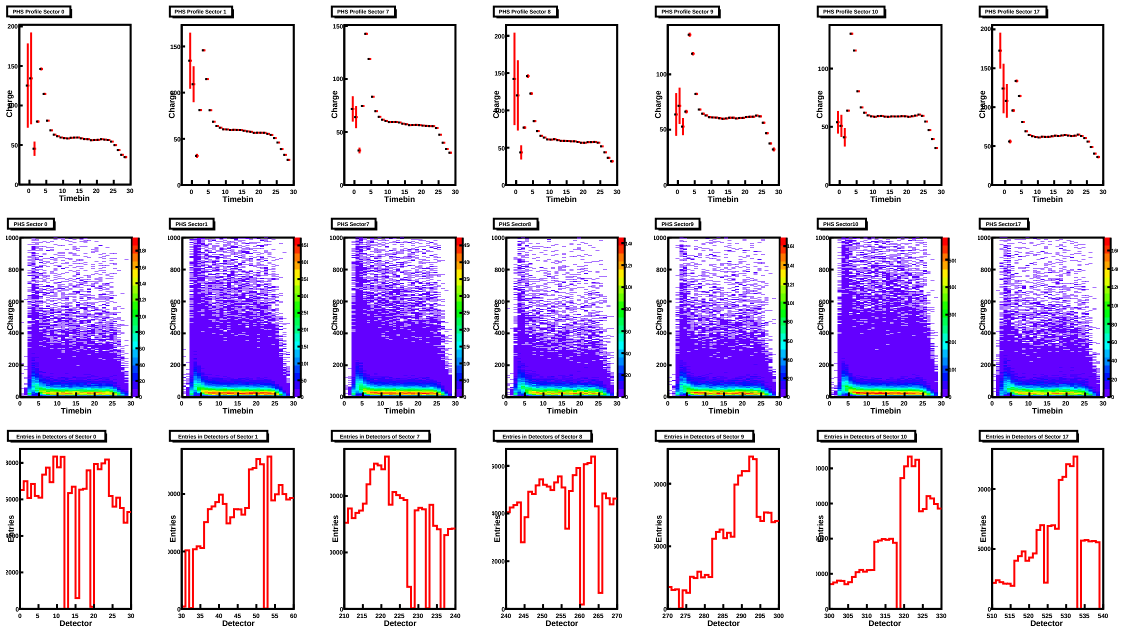

Figure A.43: PHS Profile, PHS and Total Entries per Sector for Run 99031

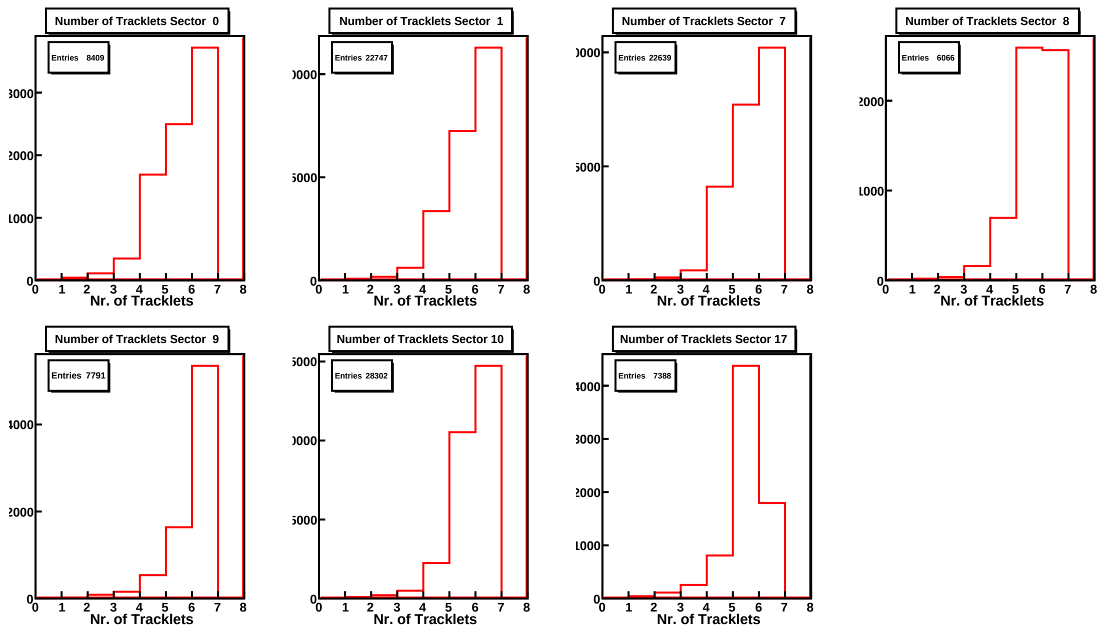

Figure A.44: Tracklets per Track Run 99031

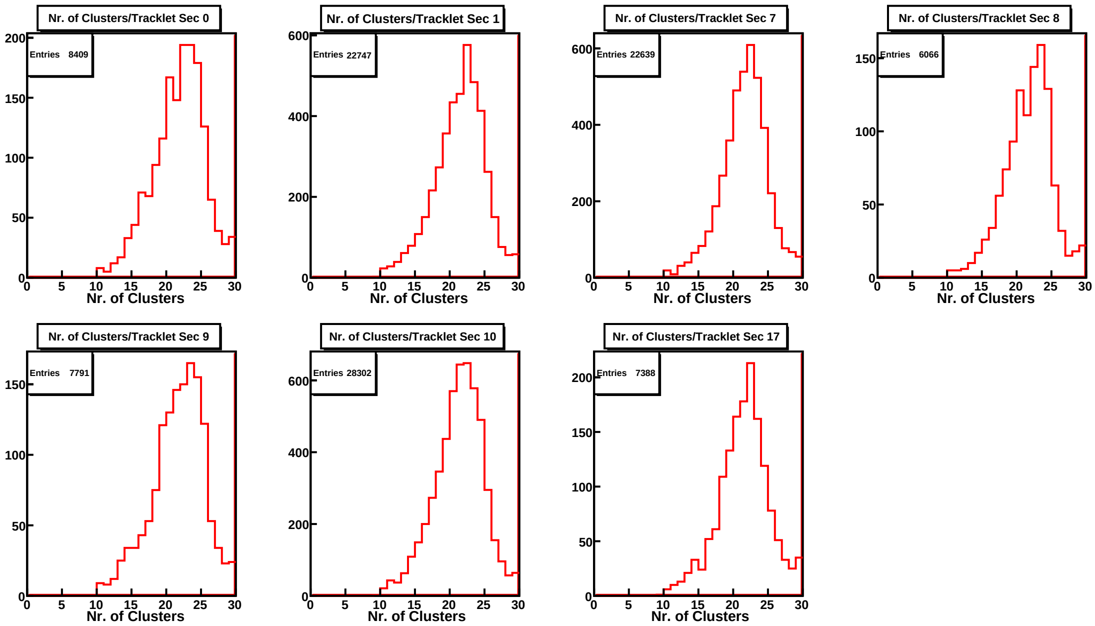

Figure A.45: Clusters per Track Run 99031

Bibliography

[1] L. Evans, *LHC Design Report - The LHC Machine - Introduction*, CERN (2004)

[2] http://www.cern.ch, CERN-AC-9906026

[3] public.web.cern.ch/public/Objects/Research/AccComplex0700829.gif

[4] ATLAS Collaboration, *ATLAS Technical Proposal for a General-Purpose pp Experiment at the Large Hadron Collider at CERN*, CERN/LHCC/94-43, (1994)

[5] CMS Collaboration, *CMS Physics Technical Design Report Volume 1: Detector Performance and Software*, CERN/LHCC/06-001, CMS TDR 8.1, (2006)

[6] LHCb Collaboration, *LHCb Technical Proposal A Large Hadron Collider Beauty Experiment for Precision Measurement of CP Violation and Rare Decays*, CERN/LHCC/98-4, LHCC/P4, (1998)

[7] O. Adriani et al., *LHCf. Technical design report of the LHCf experiment. Measurement of Photons and Neutral Pions in the Very Forward Region of LHCf.*, CERN/LHCC/06-004, LHCf-TDR-001, (2006)

[8] The TOTEM Collaboration, *Letter of Intent Total Cross Section, Elastic Scattering and Diffraction Dissociation at the LHC*, CERN/LHCC/97-49, LHCC/I 11, (1997)

[9] http://visits.web.cern.ch/visits/guides/tools/manual/images/atlasoverview.JPG

[10] http://ireswww.in2p3.fr/ires/recherche/cms/stephanie/images/CMS_3D.gif

[11] http://lhcb.cern.ch/geometry/images/lhcb-x.gif

[12] ALICE Collaboration, *ALICE Technical Proposal for A Large Ion Collider Experiment at the CERN LHC*, CERN/LHCC/95-71, (1995), S. 9 ff

[13] B. Povh, K. Rith, C. Scholz, F. Zetsche, *Teilchen und Kerne*, 6th edition, Springer-Verlag Heidelberg Berlin New York, (2004)

[14] F. Englert, R. Brout, *Broken Symmetry and the Mass of Gauge Vector Mesons*, Phys. Rev. Lett. 13, 321-323 (1964)

[15] Peter W. Higgs, *Broken Symmetry and the Masses of Gauge Bosons*, Phys. Rev. Lett. 13, 508-509 (1964)

[16] http://www.teilchenphysik.de/sites/site_teilchenphysik/content/e25/e734/e1871/Leptonen_800pixe

[17] W. Greiner, S. Schramm, E. Stein, *Quantum Chromodynamics*, 3rd edition, Springer-Verlag Berlin Heidelberg New York, (2006)

[18] A. Andronic, P. Braun-Munzinger, J. Stachel, *Hadron production in central nucleus-nucleus collisions at chemical freeze-out*, Nucl. Phys. A (2006) 167

[19] P. Braun-Munzinger, J. Wambach, *The Phase Diagram of Strongly-Interacting Matter*, arXiv:0801.4256v1 (hep-ph), (2008)

[20] A. Chodos, R. L. Jaffe, K. Johnson, C. B. Thorn, V. F. Weisskopf, *New extended models of hadrons*, Phys. Rev. D 9, 3471-3495, (1974)

[21] ALICE Collaboration, *ALICE: Physics Performance Report, Volume 2*, J. Phys. G: Nucl. Part. Phys. 32, (2006), 1295–2040

[22] J. Rafelski, J. Lettesier, *Strangeness and Quark Gluon Plasma*, arXiv:hep-ph/0305284v1, (2003)

[23] T. Matsui, H. Satz, *J/Ψ suppression by quark-gluon plasma formation*, Phys. Lett. B 178, (1986), 416

[24] P. Braun-Munzinger, *Quarkonium production in ultra-relativistic nuclear collisions: suppression vs. enhancement*, arXiv:nucl-th/0701093v1, (2007)

[25] A. Andronic, P. Braun-Munzinger, K. Redlich, J. Stachel, *Statistical hadronization of charm quarks in ultra-relativisitc nucleus-nucleus collisions*, arXiv:0710.1851v1 [nucl-th], (2007)

[26] www-alice.gsi.de/trd/gallery/index.html

[27] ALICE Collaboration, *ALICE Technical Design Report of the Inner Tracking System*, ALICE TDR 4, CERN/LHCC/99-12, (1999)

[28] ALICE Collaboration, *Technical Design Report of the Time Projection Chamber*, CERN/LHCC/00-001,(2000)

[29] ALICE Collaboration, *Time of Flight System, Technical Design Report*, ALICE TDR 8, CERN/LHCC/2000-12, (2000)

[30] ALICE Collaboration, *Detector for High Momentum PID, Technical Design Report*, ALICE TDR 1, CERN/LHCC/1998-19 (1998)

[31] ALICE Collaboration, *ALICE Technical Proposal for A Large Ion Collider Experiment at the CERN LHC*, CERN/LHCC/95-71, (1995), S. 85 ff

[32] ALICE Collaboration, *ALICE Technical Proposal for A Large Ion Collider Experiment at the CERN LHC*, CERN/LHCC/95-71, (1995), S. 97 ff

[33] ALICE Collaboration, *Technical Design Report of the Photon Multiplicity Detector(PMD)*, ALICE TDR 6, CERN/LHCC/99-32, (1999)

[34] ALICE Collaboration, *Technical Design Report of the Zero Degree Calorimeter (ZDC)*, ALICE TDR 3, CERN/LHCC/99-5, (1999)

[35] ALICE Collaboration, *The Electromagnetical Calorimeter Addendum to the Technical Proposal*, CERN/LHCC/2006-014, (2006)

[36] ALICE Collaboration, *Technical Design Report on Forward Detectors: FMD, T0 and V0*, ALICE TDR 11, CERN/LHCC/2004-25, (2004), Chapter 2

[37] ALICE Collaboration, *Technical Design Report on Forward Detectors: FMD, T0 and V0*, ALICE TDR 11, CERN/LHCC/2004-25, (2004), Chapter 3

[38] ALICE Collaboration, *Technical Design Report on Forward Detectors: FMD, T0 and V0*, ALICE TDR 11, CERN/LHCC/2004-25, (2004), Chapter 4

[39] John D. Jackson, *Klassische Elektrodynamik*, Dt. Übers. K. Müller, 4th edition, de Gruyter, (2006)

[40] ALICE Collaboration, *Technical Design Report of the Transition Radiation Detector*, ALICE TDR 9, CERN/LHCC/01-21, (2001)

[41] ALICE Collaboration, *Technical Design Report of the Computing*, CERN-LHCC-2005-018, ALICE TDR 012, (2005)

[42] http://root.cern.ch

[43] Particle Data Group, *Particle Physics Booklet*, CERN, (2006)

[44] http://www-alice.gsi.de/trd/gallery/index.html

[45] A. Unsöld, B. Baschek, *Der neue Kosmos*, 7th edition, Springer-Verlag Heidelberg, (2001)

[46] Versuchsanleitung Praktikum für Fortgeschrittene *Versuch 2.6 Höhenstrahlung*, Institut für Kernphysik, TU Darmstadt

[47] http://www.ngdc.noaa.gov/stp/SOLAR/COSMIC_RAYS/image/shower.gif

[48] M. Freudenberger *Aufbau eines Teststands und Elektroniktests für den ALICE TRD*, Thesis Proposal, (2008)

[49] ALICE TRD-Database, http://alice.physi.uni-heidelberg.de/trd-db/

Nun ist es an der Zeit, einigen Menschen zu danken, die mich bei der Anfertigung dieses Thesis-Proposals w"ahrend meiner Zeit an der GSI und dem Institut f"ur Kernphysik der Universit"at Frankfurt, aber auch dar"uber hinaus unterst"utzt haben.

Zuerst geht mein Dank an Herrn Prof. Dr. Peter Braun-Munzinger, der mir die M"oglichkeit gegeben hat, in seiner Arbeitsgruppe an der GSI diese Arbeit anzufertigen und dort viel "uber relativistische Schwerionenphysik und dem damit verbundenen experimentellen Aufwand zu lernen.

Mein Dank geht an Herrn Dr. Anton Andronic, der mich in das Thema dieser Arbeit eingef"uhrt und mir als Betreuer jederzeit mit Rat und Tat zur Seite gestanden hat.

Herrn Dr. Helmut Oeschler geb"uhrt ein Dank daf"ur, dass er mich in seiner Vorlesung f"ur das ALICE Projekt begeistern konnte und mich f"ur diese Arbeit angeworben hat.

Ein weiterer Dank geb"uhrt Herrn Dipl. Phys. Benjamin D"onigus, der mir alle Detailfragen beantwortet hat und mich beim Testen unterst"utzt hat.

Ein Dank geht an die Arbeitsgruppe in Frankfurt, wo ich mich in das Thema einarbeiten konnte und besonders an Herrn Dr. Matthias Hartig, der mir dort erkl"arend zur Seite stand.

Bei allen namentlich nicht erw"ahnten Mitgliedern der GSI Arbeitsgruppe m"ochte ich mich f"ur das gute Arbeitsklima innerhalb der Gruppe bedanken.

Last but not least m"ochte ich meiner Mutter f"ur das Korrekturlesen dieser Arbeit und der Unterst"utzung w"ahrend meines bisherigen Studiums danken.

Erklärung zur Master Thesis

Hiermit versichere ich, dass ich diese Arbeit alleine und nur mit den angegebenen Hilfen und Quellen angefertigt habe.
Alle Stellen, die aus den Quellen entnommen wurden, sind als solche kenntlich gemacht.
Diese Arbeit hat in gleicher Form noch keiner Prüfungsbehörde vorgelegen.
Mir ist bekannt, dass ein Exemplar in den Akten des Prüfungssekretariats der TU Darmstadt verbleibt.
Ich bin damit einverstanden, dass diese Arbeit in den Bibliotheksbestand der TU Darmstadt aufgenommen und öffentlich zugänglich gemacht wird.

Darmstadt, den 18. Dezember 2009

(Martin Freudenberger)